

Integration of Antiaromatic Norcorroles

反芳香族分子ノルコロールの集積化

Ukai Shusaku

鵜飼 修作

Department of Molecular and Macromolecular Chemistry,

Graduate School of Engineering, Nagoya University

2022

Preface

The studies in this thesis were conducted under the guidance of Prof. Dr. Hiroshi Shinokubo at Graduate School of Engineering, Nagoya University, during the period from April 2019 to February 2022. This thesis focuses on the integration of the π -planes of the antiaromatic Ni(II) porphyrins.

Numerous aromatic molecules have been synthesized and investigated to develop electronic functions derived from their assemblies. Recently, antiaromatic compounds have been attracted attention because they show significantly different electronic structures from those of aromatic compounds. Fundamental properties of various antiaromatic compounds as a single component have been revealed. However, researches on their assemblies have been significantly delayed due to their inherent instability. This thesis presents several strategies to assemble the π -planes of antiaromatic molecules to develop novel solid-state functions.

Table of Contents

List of Abbreviation	1
Chapter 1	5
General introduction	
Chapter 2	23
Synthesis and electron-transport property of stable antiaromatic Ni(II) norcorrole with the smallest <i>meso</i> -substituent	
Chapter 3	47
A supramolecular polymer constituted of antiaromatic Ni(II) norcorroles	
Chapter 4	81
Charge transfer complexes of antiaromatic Ni(II) norcorroles	
Chapter 5	97
Isolation and structure analysis of a Ni(II) norcorrole radical anion	
Chapter 6	113
Synthesis of Ni(II) <i>meso</i> -di(pentafluorophenyl)norcorrole	
Chapter 7	122
Summary of this thesis	
Experimental Section	125
List of Publications	147
Acknowledgment	150

List of Abbreviations

A	acceptor
Å	ångström unit
Ac	acetyl
Abs	absorbance
AFM	atomic force microscopy
APCI	atmospheric pressure chemical ionization
Ar	aryl
B3	Becke's three-parameter hybrid exchange function
bpy	bipyridine
C	concentration
calcd	calculated
CAM	coulomb-attenuating method
cod	1,5-cyclooctadiene
Cp	cyclopentadienyl
CT	charge transfer
C_T	total concentration
CV	cyclic voltammetry
D	donor
δ	chemical shift
DDQ	2,3-dichloro-5,6-dicyano- <i>p</i> -benzoquinone
ΔG	change in Gibbs free energy
ΔH	change in enthalpy
ΔS	change in entropy
DFT	density functional theory
DMF	<i>N,N</i> -dimethylformamide
DMAP	4-dimethylaminopyridine
DMSO	dimethyl sulfoxide
DNA	deoxyribonucleic acid
ϵ	molar extinction coefficient
EDCI	1-(3-dimethylaminopropyl)-3-ethylcarbodiimide
Et	ethyl
ESI-MS	electrospray ionization mass spectrometry
ESR	electron spin resonance

f	oscillator strength
Fc	ferrocene
FP	flash-photolysis
FT	Fourier-transform
h_e	molecular enthalpy
HOMA	harmonic oscillator model of aromaticity
HOMO	highest occupied molecular orbital
HR-MS	high resolution mass spectrometry
IR	infrared
λ	wavelength
λ	relaxation energy
J	coupling constant (NMR)
K_a	equilibrium constants for the nucleation process
LUMO	lowest unoccupied molecular orbital
M	molar
Mes	mesityl
MALDI	matrix assisted laser desorption ionization
Me	methyl
<i>m</i> CPBA	<i>m</i> -chloroperoxybenzoic acid
min	minute(s)
MPD	mean planer deviation
NBS	<i>N</i> -bromosuccinimide
NICS	nucleus-independent chemical shift
NIR	near infrared
NMR	nuclear magnetic resonance
OFET	organic field-effect transistor
PAH	polycyclic aromatic hydrocarbons
Ph	phenyl
Φ_n	degree of aggregation
Φ_{SAT}	unit normalization constant
φ	photo-generation efficiency of the charge carriers
ppm	part per million
% <i>T</i>	transmittance
R	an organic group
<i>R</i>	gas constant
r.t.	room temperature

$\Sigma\mu$	sum of the isotropic electron and hole mobility
SOMO	singly occupied molecular orbital
STM	scanning tunneling microscope
<i>t</i> -Bu	1,1-dimethyl-1-ethyl
TCNE	tetracyanoethylene
TCNQ	tetracyanoquinodimethane
TD	time-dependent
T_e	elongation temperature
TEM	transmission electron microscopy
TEMPOL	1-oxyl-2,2,6,6-tetramethyl-4-hydroxypiperidine
THF	tetrahydrofuran
TIPS	triisopropylsilyl
TLC	thin-layer chromatography
TMS	trimethylsilyl
TRMC	time-resolved microwave conductivity
TTF	tetrathiafulvalene
UV	ultraviolet
v	volume
vis	visible
VT	variable-temperature

Chapter 1

General Introduction

Contents

1-1. Aromatic compounds	6
1-2. Antiaromatic compounds	8
1-3. Norcorroles.....	11
1-4. Overview of this thesis.....	18
1-5. References	20

1-1. Aromatic compounds

Material properties strongly depend on the electronic structure, shape, and arrangement of the component atoms and molecules. Inorganic materials composed of metals, silicon, and III-V group elements form periodic packing structures that exhibit attractive electronic functions such as dielectric, conductive, semiconductive, ferromagnetic, and superconductive. These intriguing features of inorganic materials have attracted significant attention of theoreticians to establish the field of solid-state physics.

The main advantage of organic compounds compared to inorganic materials is the potential to change both the electronic and structural properties of organic molecular compounds through chemical modification. In addition, organic compounds have excellent processability, which enables flexible material design. However, materials research based on organic compounds has been slower than the progress of inorganic materials. This is because the creation of organic molecules as raw materials must involve the development of multiple factors, such as synthetic methods, purification techniques, and structural determination. In particular, highly reactive molecules are difficult to handle, and investigating the properties is not easy.

Hückel's rule was proposed in 1931 to explain the stability of compounds with π -electrons in a planar cyclic conjugate circuit.¹ According to this rule, a compound with $4n+2$ cyclic π -electrons is defined as an aromatic compound (Figure 1-1). In general, aromatic compounds exhibit high stability due to the effective conjugation of π -electrons. In particular, benzene is a typical aromatic compound with six π -electrons in a planar ring. Planar compounds with fused benzene rings are also highly stable.² Importantly, aromatic compounds can be handled without steric protection by bulky substituents.

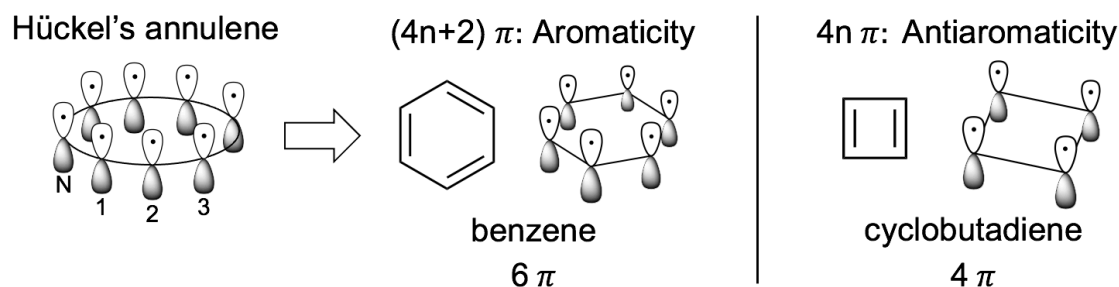


Figure 1-1. Hückel aromaticity and antiaromaticity.

Figure 1-2 shows the stacking structure of benzene and fused aromatic compounds. The stacking pattern depends on the size and shape of the π -planes.³ The overlap of π -orbitals enables charge transport properties.

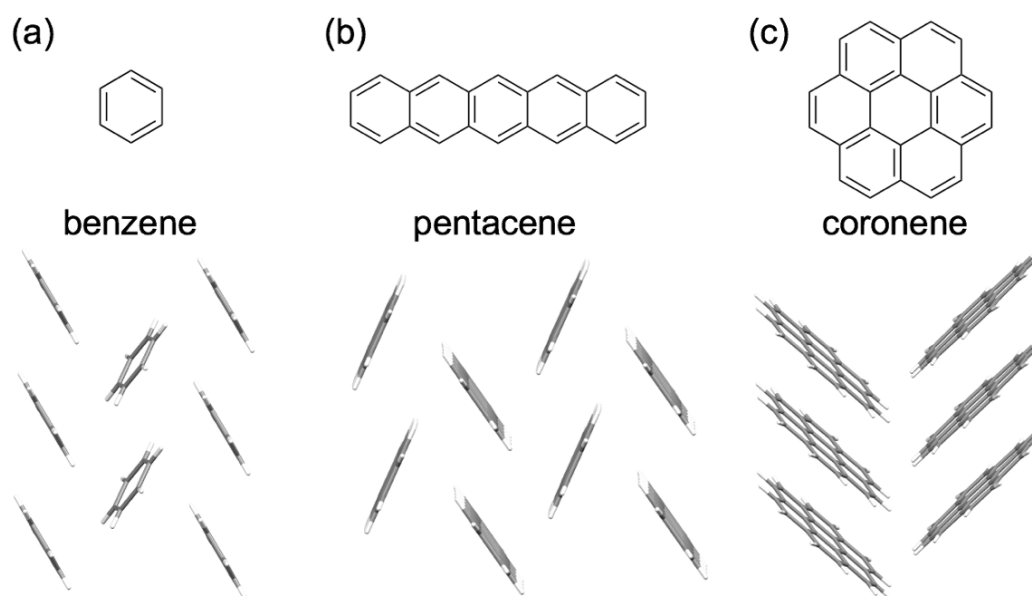


Figure 1-2. Structures and crystal packings of (a) benzene, (b) pentacene, and (c) coronene.

Since the early '80s of the last century, vast amounts of research efforts for organic π -conjugated compounds have been focused on the fundamental properties of organic metals,⁴ organic field-effect transistors (OFETs),⁵ and organic superconductor.⁶ Their use as active materials in organic electronics has been developed based on the knowledge of solid-state physics.

1-2. Antiaromatic compounds

A compound with $4n$ π -electrons in a planar ring is defined as antiaromatic compounds by Hückel's rule (Figure 1-1).¹ In contrast to aromatic compounds, experimental and theoretical studies revealed that such electron systems are not stabilized by π -electron conjugation. The highly symmetrical antiaromatic compound has two degenerate SOMOs with an open-shell triplet diradical ground state (Figure 1-3). However, such an open-shell structure is unstable. Accordingly, this instability causes a bond alternation to a lower symmetry structure with a more stable closed-shell system in the ground state (Jahn–Teller distortion).⁷ For these reasons, antiaromatic compounds with small bond alternation have a narrow HOMO–LUMO gap, which causes various electronic properties and functions such as biradical properties,⁸ near-infrared absorption,⁹ and multi-redox capability.¹⁰ Consequently, antiaromatic compounds should be attractive for electronic materials.

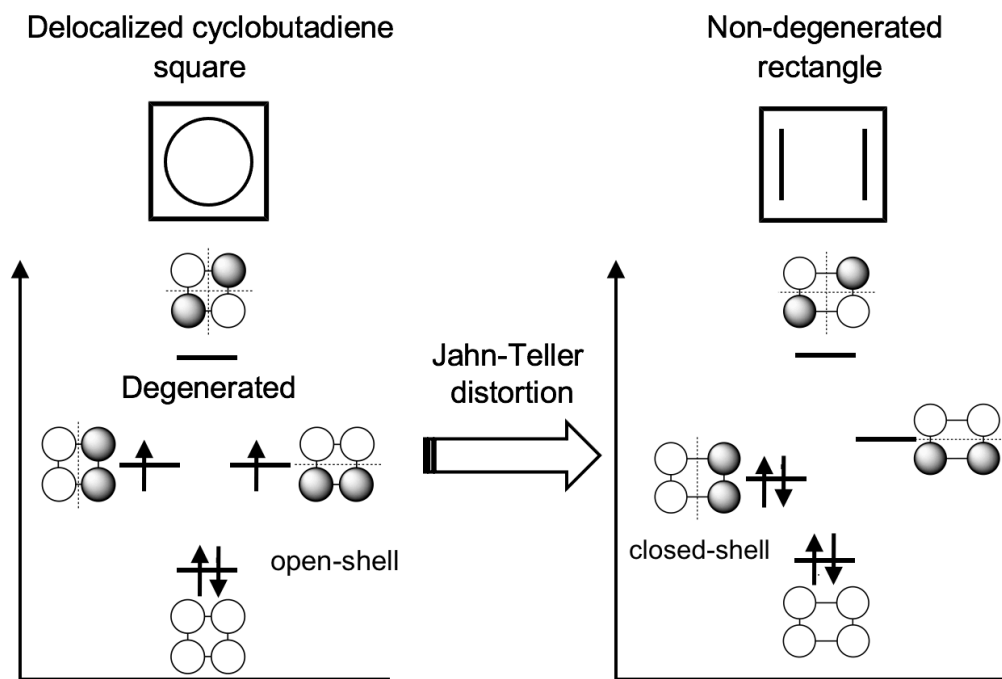
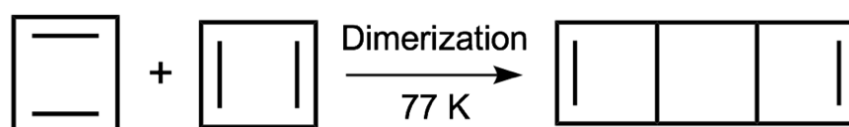


Figure 1-3. Electronic configuration of cyclobutadiene.

However, despite its attractive electronic properties, the localized double bonds formed by the bond alternation and high HOMO and low LUMO energies cause a variety of side reactions. For example, cyclobutadiene undergoes the dimerization reaction even under extremely low-temperature conditions at 77 K (Scheme 1-1).¹¹



Scheme 1-1. Dimerization of cyclobutadiene.

Bulky substituents such as *t*-Bu, TMS, and mesityl groups are often introduced at peripheral positions to stabilize the antiaromatic molecule.¹² For example, several antiaromatic molecules such as cyclobutadiene,^{12f} pentalene,^{12a} indacene,^{12g} and cyclooctatetraene (COT)^{12h} have been successfully isolated by the kinetic stabilization strategy (Figure 1-4). However, bulky substituents inhibit the dense packing of each π -planes. In other words, kinetic stabilization is suitable for investigating the properties of independent single molecule.

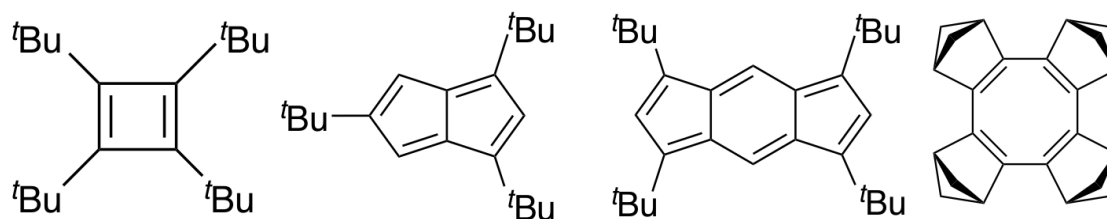


Figure 1-4. Kinetically stabilized antiaromatic molecules.

In addition to kinetic stabilization, the fusion of aromatic rings to the peripheral sites also stabilizes antiaromatic molecules thermodynamically. This strategy also

enabled the synthesis of a variety of antiaromatic molecules (Figure 1-5).^{14,15,15} Furthermore, there is no requirement for bulky substituents, which allows the formation of π -stacked packing structures in the solid-state. For example, TIPS-substituted thiophene-fused COT derivatives exhibit charge transport properties due to the partial overlap of the π -planes in the crystal (Figure 1-6).¹⁶ In addition, this molecule exhibits bipolar FET properties, which would be attributed to the characteristics of antiaromatic molecules with destabilized HOMO and stabilized LUMO levels. However, thermodynamic stabilization reduces the contribution of the $4n$ π -electrons system due to the localized aromatic rings. Consequently, the electronic structure is strongly disturbed, which hampers the verification of the effect of antiaromaticity.

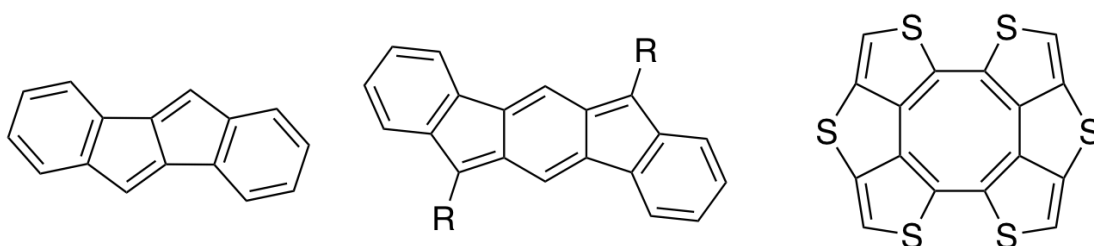


Figure 1-5. Thermodynamically stabilized antiaromatic molecules.

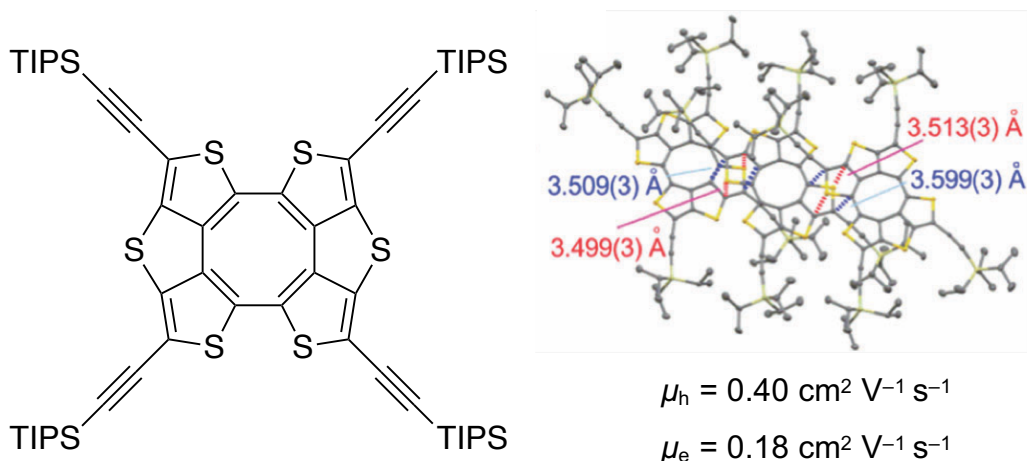


Figure 1-6. Packing structure of thiophene-fused COT.

1-3. Norcorroles

Norcorrole is a ring-contracted porphyrinoid, which lacks two *meso*-carbons from a regular porphyrin (Figure 1-7). Norcorrole contains 16 π -electrons in the macrocyclic conjugation, thus being antiaromatic.

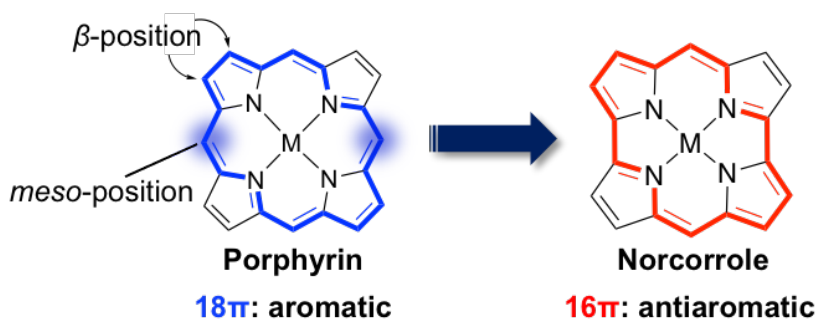
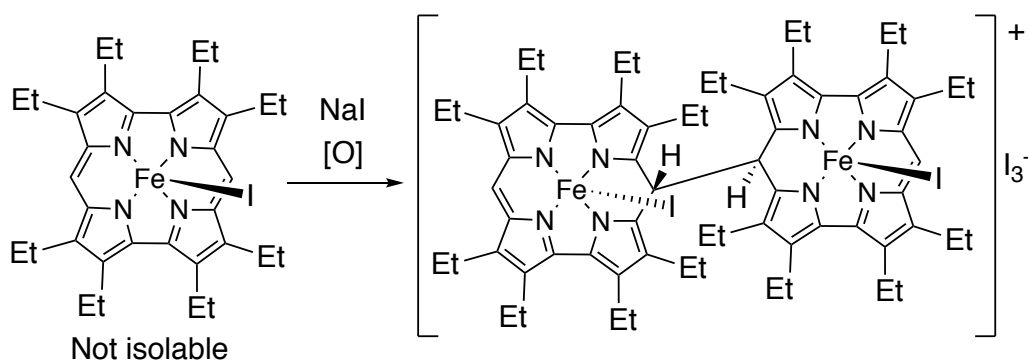


Figure 1-7. Structure of porphyrin and norcorrole.

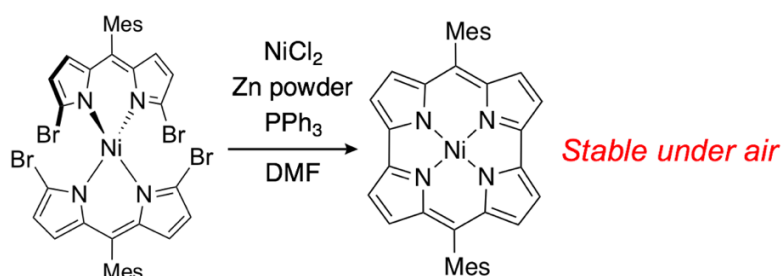
In 2008, octaethylnorcorrole Fe(III) complex was reported by Bröring and co-workers. However, this Fe(III) complex was not isolated due to dimerization at the *meso* positions (Scheme 1-2).¹⁷



Scheme 1-2. Dimerization of Fe(III) norcorrole complex.

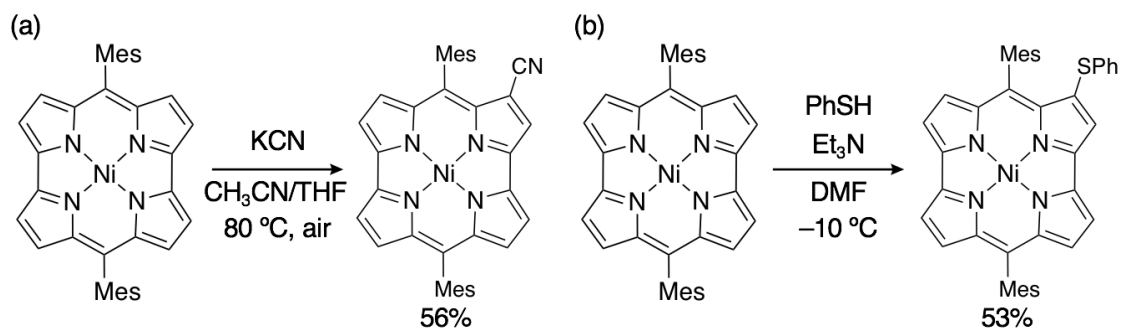
After this report, in 2012, Shinokubo and co-workers succeeded in synthesizing Ni(II) *meso*-dimesitylnorcorrole through the reductive coupling reaction of Ni(II) dibromodipyrrin (Scheme 1-3).¹⁸ Furthermore, the X-ray crystal structure analysis revealed that Ni(II) norcorrole has a highly planar structure, which secures an effective conjugation circuit with 16 π -electrons. Theoretical and experimental studies have

demonstrated that Ni(II) norcorrole shows a distinct antiaromatic character. Notably, Ni(II) *meso*-dimesitylnorcorrole was highly stable under ambient conditions. Considering the results of the dimerization reaction at the *meso*-position of the Fe(III) norcorrole in scheme 1-2, the steric protection of the *meso*-positions of Ni(II) norcorrole is expected to play an important role in the stability. The discovery by Shinokubo and co-workers accelerated the study of antiaromatic molecules. The following are some of the studies related to this thesis.



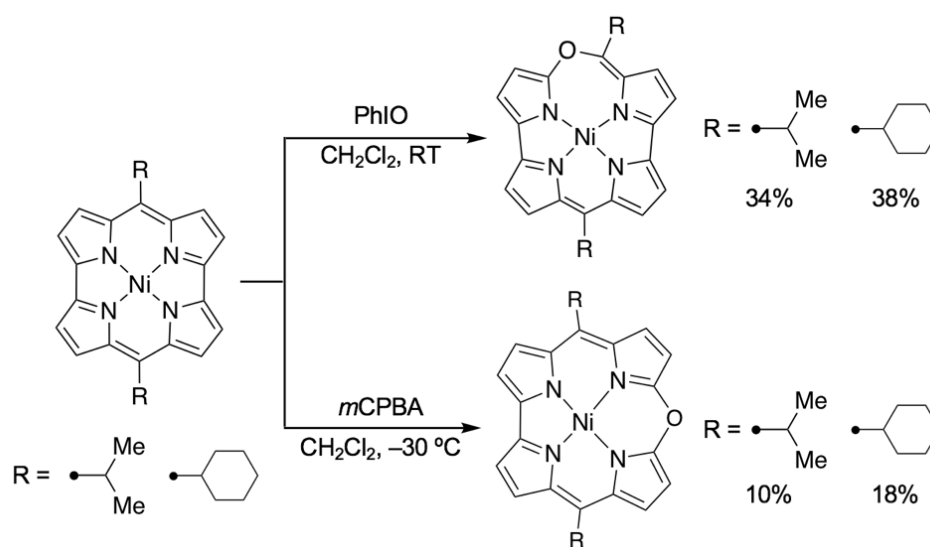
Scheme 1-3. Synthesis of norcorrole Ni(II) *meso*-dimesitylnorcorrole.

The nucleophilic reaction to Ni(II) *meso*-dimesitylnorcorrole was investigated (Scheme 1-4).¹⁹ Ni(II) norcorroles have a low-lying LUMO, allowing direct cyanation and thiolation to proceed to the periphery without the help of a catalyst. Interestingly, after the nucleophilic reaction to the norcorrole core, the norcorrole 16 π -electrons system is retained. This result implies that the aromatic stabilization of local pyrroles contributes to the stability of norcorrole.



Scheme 1-4. (a) Cyanation and (b) thiolation of Ni(II) *meso*-dimesitylnorcorrole.

meso-Dialkylporphyrins were synthesized to investigate their stability and reactivity. Ni(II) porphyrins with isopropyl and cyclohexyl groups at the *meso* positions are substantially stable under ambient conditions. Interestingly, the oxygen insertion position of these *meso*-dialkylporphyrins was controlled by the choice of oxidants (Scheme 1-5).²⁰ The markedly different regioselectivities indicate that the steric protection of the reacting *meso*-positions is crucial for the reactivity of the porphyrin.



Scheme 1-5. Structure of Ni(II) *meso*-dialkylporphyrins and oxidation.

Modification of the electronic properties of Ni(II) porphyrins with *meso*-substituents has been investigated. Various substituted aryl Ni(II) porphyrins were synthesized to investigate their electronic structure and stability. However, due to their instability, the Ni(II) porphyrins with electron-withdrawing or electron-donating groups at two *meso*-positions were not obtained. However, unsymmetrical Ni(II) porphyrins with both electron-donating and electron-withdrawing groups were handled under ambient conditions (Figure 1-8).²¹ Interestingly, unsymmetrical Ni(II) porphyrins showed low energy absorption due to intramolecular charge-transfer interactions.

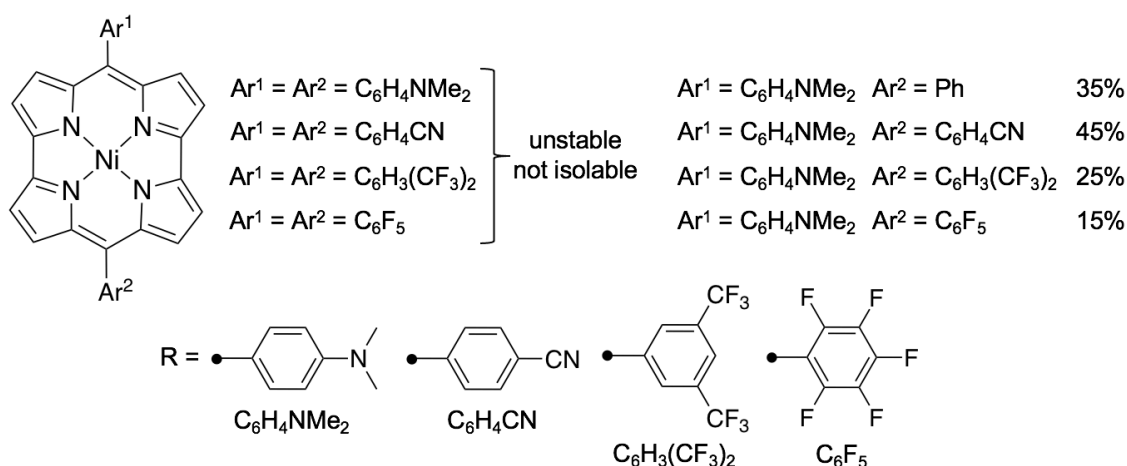


Figure 1-8. Ni(II) norcorrole substituted electron-withdrawing and donating groups at the *meso*-positions.

The synthesis and electronic structure of benzo-fused norcorroles were investigated (Figure 1-9).^{8b} As mentioned above, benzo-fused antiaromatic compounds are generally diminished in antiaromaticity due to the disrupted $4n\pi$ electron system. However, the benzo-fused norcorroles exhibited strong antiaromaticity due to the 16π electron system inside the norcorrole induced by the fused benzene rings. Due to its strong antiaromaticity, Ni(II) tetrabenzonorcorrole exhibited a diradical character. Due to the narrow HOMO–LUMO gap, the thermal excitation causes a transition to triplet state ($J_{S-T} = -1.40$ kcal mol⁻¹).

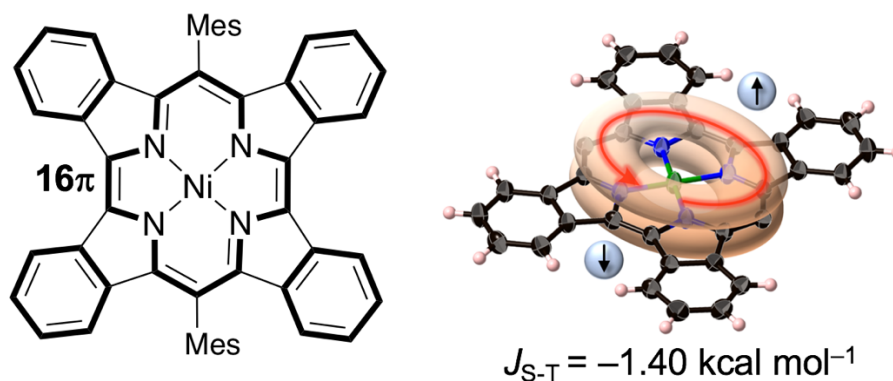


Figure 1-9. Structure of tetrabenzonorcorrole and 16π electron circuit.

Schleyer *et al.* predicted that the stacking of cyclobutadiene π -systems would lead to a loss of antiaromaticity due to the interaction between the frontier orbitals of each π -system (Figure 1-10).²² In other words, π -stacking antiaromatic molecules should exhibit three-dimensional aromaticity.

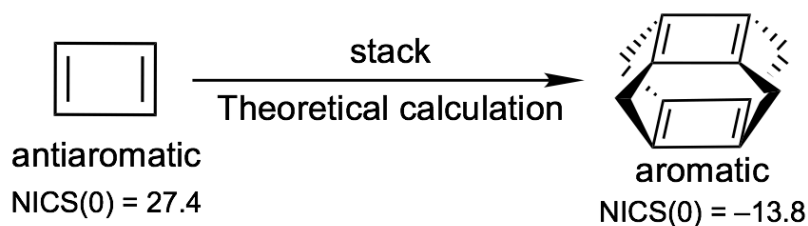


Figure 1-10. Stacked antiaromatic cyclobutadiene.

Various types of Ni(II) norcorrole dimers were synthesized and investigated the aromaticity by theoretical and experimental studies to demonstrate this prediction.²³ Notably, stacked Ni(II) norcorrole by linkers caused a decrease in their antiaromaticity. In particular, thiophene-bridged cyclophane dimer exhibited a significant decrease in antiaromaticity than alkyl chains linked one (Figure 1-11).^{23a,23b}

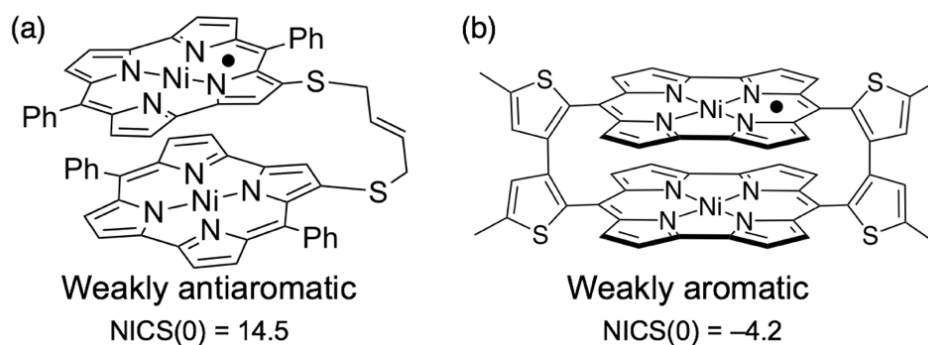


Figure 1-11. (a) Alkyl linked and (b) thiophene-bridged Ni(II) norcorrole dimers.

Recently, cyclophane type Ni(II) norcorrole linked by two flexible alkyl chains has been synthesized to evaluate the aromaticity (Figure 1-12).^{23c} This norcorrole cyclophane

showed a crystalline polymorph and three different solid-phase structures. Surprisingly, one of them aligned face-to-face stacking structure (Figure 1-12c). In this orientation, the exchange repulsion between the two π -clouds should be maximal, but the π - π distance is extremely close, at 3.258 Å (the π - π distances in (a) and (b) are 3.33 Å and 3.39 Å, respectively). Furthermore, in the slipped and twisted structures, the composed norcorroles exhibited antiaromaticity, while the face-to-face stacking exhibited three-dimensional aromaticity. The stacking orientation would also be an essential factor in achieving three-dimensional aromaticity.

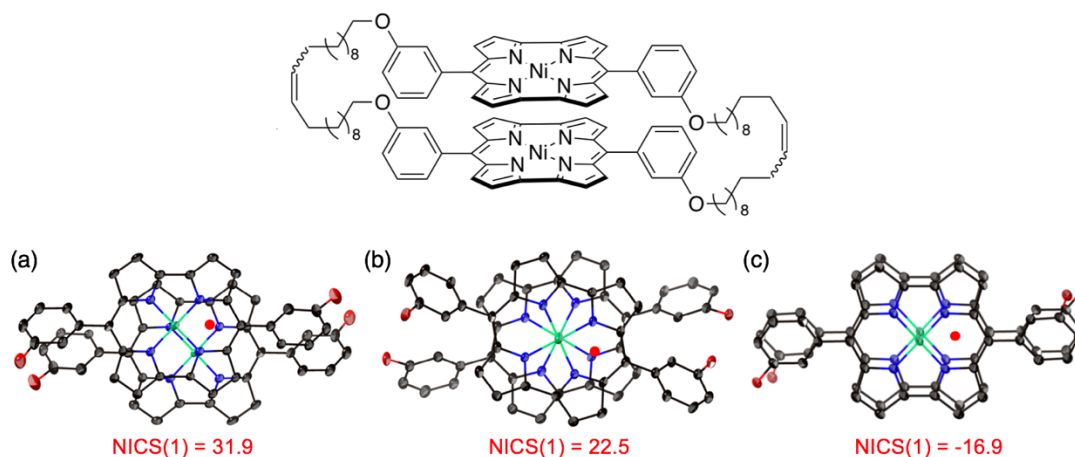


Figure 1-12. X-ray structures of norcorrole cyclophane with flexible linkers. (a) Slipped, (b) twisted stacking, and (c) face-to-face stacking orientations. Hydrogen atoms and alkyl chains are omitted for clarity.

The electrical conductance of a single molecule of Ni(II) norcorrole was investigated by STM. The thioester functionalized Ni(II) norcorrole exhibited more than 20 times higher conductivity than the similar aromatic molecule Ni(II) porphyrin. By changing the applied electrochemical potential, the Ni(II) norcorrole conductance can be controlled by nearly an order of magnitude (Figure 1-13).²⁴

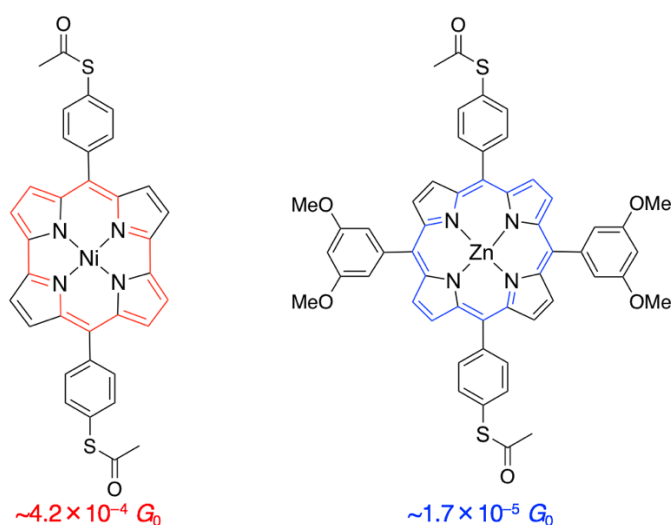


Figure 1-13. Thioester functionalized Ni(II) norcorrole and Ni(II) porphyrin.

In 2019, Nitschke and co-workers reported a cage with nanospaces surrounded by antiaromatic walls was developed by self-assembling Ni(II) norcorrole (Figure 1-14).²⁵ The self-assembled tetrahedral cage was constructed by complexation of six norcorrole-edges with four metal ions at the vertices. Calculations showed that the antiaromatic sites surrounding this nanospace enhance each other's magnetic effects. This prediction is confirmed by the ^1H nuclear magnetic resonance (NMR) signal of the guest molecule captured by the host, which shows a chemical shift of p to 24 ppm due to the antiaromatic deshielding effect of the surrounding rings.

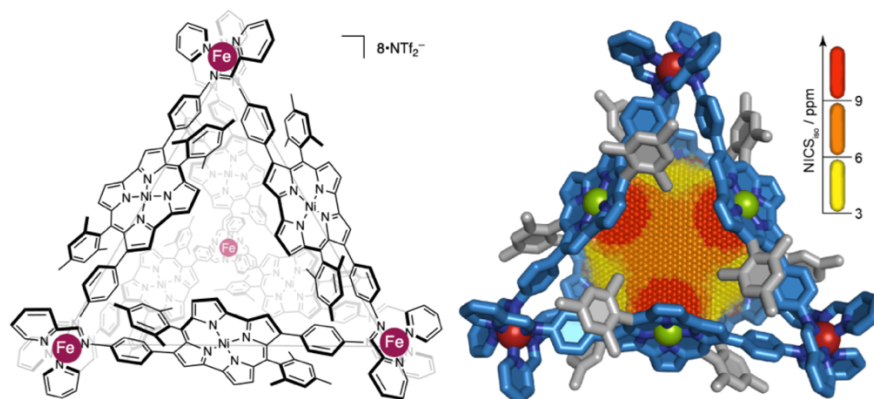


Figure 1-14. Structure of norcorrole nanocage and NICS calculation.

1-4. Overview of this thesis

As mentioned above, the synthesis of various antiaromatic molecules with a cyclic $4n\pi$ circuit has been developed. Furthermore, these antiaromatic molecules exhibited attractive functions derived from the narrow HOMO–LUMO gap. In particular, antiaromatic Ni(II) norcorroles have accelerated the research on antiaromatic molecules due to their high stability and facile large-scale synthesis. The electronic and steric modulation through peripheral modifications has been investigated to control the reactivity of norcorroles. The recently revealed high single molecular conductivity and close stacking of antiaromatic Ni(II) norcorroles are distinctly different from those of common aromatic compounds.

These previous studies of antiaromatic compounds have been limited to the single-molecule level. The author describes the integration of the antiaromatic Ni(II) norcorroles π -systems in this thesis to lead the chemistry of antiaromatic molecules to the next stage. (Figure 1-14).

Chapter 2 describes the synthesis and properties of Ni(II) dimethylnorcorrole, which can be handled without the bulky protection at the *meso*-positions.

Chapter 3 discloses the formation of a one-dimensional supramolecular polymer from an antiaromatic Ni(II) norcorrole with hydrogen bonding.

Chapter 4 discusses the formation of CT complexes of Ni(II) norcorrole with various acceptors.

Chapter 5 describes the reduction of Ni(II) *meso*-dimesitylnorcorrole to its isolable radical anion with cobaltocene ($\text{Co}^{\text{II}}\text{Cp}_2$).

Chapter 6 discloses the introduction of pentafluorophenyl groups to Ni(II) norcorrole at *meso*-positions.

The author believes that the present study on the integration of norcorroles would inspire the prospects of antiaromatic molecules-based materials.

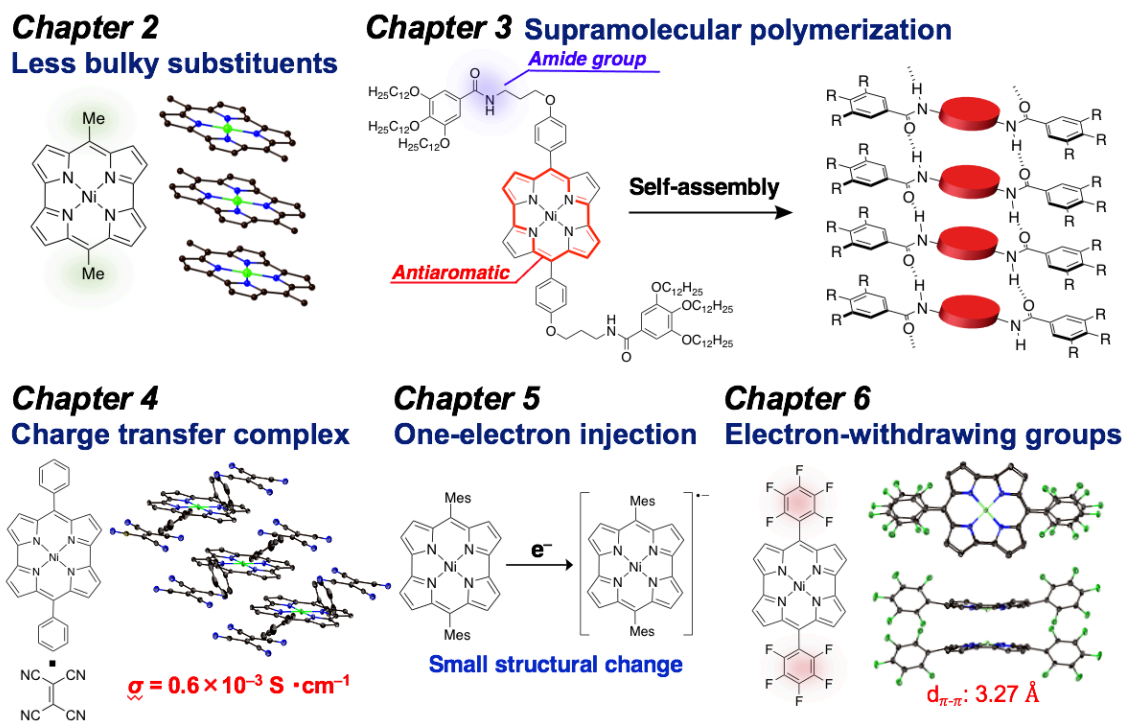


Figure 1-15. Overview of this thesis.

1-5. References

1. (a) Aromaticity and Other Conjugation Effects (Eds.: R. Gleiter, G. Haberhauser), Wiley-VCH, Weinheim, 2012. (b) Hückel, E. *Z. Physik* **1931**, *70*, 204.
2. (a) Harvey, R. G. Polycyclic Aromatic Hydrocarbons, Wiley-VCH, Weinheim, 1997. (b) Wu, J.; Pisula, W.; Müllen, K. *Chem. Rev.* **2007**, *107*, 718. (c) Narita, A.; Feng, X.; Müllen, K. *Chem. Rec.* **2014**, *15*, 295.
3. (a) Gavezzotti, A.; Desiraju, G. R. *Acta. Crystallogr. B Struct. Sci. Cryst.* **1988**, *44*, 427. (b) Desiraju, G. R.; Gavezzotti, A. *J. Chem. Soc., Chem. Commun.* **1989**, 621.
4. (a) Ferraris, John.; Cowan, D. O.; Walatka, V.; Perlstein, J. H. *J. Am. Chem. Soc.* **1973**, *95*, 948. (b) Shirakawa, H.; Louis, E. J.; MacDiarmid, A. G.; Chiang, C. K.; Heeger, A. J. *J. Chem. Soc., Chem. Commun.* **1977**, 578.
5. (a) Shirota, Y.; Kageyama, H. *Chem. Rev.* **2007**, *107*, 953. (b) Wang, C.; Dong, H.; Jiang, L.; Hu, W. *Chem. Soc. Rev.* **2018**, *47*, 422. (c) Wang, Y.; Sun, L.; Wang, C.; Yang, F.; Ren, X.; Zhang, X.; Dong, H.; Hu, W. *Chem. Soc. Rev.* **2019**, *48*, 1492.
6. (a) Jérôme, D.; Mazaud, A.; Ribault, M.; Bechgaard, K. *J. Phys. Lett.* **1980**, *41*, 95. (b) Bechgaard, K.; Carneiro, K.; Rasmussen, F. B.; Olsen, M.; Rindorf, G.; Jacobsen, C. S.; Pedersen, H. J.; Scott, J. C. *J. Am. Chem. Soc.* **1981**, *103*, 2440. (c) Saito, G.; Yoshida, Y. *Chem. Rec.* **2011**, *11*, 124.
7. Wörner, H. J.; Merkt, F. *J. Chem. Phys.* **2007**, *127*, 034303.
8. (a) Konishi, A.; Okada, Y.; Nakano, M.; Sugisaki, K.; Sato, K.; Takui, T.; Yasuda, M. *J. Am. Chem. Soc.* **2017**, *139*, 15284. (b) Yoshida, T.; Takahashi, K.; Ide, Y.; Kishi, R.; Fujiyoshi, J.; Lee, S.; Hiraoka, Y.; Kim, D.; Nakano, M.; Ikeue, T.; Yamada, H.; Shinokubo, H. *Angew. Chem. Int. Ed.* **2018**, *57*, 2209.
9. Sung, Y. M.; Oh, J.; Cha, W.-Y.; Kim, W.; Lim, J. M.; Yoon, M.-C.; Kim, D. *Chem.*

- Rev.* **2016**, *117*, 2257.
10. (a) Shin, J.-Y.; Yamada, T.; Yoshikawa, H.; Awaga, K.; Shinokubo, H. *Angew. Chem. Int. Ed.* **2014**, *53*, 3096. (b) Hwang, J.; Hagiwara, R.; Shinokubo, H.; Shin, J.-Y. *Mater. Adv.* **2021**, *2*, 2263.
 11. Maier, G. *Angew. Chem. Int. Ed.* **1988**, *27*, 309.
 12. (a) Hafner, K.; Süß, H. U. *Angew. Chem. Int. Ed. Engl.* **1973**, *12*, 575. (b) Chase, D. T.; Rose, B. D.; McClintock, S. P.; Zakharov, L. N.; Haley, M. M. *Angew. Chem. Int. Ed.* **2011**, *50*, 1127. (c) Shimizu, A.; Tobe, Y. *Angew. Chem. Int. Ed.* **2011**, *50*, 6906. (d) Iida, A.; Yamaguchi, S. *J. Am. Chem. Soc.* **2011**, *133*, 6952. (e) Wakamiya, A.; Mishima, K.; Ekawa, K.; Yamaguchi, S. *Chem. Commun.* **2008**, 579. (f) Maier, G.; Pfriederich, S., *Angew. Chem. Int. Ed.* **1978**, *17*, 519. (g) Hafner, K.; Stowasser, B.; Krimmer, H.-P.; Fischer, S.; Böhm, M. C.; Lindner, H. J. *Angew. Chem. Int. Ed. Engl.* **1986**, *25*, 630. (h) Matsuura, A.; Komatsu, K. *J. Am. Chem. Soc.* **2001**, *123*, 1768.
 13. Chase, D. T.; Rose, B. D.; McClintock, S. P.; Zakharov, L. N.; Haley, M. M. *Angew. Chem. Int. Ed.* **2010**, *123*, 1159.
 14. Saito, M. *Symmetry* **2010**, *2*, 950.
 15. Ohmae, T.; Nishinaga, T.; Wu, M.; Iyoda, M. *J. Am. Chem. Soc.* **2009**, *132*, 1066.
 16. Nishinaga, T.; Ohmae, T.; Aita, K.; Takase, M.; Iyoda, M.; Arai, T.; Kunugi, Y. *Chem. Commun.* **2013**, *49*, 5354.
 17. Bröring, M.; Köhler, S.; Kleeberg, C. Norcorrole. *Angew. Chem. Int. Ed.* **2008**, *47*, 5658.
 18. Ito, T.; Hayashi, Y.; Shimizu, S.; Shin, J.; Kobayashi, N.; Shinokubo, H. *Angew. Chem. Int. Ed.* **2012**, *51*, 8542.
 19. Nozawa, R.; Yamamoto, K.; Shin, J.-Y.; Hiroto, S.; Shinokubo, H. *Angew. Chem. Int.*

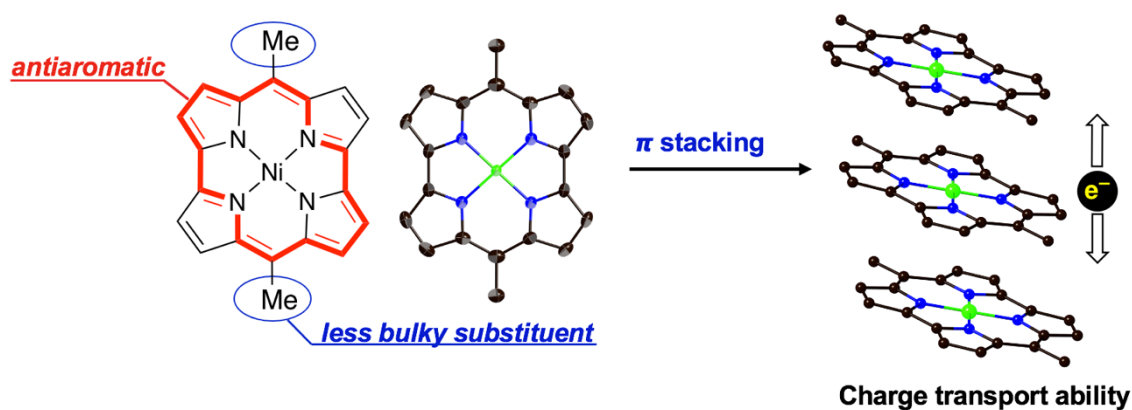
Chapter 1

Ed. **2015**, *54*, 8454.

20. Liu, S.; Tanaka, H.; Nozawa, R.; Fukui, N.; Shinokubo, H. *Chem. Eur. J.* **2019**, *25*, 7618.
21. Yoshida, T.; Sakamaki, D.; Seki, S.; Shinokubo, H. *Chem. Commun.* **2017**, *53*, 1112.
22. (a) Corminboeuf, C.; Schleyer, P. v. R.; Warner, P. *Org. Lett.* **2007**, *9*, 3263. (b) Bean, D. E.; Fowler, P. W. *Org. Lett.* **2008**, *10*, 5573.
23. (a) Nozawa, R.; Tanaka, H.; Cha, W.-Y.; Hong, Y.; Hisaki, I.; Shimizu, S.; Shin, J.-Y.; Kowalczyk, T.; Irle, S.; Kim, D.; Shinokubo, H. *Nat. Commun.* **2016**, *7*, 13620.
(b) Nozawa, R.; Kim, J.; Oh, J.; Lamping, A.; Wang, Y.; Shimizu, S.; Hisaki, I.; Kowalczyk, T.; Fliegl, H.; Kim, D.; Shinokubo, H. *Nat. Commun.* **2019**, *10*, 3576.
(c) Kawashima, H.; Ukai, S.; Nozawa, R.; Fukui, N.; Fitzsimmons, G.; Kowalczyk, T.; Fliegl, H.; Shinokubo, H. *J. Am. Chem. Soc.* **2021**, *143*, 10676.
24. Fujii, S.; Marqués-González, S.; Shin, J.-Y.; Shinokubo, H.; Masuda, T.; Nishino, T.; Arasu, N. P.; Vázquez, H.; Kiguchi, M. *Nat. Commun.* **2017**, *8*, 15984.
25. Yamashina, M.; Tanaka, Y.; Lavendomme, R.; Ronson, T. K.; Pittelkow, M.; Nitschke, J. R. *Nature* **2019**, *574*, 511.

Chapter 2

Synthesis and electron-transport property of stable antiaromatic Ni(II) norcorrole with the smallest *meso*-substituent



Contents

2-1. Introduction	24
2-2. Stability of 2-1 and 2-3	26
2-3. Synthesis	29
2-4. Electronic structure	35
2-5. Structural analysis	36
2-6. Charge transport properties	39
2-7. Summary of Chapter 2	42
2-8. References	43

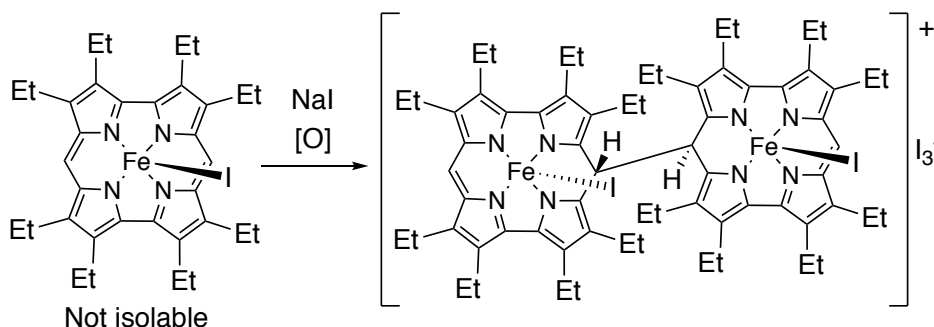
2-1. Introduction

Stability is a basic, yet the essential physical property of organic molecules. In particular, π -conjugated molecules with high stability are attractive because they not only enable the comprehensive studies on their fundamental properties relating to conjugation, charge transfer, and photophysical process, but also allow the fabrication of practical devices with high durability. The Hückel rule predicts that cyclic π -systems with $4n+2$ π -electrons gain substantial stability, so-called aromaticity.¹ They have been indispensable components of various practical materials such as plastics, medicines, dyes, and (opto)electronic devices.²

Planar cyclic π -systems with $4n$ π -electrons display antiaromaticity.^{3,4} Antiaromatic molecules are often unstable. Indeed, several antiaromatic molecules exhibit higher reactivities toward both electrophiles and nucleophiles than aromatic molecules.⁵ Consequently, the current molecular designs of antiaromatic compounds are invariably associated with thermodynamic and kinetic stabilization.⁶ However, thermodynamic stabilization strongly changes the electronic structures of the π -systems, which diminishes their intrinsic properties such as narrow HOMO–LUMO gap and multi-redox capabilities. Kinetic stabilization by sterically hindered peripheral substituents prevents effective intermolecular interactions in the condensed phases. This situation is not suitable for the fabrication of solid-state materials including organic rechargeable batteries⁷ and ambipolar semiconductors.⁸ In this regard, a stable antiaromatic molecule with a small peripheral substituent should be a fascinating research target.

As mentioned in Chapter 1, the preparation of a β -octaethylnorcorrole Fe(III) complex was accomplished by Bröring and co-workers (Scheme 2-1).⁹ Unfortunately, the Fe(III) norcorrole was not isolable because rapid dimerization of Fe(III) norcorrole

afforded the corresponding dinorcorrole.



Scheme 2-1. Dimerization of Fe(III) norcorrole complex.

In contrast, *meso*-dimesitylnorcorrole Ni(II) complex **2-1** was stable under ambient conditions.¹⁰ These results revealed that the bulky mesityl groups kinetically stabilize the inherently reactive *meso*-positions of norcorroles. Nevertheless, recent studies demonstrated that smaller peripheral substituents such as phenyl and isopropyl groups are sufficient to yield bench-stable derivatives **2-2** and **2-3**.¹¹ However, the minimum substituent to stabilize the antiaromatic norcorrole core has remained unclear.

In Chapter 2, the author describes the synthesis and structure of **2-4**. In addition, the author also describes the consideration of the introduction of hydrogen atoms for *meso*-position. The small methyl substituents realize a dense and long-range π -stacking in its solid state, which results in the superior electron-transporting ability to previously reported Ni(II) norcorroles.

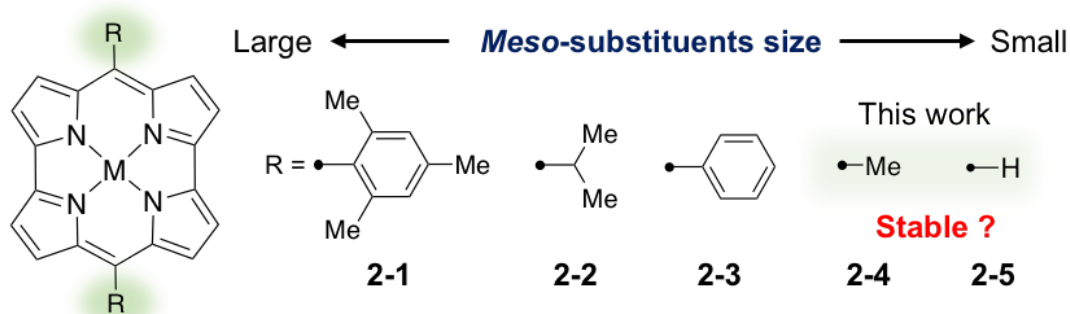


Figure 2-1. Structures of Ni(II) norcorroles and the *meso*-substituents size.

2-2. Stability of 2-1 and 2-3

Because Ni(II) norcorroles exhibit the distinct antiaromaticity, they are essentially unstable and reactive. The current research started with comparison of the stability of Ni(II) *meso*-dimesitylnorcorrole **2-1** and Ni(II) *meso*-diphenylnorcorrole **2-3** upon the exposure to air, water, silica-gel, and heat. The solid samples of **2-1** and **2-3** were stored for 2–4 months under ambient conditions, resulting in no detectable degradation. The stability of **2-1** and **2-3** in solution was also examined by monitoring their ¹H NMR spectra in CDCl₃ after the storage under ambient conditions for 1 week. This experiment again confirmed no detectable spectral change (Figure 2-2, 2-3; Table 2-1). Norcorroles **2-1** and **2-3** were also robust to the conventional purification such as washing with water and silica-gel chromatography (Fig. 2-4 (a), (b)). Solutions of **2-1** and **2-3** in toluene were heated at 80 °C under air for 16 h to result in recovery of these molecules in almost quantitative yields (Figure 2-4 (c)). These observations indicate that relatively small phenyl groups are enough to stabilize the antiaromatic norcorrole core, enabling the treatment under ambient conditions with no special care. These results encouraged the author to quest for the minimum substituent to stabilize the antiaromatic norcorrole core.

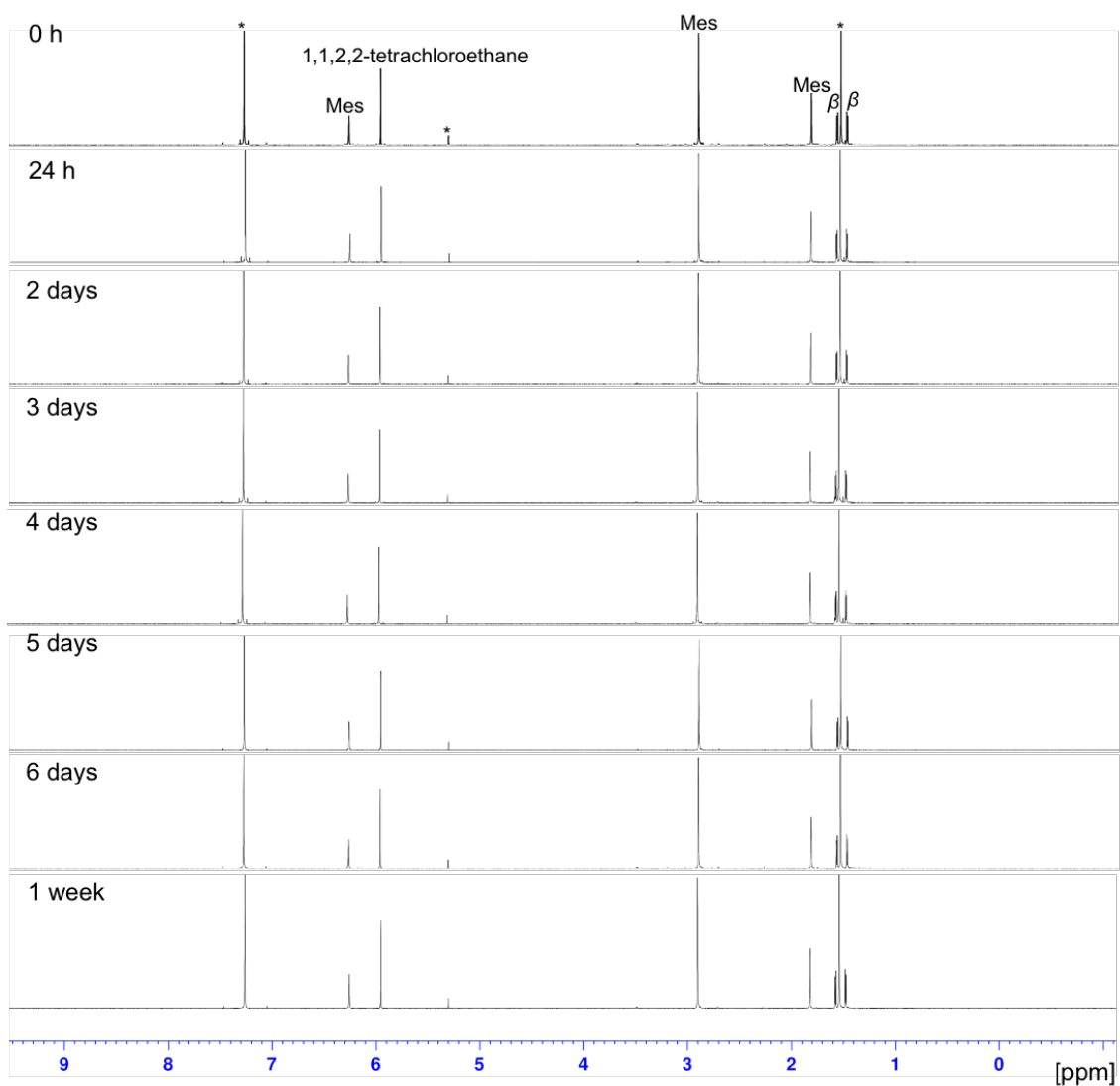


Figure 2-2. Change of ¹H NMR (500 MHz) spectra of 2-1 in CDCl₃ at 25 °C (*solvent peaks).

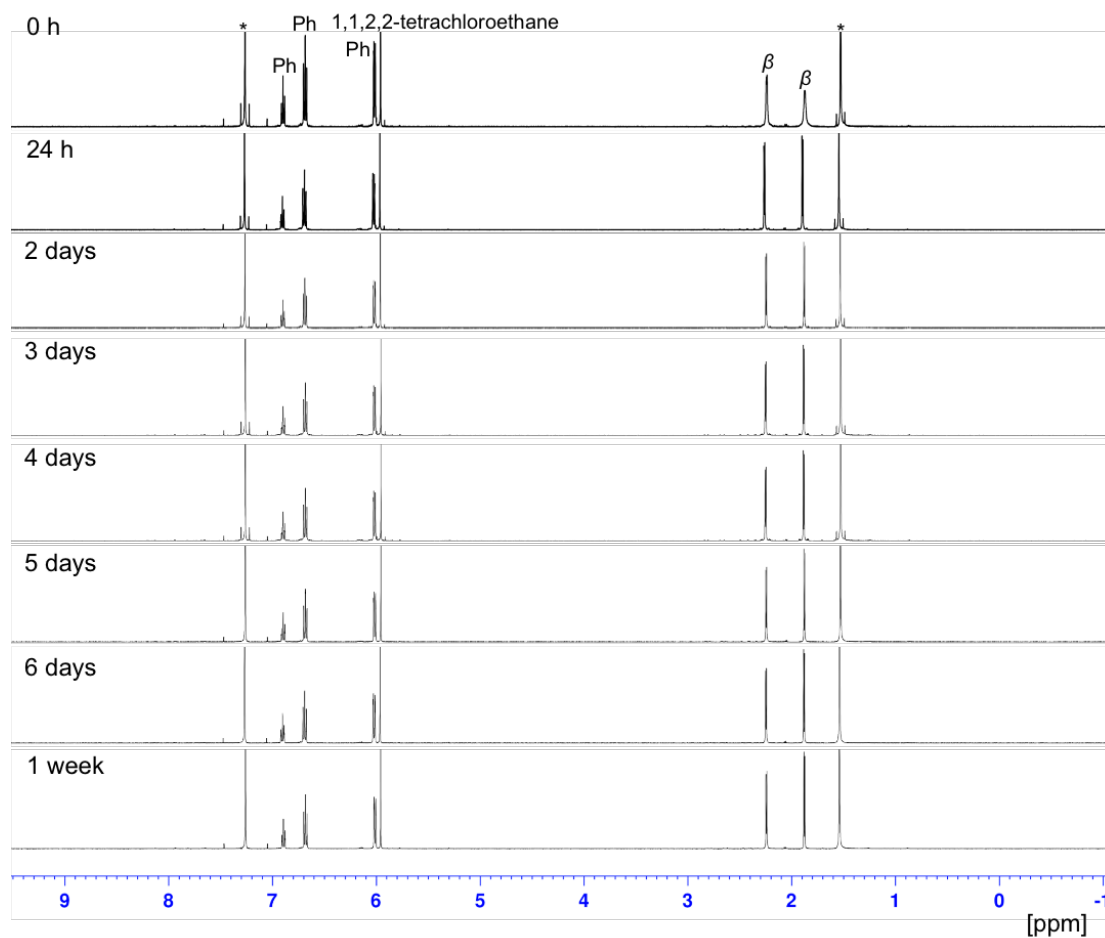


Figure 2-3. Change of ^1H NMR (500 MHz) spectra of **2-3** in CDCl_3 at $25\text{ }^\circ\text{C}$ (*solvent peaks).

Table 2-1. The relative integrated intensities^[a] of the ^1H NMR signals of **2-1** and **2-3**.

Time	2-1 β proton (1.57 ppm)	2-3 β proton (2.24 ppm)
0 h	1.13	1.19
24 h	1.13	1.23
2 days	1.19	1.22
3 days	1.13	1.20
4 days	1.12	1.20
5 days	1.11	1.18
6 days	1.11	1.17
1 week	1.11	1.17

[a] These values were calculated on the basis of the integral values of the signal of the internal standard (1,1,2,2-tetrachloroethane).

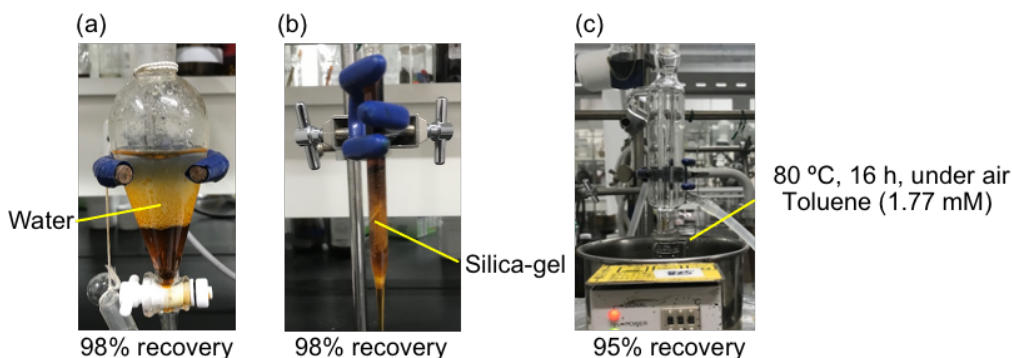


Figure 2-4. Treatment of **2-3** with (a) water and (b) silica-gel. (c) Heating of **2-3** in toluene.

2-3. Synthesis

In the norcorrole reported by Bröring and co-workers the central metal is iron, but in this case the central metal is nickel, so the electronic structure and stability should be different. Then, the author set Ni(II) *meso*-unsubstituted norcorrole **2-5** as the first target molecule.

Bromination of dipyrromethane **2-6** with N-bromosuccinimide (NBS) followed by oxidation with 2,3-dichloro-5,6-dicyano-*p*-benzoquinone (DDQ) afforded dipyrromethene **2-7**, which was unstable under aerobic conditions. The reaction mixture was subjected to metalation with Ni(OAc)₂·4H₂O without purification to provide the corresponding dipyrin Ni(II) complex **2-9** in 11% yield in three steps (Scheme 2-2). Recrystallization of **2-9** from hexane afforded a single crystal suitable for X-ray diffraction analysis, which unambiguously confirmed the molecular structure of **2-9** (Figure 2-5). A reductive coupling of **2-9** with Ni(cod)₂ was attempted, but **2-5** could not be detected by ¹H NMR and MS spectra. From the MALDI-TOF-MS spectra of the reaction mixture (Figure 2-6), the molecular weight of a dimerization product of **2-10** was observed as the major peak, which was linked to the *meso-meso* and β-β positions. This

result implies that the *meso*-position of Ni(II) *meso*-unsubstituted norcorrole is highly reactive as well as that of Fe(III) *meso*-unsubstituted norcorrole.

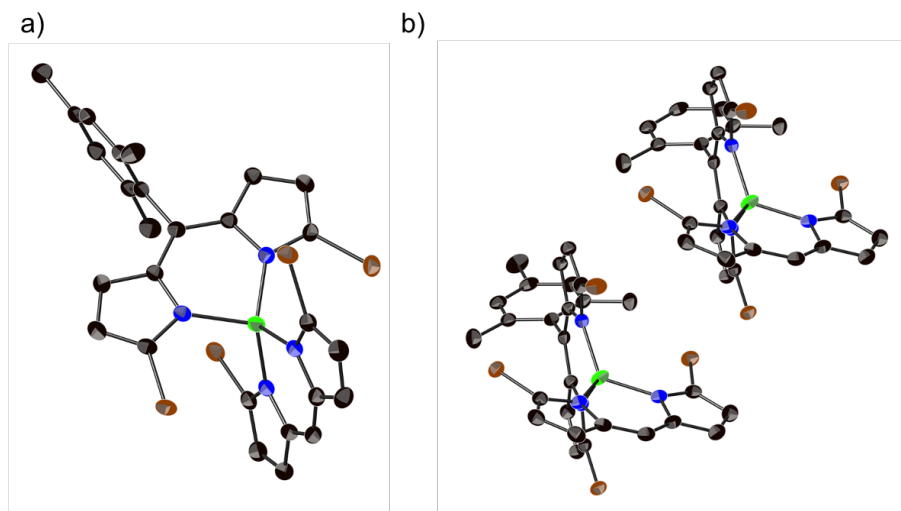
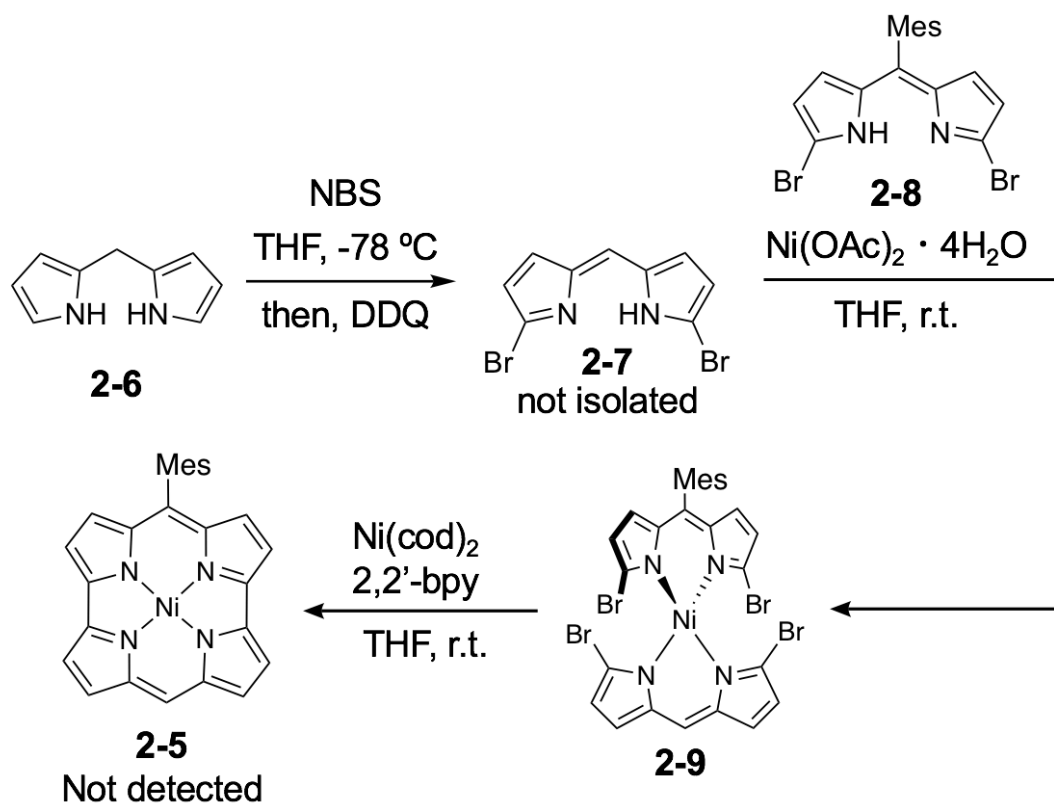


Figure 2-5. (a) Top and (b) side views of the molecular structure of **2-9** (atomic displacement parameter set at 50% probability; all hydrogen atoms omitted for clarity).



Scheme 2-2. Synthesis of Ni(II) *meso*-unsubstituted norcorrole **2-5**.

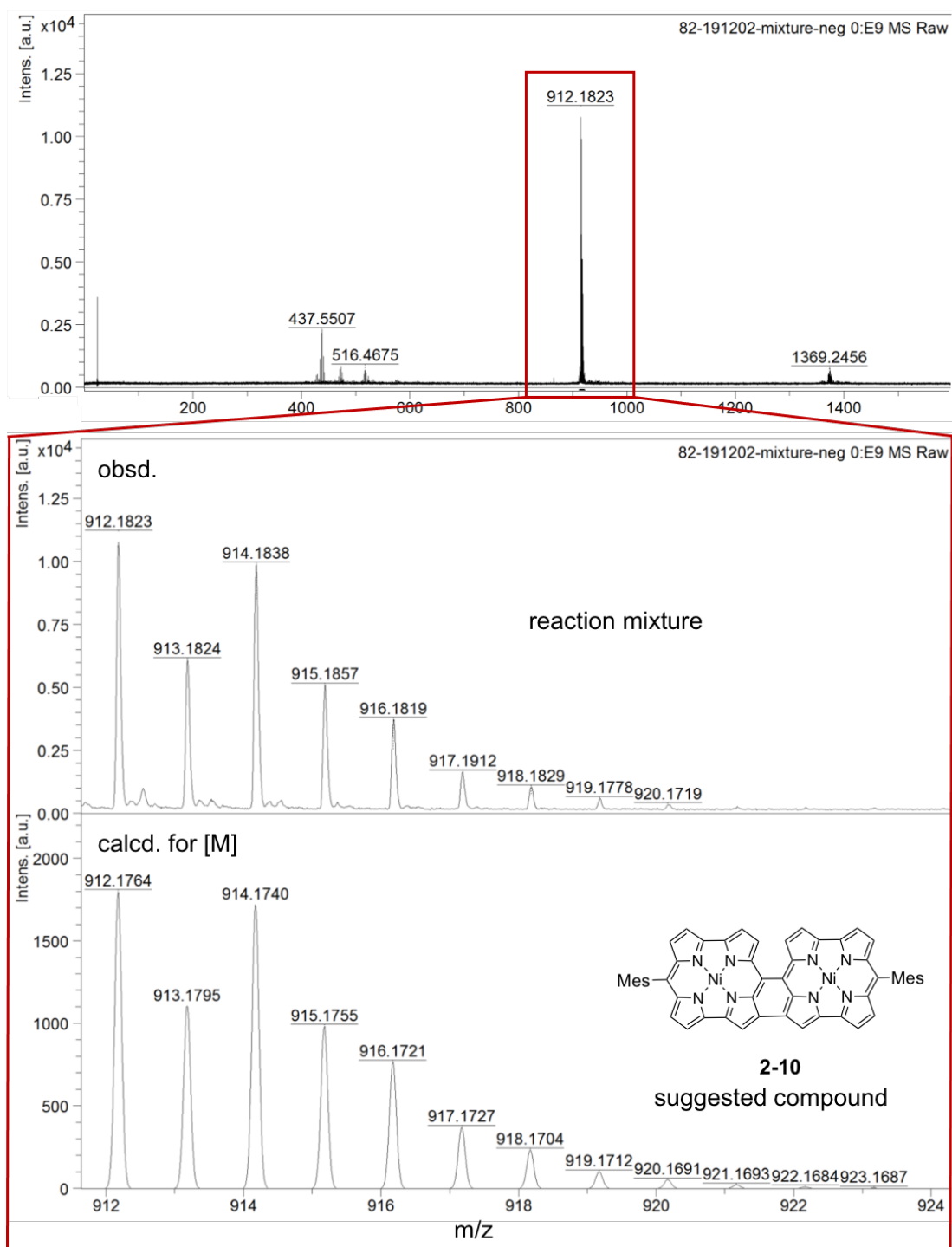
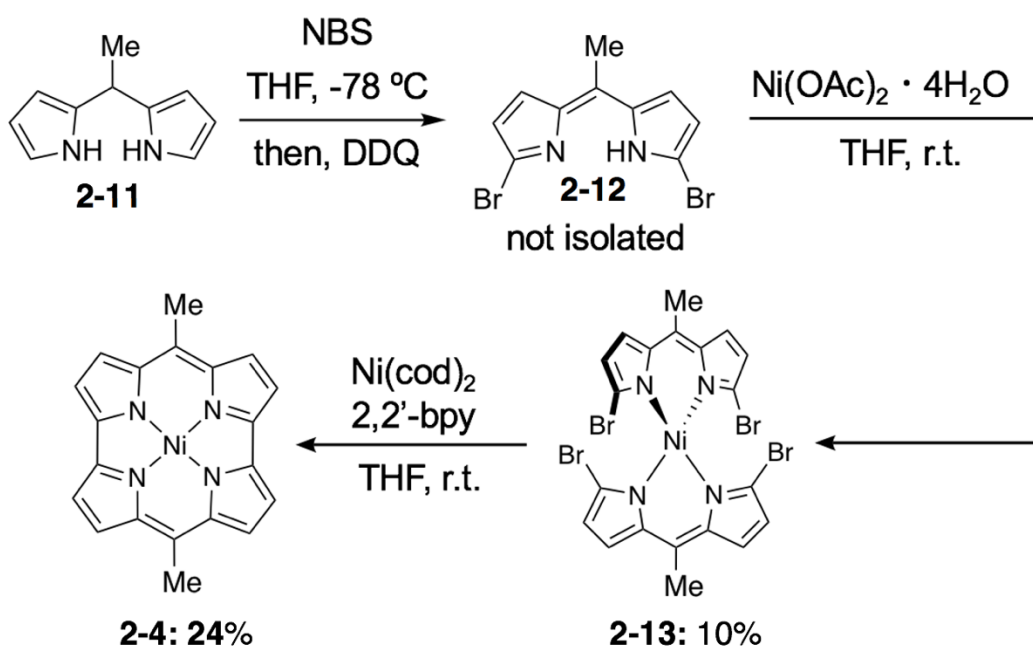


Figure 2-6. MALDI-TOF-MS spectra of the reaction mixture of the reductive coupling of 2-9.

Based on the above discussion of the introduction of hydrogen atom into the *meso*-position, methyl groups were chosen as smaller substituents. The author chose Ni(II) *meso*-dimethylnorcorrole **2-4** as the next target molecule.

Bromination of 5-methyldipyrrromethane **2-11** with NBS followed by oxidation with DDQ afforded dipyrromethene **2-12**, which was unstable under aerobic conditions. The reaction mixture was subjected to metalation with Ni(OAc)₂·4H₂O without purification to provide the corresponding dipyrin Ni(II) complex **2-13** in 10% yield in three steps (Scheme 2-3). Reductive coupling of **2-13** provided Ni(II) *meso*-dimethylnorcorrole **2-4** in 24% yield. Norcorrole **2-4** showed low solubility in various solvents, e.g. 0.2 g/L in CH₂Cl₂.



Scheme 2-3. Synthesis of Ni(II) *meso*-dimethylnorcorrole **2-4**.

Figure 2-7 displays the ¹H NMR spectrum of Ni(II) *meso*-dimethylnorcorrole **2-4** in CDCl₃. The signals due to β-protons appeared at 3.11 and 2.42 ppm, which were obviously upfield-shifted from those of normal pyrroles (ca. 6–7 ppm). In addition, the

signal due to the *meso*-methyl protons was observed at -0.96 ppm.

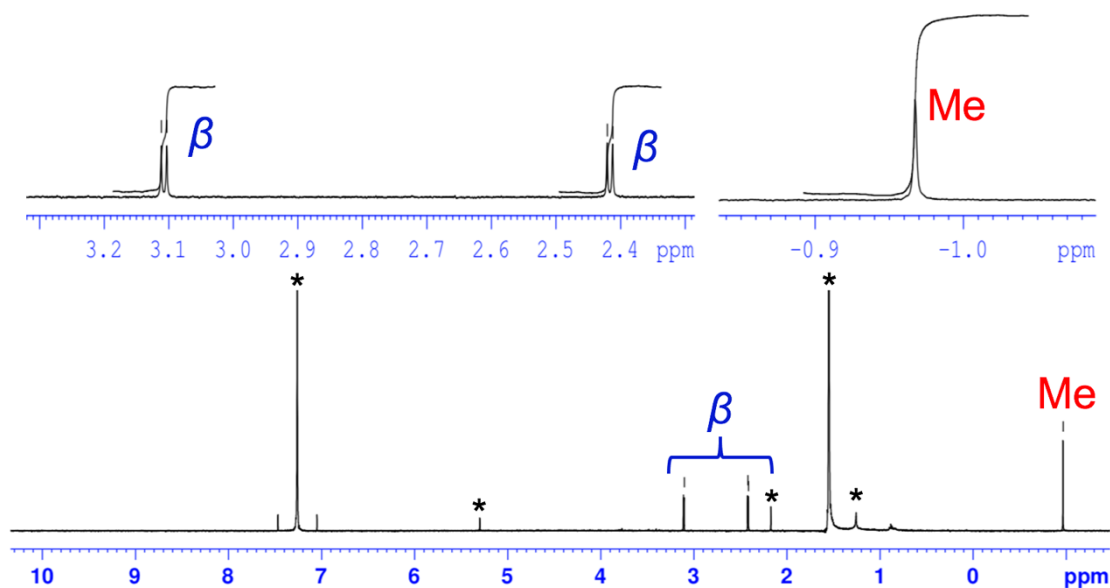


Figure 2-7. ^1H NMR (500 MHz) spectra of **2-4** in CDCl_3 at $25\text{ }^\circ\text{C}$ (*solvent peaks).

Importantly, Ni(II) *meso*-dimethylnorcorrole **2-4** was sufficiently stable under ambient conditions. The storage of the solid samples under ambient conditions for at least 1 month resulted in no detectable decomposition. In addition, a solution of **2-4** in CH_2Cl_2 was monitored by the absorption spectra, suggesting that **2-4** underwent negligible degradation (ca. 3.4%) after 24 h under ambient conditions (Figure 2-8). According to this result, the half-life time of **2-4** in a CH_2Cl_2 solution was estimated to be about two weeks. Furthermore, Ni(II) *meso*-dimethylnorcorrole **2-4** was robust to silica-gel chromatography and required no special treatment during the work-up process. It is worth noting that the apparent degradation was observed after heating the toluene solution at $80\text{ }^\circ\text{C}$, in which ca. 50% of **2-4** underwent decomposition after 12 h (Figure 2-9). Since none of *meso*-unsubstituted norcorroles have been isolated to date, the methyl group is the smallest substituent to stabilize the antiaromatic norcorrole core.

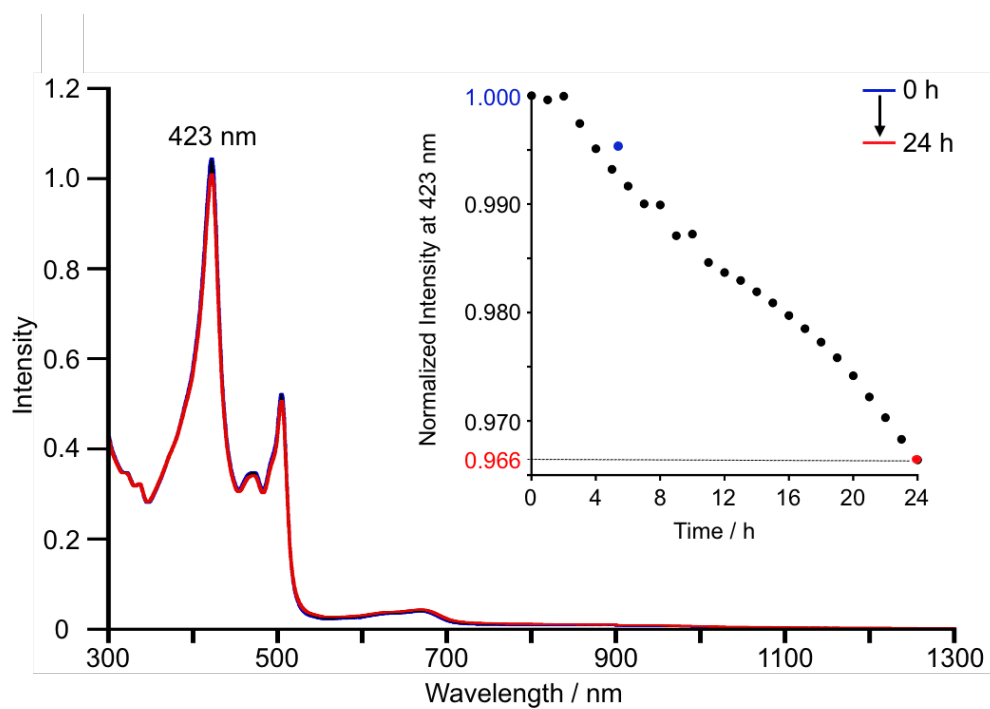


Figure 2-8. Time-dependent change in UV/vis/NIR absorption spectra of **2-4** in CH₂Cl₂ at 25 °C. Inset shows the plots of the intensities at 423 nm.

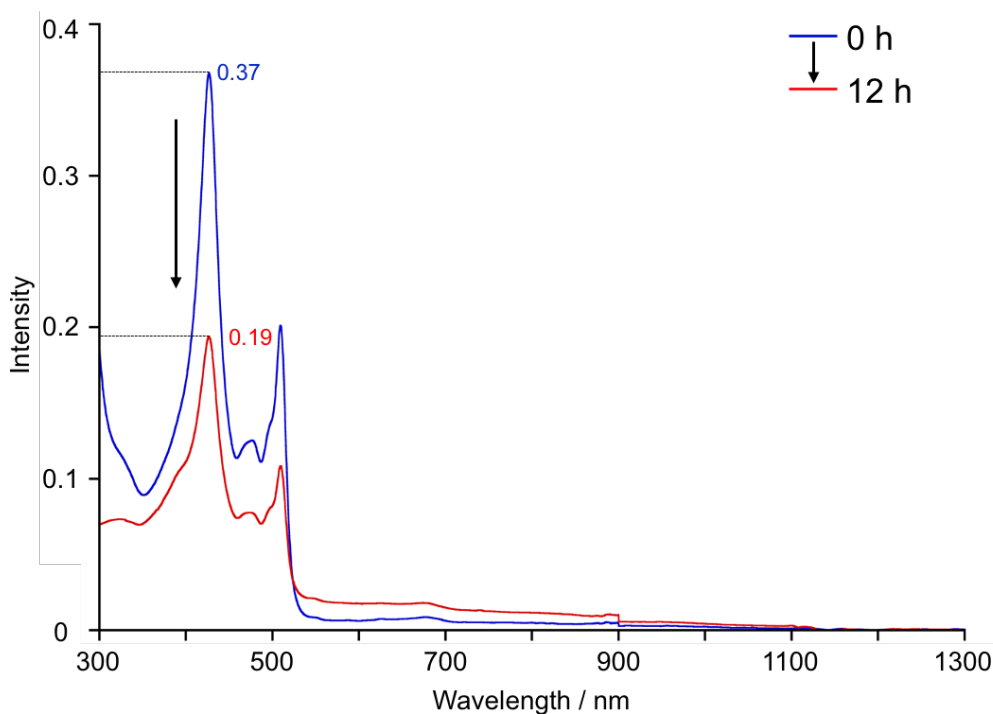


Figure 2-9. UV/vis/NIR absorption spectrum of **2-4** in toluene at 80 °C at 0 min and after heating for 12 h at 80 °C.

2-4. Electronic structure

To evaluate the antiaromaticity of Ni(II) *meso*-dimethylnorcorrole **2-4**, NICS(1) values¹² are calculated all rings. Then, positive values from 2.8–31.2 ppm for all rings were obtained (Figure 2-10). This result is consistent with the ¹H NMR results.



Figure 2-10. NICS(1) values of **2-4**. Calculations were carried out at the B3LYP/6-31G(d)+SDD level of theory.

The UV/Vis/NIR absorption spectrum of **2-4** in CH₂Cl₂ shows peaks at 422, 472, and 505 nm as well as a weak absorption band tailing to the NIR region (Figure 2-11). This spectral feature resembles those of other norcorrole derivatives. These results indicate the negligible perturbation of the methyl groups on the electronic structure, especially the antiaromaticity, of the norcorrole core.

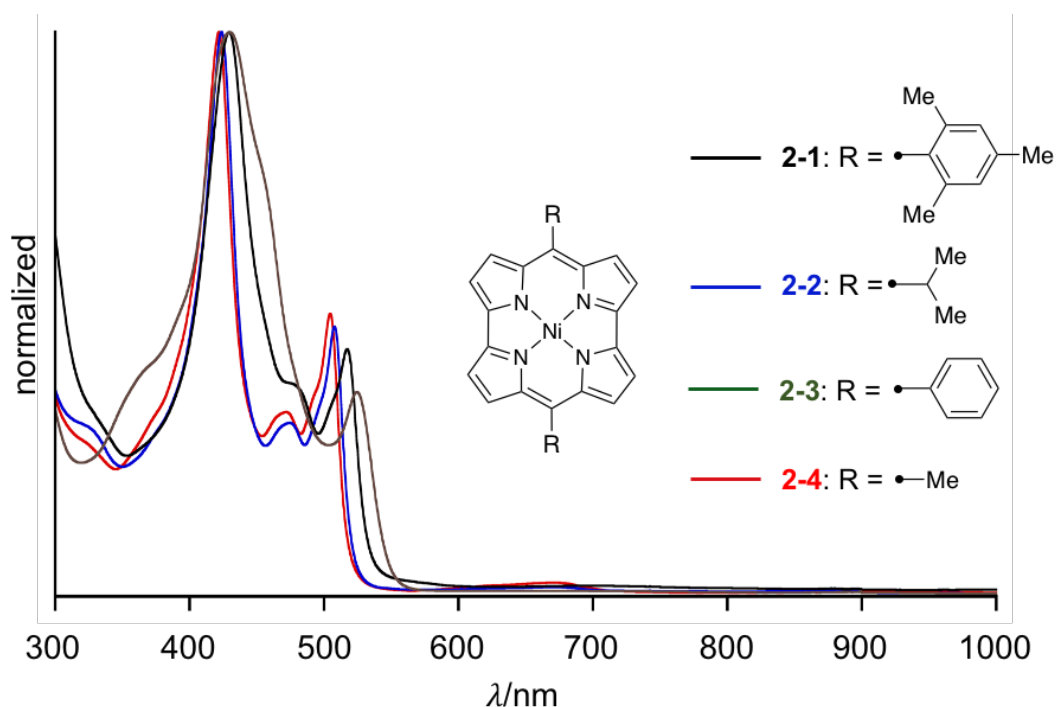


Figure 2-11. UV/Vis/NIR absorption spectra of **2-1** (black), **2-2** (blue), **2-3** (green), and **2-4** (red) in CH_2Cl_2 . λ = wavelength.

2-5. Structural analysis

Figure 2-12 shows the crystal structure of Ni(II) *meso*-dimethylnorcorrole **2-4**. In the crystal, **2-4** exhibits almost planar structure with the mean plane deviation (MPD)¹³ of 0.01 Å, which is comparable to those of other norcorroles **2-1**, **2-2**, and **2-3** (0.03–0.04 Å). The harmonic oscillator model of aromaticity (HOMA)¹⁴ value is 0.32, which is also comparable to those of other norcorroles **2-1**, **2-2**, and **2-3** (0.43–0.46). These results suggest the negligible perturbation by the methyl groups on the structure of the norcorrole core.

In the crystal of **2-4**, one-dimensional columnar π -stacking with an interplanar distance of 3.31 Å is observed (Figure 2-12 b). The short contact between two norcorrole core in **2-4** is striking because π - π stacking distances typically range from 3.4 to 3.6 Å.

On the other hand, each norcorrole unit of **2-1** is separated due to bulky mesityl groups (Figure 2-13). Diisopropylnorcorrole **2-2** also shows no effective overlap of π -systems (Figure 2-14). Diphenylnorcorrole **2-3** adopts a triple-decker stacking structure with the short π - π distance of 3.15 Å. However, the stacked trimers do not form continuous π -stacking (Figure 2-15). Consequently, dense and long-range π -stacking is only observed in the crystal of **2-4**.

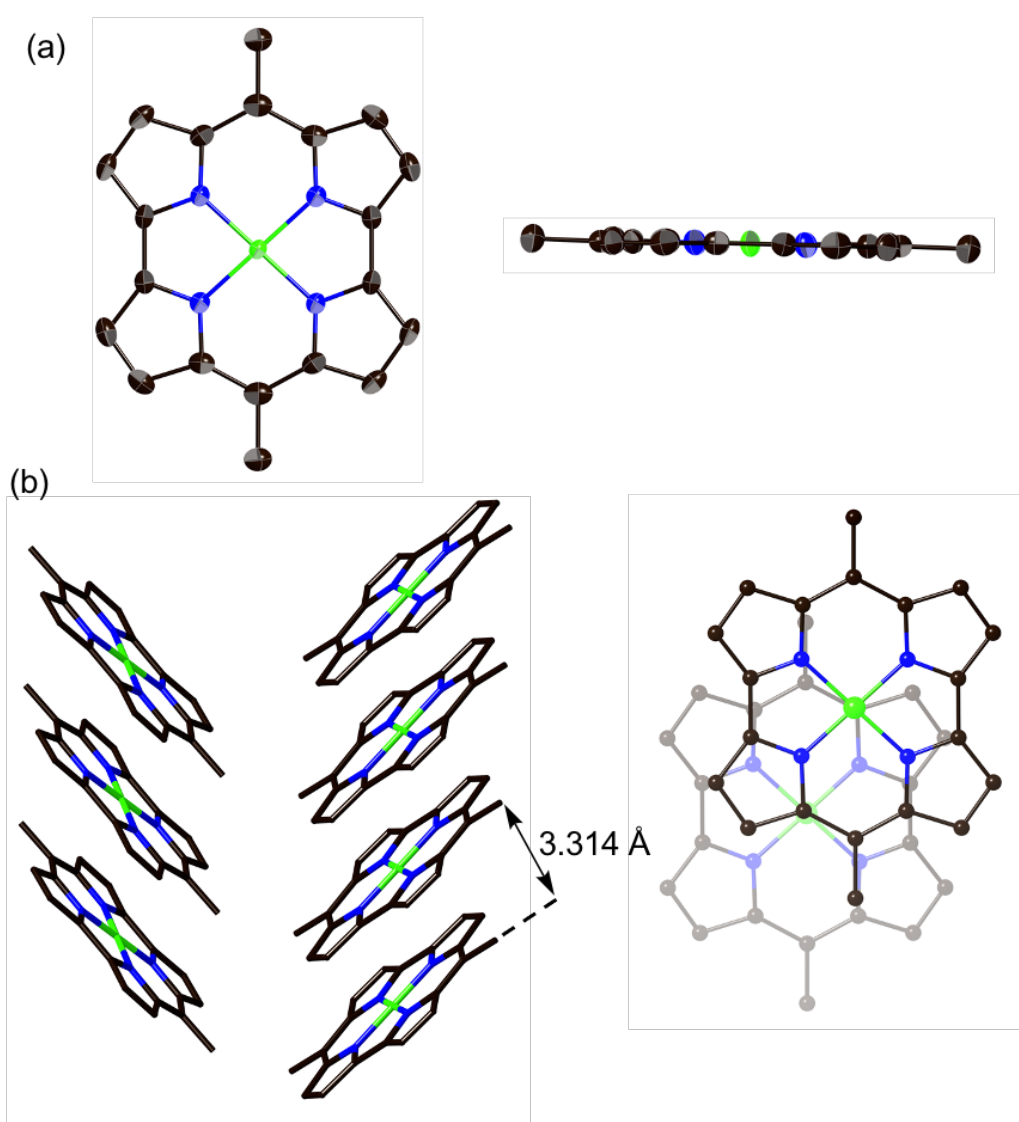


Figure 2-12. X-ray crystal structure of *meso*-dimethylnorcorrole **2-4**. (a) Single-molecule structure and (b) packing structure. Thermal ellipsoids are drawn at the 50% probability level. All hydrogen atoms are omitted for clarity.

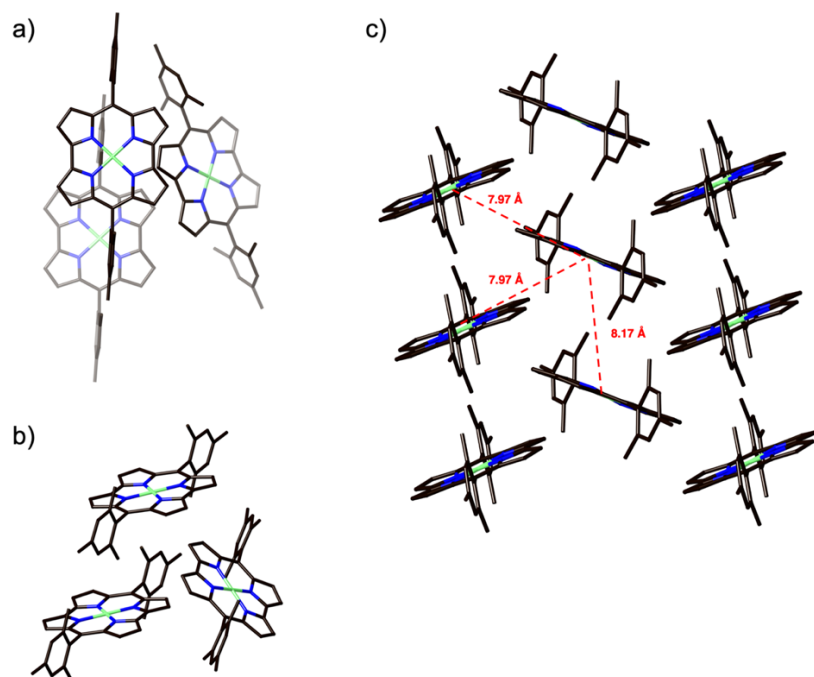


Figure 2-13. Packing diagrams of 2-1 as well as their intermolecular distances. The intermolecular distance is defined as the distance between two nickel centers.

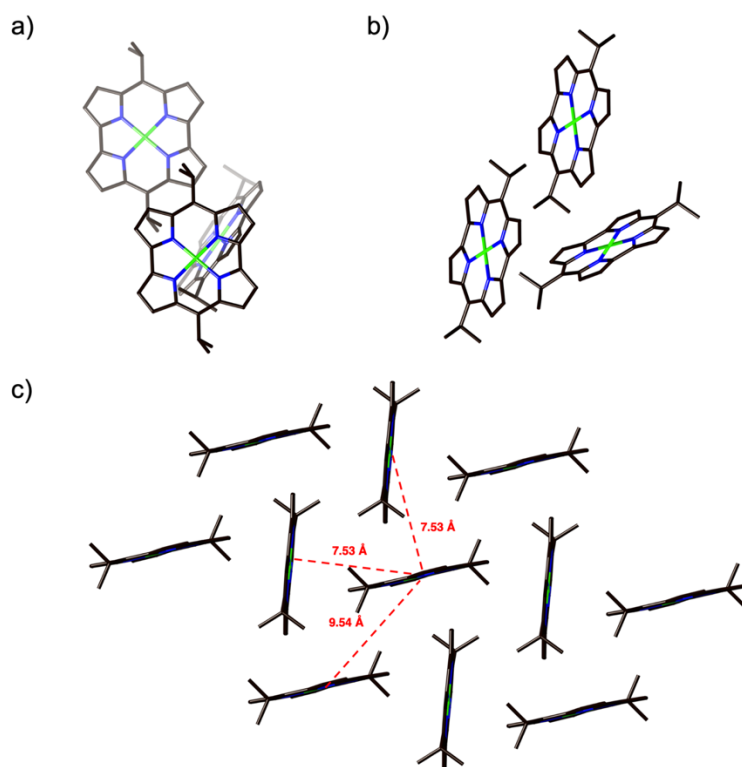


Figure 2-14. Packing diagrams of 2-2 as well as their intermolecular distances. The intermolecular distance is defined as the distance between two nickel centers.

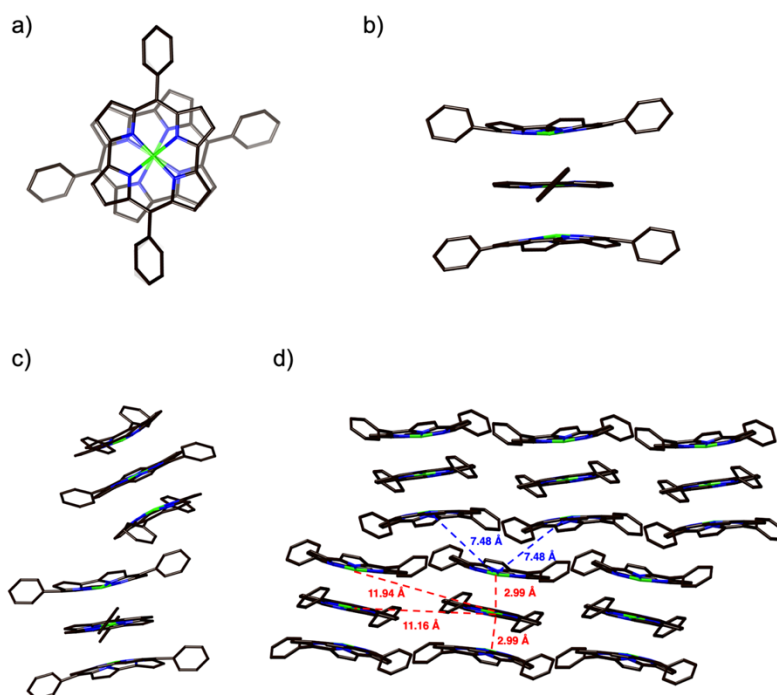


Figure 2-15. Packing diagrams of **2-3** as well as their intermolecular distances. The intermolecular distance is defined as the distance between two nickel centers.

2-6. Charge transport properties

Norcorrole exhibits a deep-lying LUMO level due to its antiaromaticity.¹⁵ The one-dimensional columnar alignment in a slipped parallel manner of **2-4** inspired us the stacking axes as potential and stable electron-conducting pathways. Indeed, DFT calculations predicted that the π -stacking afforded a large intermolecular transfer integral of 64 meV (Figure 2-16). In contrast, the calculated transfer integrals in **2-1** and **2-2** were less than 14.2 meV. Ni(II) *meso*-diphenylnorcorrole **2-3** showed a large transfer integral (130.9 meV) between two stacking macrocycles. However, the transfer integrals between neighboring triple stacks were small (<27.3 meV), suggesting the lack of an effective electron-conducting pathway in **2-3**.

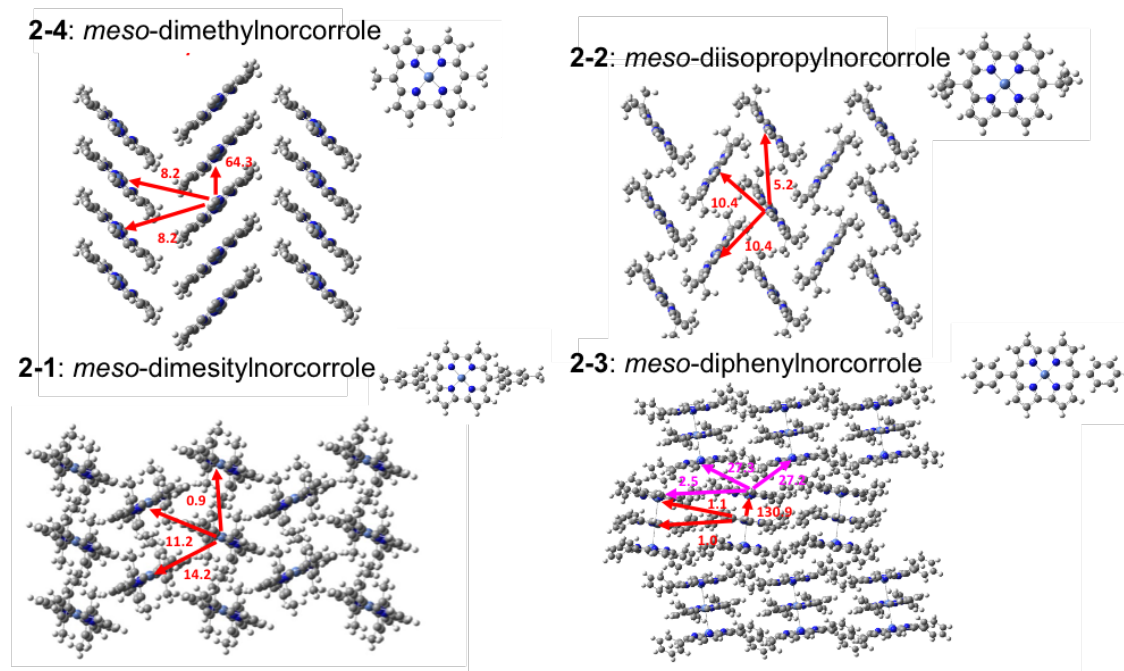


Figure 2-16. Effective transfer integrals (meV) of LUMO calculated for nearest intralayer neighbors in the crystal structure of **2-4**, **2-2**, **2-1**, and **2-3**.

The author examined the electronic photo-conduction of **2-1**, **2-2**, **2-3**, and **2-4** by flash-photolysis time-resolved microwave conductivity (FP-TRMC) measurement in their microcrystalline states.¹⁶ Electrodeless photocarrier injection was performed upon excitation at 355 nm where the electronic transitions of the series of molecules are minimum, securing the homogeneous photocarrier distribution in their crystalline states. The observed photoconductivity transients were shown in Figure 2-17. Dimethylnorcorrole **2-4** marked the highest photoconductivity over all time regime up to $\sim 100 \mu\text{s}$. Kinetic trace of **2-4** exhibits clearly double exponential decay with the first order rate constants of 4×10^6 and $\sim 10^4 \text{ s}^{-1}$. To assess the major contribution from photo-generated electrons and holes onto the columnar stacking of **2-4**, the effects of O_2 on conductivity transients were observed as shown in Figure 2-18. Conductivity signals were significantly suppressed and quenched by O_2 particularly for the initial decay in the

transients, which is suggestive of the major contribution of electrons in photoconductivity as presumed by the LUMO levels of norcorrole cores. It should be noted that quenching by O₂ was indistinct for the longer decay component in conductivity transients. This may be due to the conductivity transients observed at >1 μs reflected mainly by the local motion of electrons within μm-sized crystallites of **2-4**, followed by surface quenching by O₂. One order of magnitude higher photoconductivity was recorded for **2-4** in contrast to negligible change in conductivity of **2-1**, **2-2**, and **2-2**. This is the case of impacts by the methyl substitution onto the dense crystalline structure and hence onto the stable electronic conducting pathways.

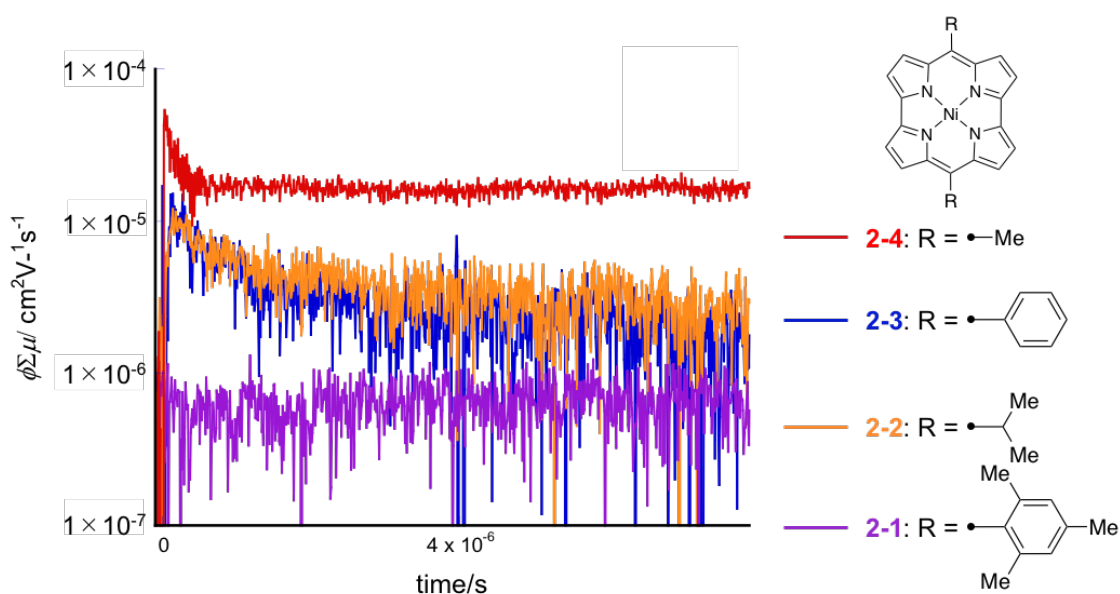


Figure 2-17. Photoconductivity transients recorded in microcrystalline **2-3** (blue), **2-2** (orange), **2-1** (violet), and **2-4** (red), respectively upon excitation at 355 nm, $0.2\text{--}1.3 \times 10^{15}$ photons cm^{-2} , RT.

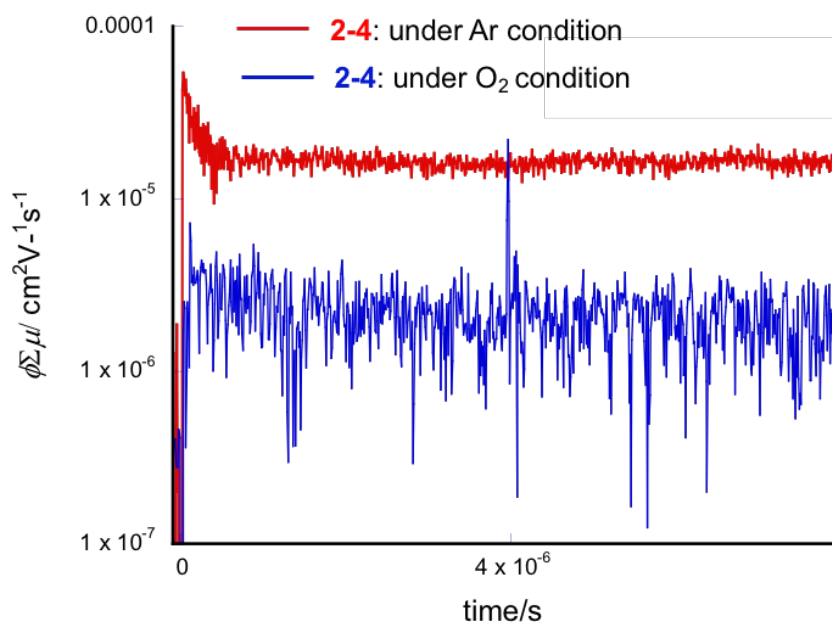


Figure 2-18. Photoconductivity transients recorded in microcrystalline **2-4** under argon (red) and O₂ (blue) saturated environment, respectively upon excitation at 355 nm, $0.2\text{--}1.3 \times 10^{15}$ photons cm⁻², r.t.

2-7. Summary of Chapter 2

In summary, the author investigated the stability of several norcorrole Ni(II) complexes toward the exposure to air, water, silica-gel, and heat. Furthermore, the author achieved the synthesis of Ni(II) *meso*-dimethylnorcorrole **2-4**, which was considerably stable under ambient conditions despite its distinct antiaromaticity. Currently, the methyl group is the smallest substituent to afford a stable norcorrole Ni(II) complex. Importantly, **2-4** exhibited superior electron-transporting ability to other Ni(II) norcorroles owing to its dense and long-range π -stacking. The current research should offer new insight into the design of stable antiaromatic molecules with small peripheral substituents.

2-8. References

1. (a) Aromaticity and Other Conjugation Effects (Eds.: R. Gleiter, G. Haberhauser), Wiley-VCH, Weinheim, 2012. (b) Hückel, E. *Z. Physik* **1931**, *70*, 204.
2. Functional Organic Materials (Eds.: Müller, T. J. J.; Bunz, U. H. F.), Wiley-VCH, Weinheim, 2007.
3. Reviews: (a) Wiberg, K. B. *Chem. Rev.* **2001**, *101*, 1317. (b) Nishinaga, T.; Ohmae, T.; Iyoda, M. *Symmetry* **2010**, *2*, 76. (c) Braunschweig, H.; Kupfer, T. *Chem. Commun.* **2011**, *47*, 10903. (d) Hopf, H. *Angew. Chem. Int. Ed.* **2013**, *52*, 12224. (e) Rosenberg, M.; Dahlstrand, C.; Kilså, K.; Ottosson, H. *Chem. Rev.* **2014**, *114*, 5379. (f) Frederickson, C. K.; Rose, B. D.; Haley, M. M. *Acc. Chem. Res.* **2017**, *50*, 977. (g) Sung, Y. M.; Oh, J.; Cha, W.-Y.; Kim, W.; Lim, J. M.; Yoon, M.-C.; Kim, D. *Chem. Rev.* **2017**, *117*, 2257.
4. Selected examples: (a) Cissell, J. A.; Vaid, T. P.; Rheingold, A. L. *J. Am. Chem. Soc.* **2005**, *127*, 12212. (b) Yamamoto, Y.; Hirata, Y.; Kodama, M.; Yamaguchi, T.; Matsukawa, S.; Akiba, K.; Hashizume, D.; Iwasaki, F.; Muranaka, A.; Uchiyama, M.; Chen, P.; Kadish, K. M.; Kobayashi, N. *J. Am. Chem. Soc.* **2010**, *132*, 12627. (c) Stępień, M.; Szyszko, B.; Latos-Grażyński, L. *J. Am. Chem. Soc.* **2010**, *132*, 3140. (d) Ohmae, T.; Nishinaga, T.; Wu, M.; Iyoda, M. *J. Am. Chem. Soc.* **2010**, *132*, 1066. (e) Sung, Y. M.; Yoon, M.-C.; Lim, J. M.; Rath, H.; Naoda, K.; Osuka, A.; Kim, D. *Nat. Chem.* **2015**, *7*, 418. (f) Cao, J.; London, G.; Dumele, O.; von Wantoch Rekowski, M.; Trapp, N.; Ruhlmann, L.; Boudon, C.; Stanger, A.; Diederich, F. *J. Am. Chem. Soc.* **2015**, *137*, 7178. (g) Frederickson, C. K.; Zakharov, L. N.; Haley, M. M. *J. Am. Chem. Soc.* **2016**, *138*, 16827. (h) Satoh, T.; Minoura, M.; Nakano, H.;

- Furukawa, K.; Matano, Y. *Angew. Chem. Int. Ed.* **2016**, *55*, 2235. (i) Oshima, H.; Fukazawa, A.; Yamaguchi, S. *Angew. Chem. Int. Ed.* **2017**, *56*, 3270. (j) Nishiyama, A.; Fukuda, M.; Mori, S.; Furukawa, K.; Fliegl, H.; Furuta, H. *Angew. Chem. Int. Ed.* **2018**, *57*, 9728. (k) Zou, Y.; Zeng, W.; Gopalakrishna, T. Y.; Han, Y.; Jiang, Q.; Wu, J. *J. Am. Chem. Soc.* **2019**, *141*, 7266.
5. (a) Kaiser, R.; Hafner, K. *Angew. Chem. Int. Ed. Engl.* **1973**, *12*, 337. (b) Eisch, J. J.; Galle, J. E. *J. Am. Chem. Soc.* **1975**, *97*, 4436. (c) Nishinaga, T.; Uto, T.; Inoue, R.; Matsuura, A.; Treitel, N.; Rabinovitz, M.; Komatsu, K. *Chem. Eur. J.* **2008**, *14*, 2067. (d) Fan, C.; Mercier, L. G.; Piers, W. E.; Tuononen, H. M.; Parvez, M. *J. Am. Chem. Soc.* **2010**, *132*, 9604. (e) Fukuoka, T.; Uchida, K.; Sung, Y. M.; Shin, J.-Y.; Ishida, S.; Lim, J. M.; Hiroto, S.; Furukawa, K.; Kim, D.; Iwamoto, T.; Shinokubo, H. *Angew. Chem. Int. Ed.* **2014**, *53*, 1506. (f) Nozawa, R.; Yamamoto, K.; Shin, J.-Y.; Hiroto, S.; Shinokubo, H. *Angew. Chem. Int. Ed.* **2015**, *54*, 8454. (g) Liu, B.; Li, X.; Stępień, M.; Chmielewski, P. J. *Chem. Eur. J.* **2015**, *21*, 7790. (h) Deng, Z.; Li, X.; Stępień, M.; Chmielewski, P. J. *Chem. Eur. J.* **2016**, *22*, 4231. (i) Yoshida, T.; Shinokubo, H. *Mater. Chem. Front.* **2017**, *1*, 1853. (j) Liu, S.-Y.; Fukuoka, T.; Fukui, N.; Shin, J.-Y.; Shinokubo, H. *Org. Lett.* **2020**, *22*, 4400.
6. (a) Hafner, K.; Süß, H. U. *Angew. Chem. Int. Ed. Engl.* **1973**, *12*, 575. (b) Chase, D. T.; Rose, B. D.; McClintock, S. P.; Zakharov, L. N.; Haley, M. M. *Angew. Chem. Int. Ed.* **2011**, *50*, 1127. (c) Shimizu, A.; Tobe, Y. *Angew. Chem. Int. Ed.* **2011**, *50*, 6906. (d) Iida, A.; Yamaguchi, S. *J. Am. Chem. Soc.* **2011**, *133*, 6952. (e) Wakamiya, A.; Mishima, K.; Ekawa, K.; Yamaguchi, S. *Chem. Commun.* **2008**, 579.
7. Shin, J.-Y.; Yamada, T.; Yoshikawa, H.; Awaga, K.; Shinokubo, H. *Angew. Chem. Int. Ed.* **2014**, *53*, 3096.

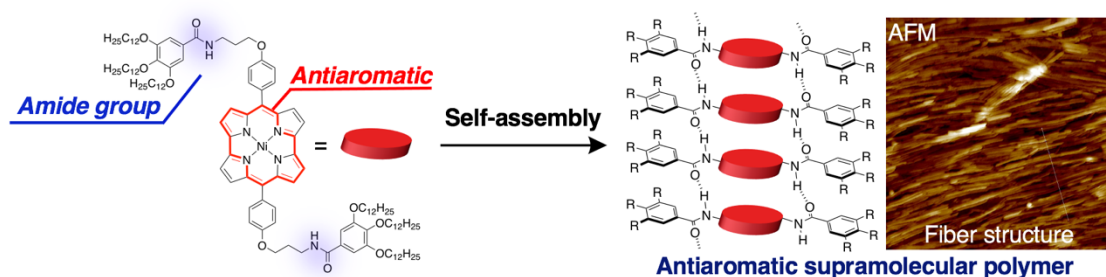
8. (a) Kawase, T.; Fujiwara, T.; Kitamura, C.; Konishi, A.; Hirao, Y.; Matsumoto, K.; Kurata, H.; Kubo, T.; Shinamura, S.; Mori, H.; Miyazaki, E.; Takimiya, K. *Angew. Chem. Int. Ed.* **2010**, *49*, 7728. (b) Chase, D. T.; Fix, A. G.; Kang, S. J.; Rose, B. D.; Weber, C. D.; Zhong, Y.; Zakharov, L. N.; Lonergan, M. C.; Nuckolls, C.; Haley, M. *M. J. Am. Chem. Soc.* **2012**, *134*, 10349. (c) Nishinaga, T.; Ohmae, T.; Aita, K.; Takase, M.; Iyoda, M.; Arai, T.; Kunugi, Y. *Chem. Commun.* **2013**, *49*, 5354. (d) Nakano, M.; Osaka, I.; Takimiya, K.; Koganezawa, T. *J. Mater. Chem. C.* **2014**, *2*, 64. (e) Marshall, J. L.; Uchida, K.; Frederickson, C. K.; Schütt, C.; Zeidell, A. M.; Goetz, K. P.; Finn, T. W.; Jarolimek, K.; Zakharov, L. N.; Risko, C.; Herges, R.; Jurchescu, O. D.; Haley, M. M. *Chem. Sci.* **2016**, *7*, 5547.
9. Bröring, M.; Köhler, S.; Kleeberg, C. *Norcorrole. Angew. Chem. Int. Ed.* **2008**, *47*, 5658.
10. Ito, T.; Hayashi, Y.; Shimizu, S.; Shin, J.; Kobayashi, N.; Shinokubo, H. *Angew. Chem. Int. Ed.* **2012**, *51*, 8542.
11. (a) Nozawa, R.; Tanaka, H.; Cha, W.-Y.; Hong, Y.; Hisaki, I.; Shimizu, S.; Shin, J.-Y.; Kowalczyk, T.; Irle, S.; Kim, D.; Shinokubo, H. *Nat. Commun.* **2016**, *7*, 13620. (b) Yoshida, T.; Sakamaki, D.; Seki, S.; Shinokubo, H. *Chem. Commun.* **2017**, *53*, 1112. (c) Liu, S.; Tanaka, H.; Nozawa, R.; Fukui, N.; Shinokubo, H. *Chem. Eur. J.* **2019**, *25*, 7618.
12. (a) Bühl, M.; van Wüllen, C. *Chem. Phys. Lett.* **1995**, *247*, 63. (b) Schleyer, P. von R.; Maerker, C.; Dransfeld, A.; Jiao, H.; van Eikema Hommes, N. J. R. *J. Am. Chem. Soc.* **1996**, *118*, 6317.
13. The mean planes are defined by the 22 core atoms consisting of *meso*-carbons and four pyrrole units.

Chapter 2

14. Krygowski, T. M.; Cyrański, M. K. *Chem. Rev.* **2001**, *101*, 1385.
15. Fujii, S.; Marqués-González, S.; Shin, J.-Y.; Shinokubo, H.; Masuda, T.; Nishino, T.; Arasu, N. P.; Vázquez, H.; Kiguchi, M. *Nat. Commun.* **2017**, *8*, 15984.
16. (a) Seki, S.; Saeki, A.; Sakurai, T.; Sakamaki, D. *Phys. Chem. Chem. Phys.* **2014**, *16*, 11093. (b) Kato, S.; Serizawa, Y.; Sakamaki, D.; Seki, S.; Miyake, Y.; Shinokubo, H. *Chem. Commun.* **2015**, *51*, 16944.

Chapter 3

A supramolecular polymer constituted of antiaromatic Ni(II) norcorroles



Contents

3-1. Introduction	48
3-2. Synthesis and characterization of monomers	50
3-3. Self-assembly behavior	56
3-4. Morphology of aggregates	61
3-5. π -Stacking mode.....	64
3-6. Charge-transport properties.....	69
3-7. Summary of Chapter 3	73
3-8. References	74

3-1. Introduction

Polymers, which consist of repeating structures linked by covalent bonds, have been successfully applied to a wide range of functional materials due to their high durability, light weight, and processability. On the other hand, the very same high durability can also result in unsustainable materials with high environmental impact.

In recent decades, chemists have been inspired by the dynamic interactions of biological systems such as DNA¹ and organelles,² which form large periodic structures to explore supramolecular polymerization. Supramolecular polymerization allows the reversible construction of large periodic structures by combining dynamic intermolecular interactions, i.e., hydrogen bonds,³ coordination bonds,⁴ or π - π stacking.^{5,6c}

As the function of a supramolecular polymer depends on the properties of its monomer units,⁶ an expansion of the diversity in monomers available for supramolecular polymerization should represent a desirable research target. One attractive class of monomers is π -conjugated molecules, because their delocalized π -electrons can enable higher-order functions such as charge transport,⁷ magnetism,⁸ and energy storage.⁹ However, the use of “aromatic” π -conjugated molecules has been regarded as indispensable in the design of electronic functional supramolecular polymer systems, which are often composed of polycyclic aromatic hydrocarbons, perylene bisimides, or porphyrins.¹⁰

In recent years, antiaromatic compounds have attracted considerable attention due to their unique properties,¹¹ which include high conductivity,¹² biradical character,¹³ and multi-redox behavior.¹⁴ In this context, the author became interested in supramolecular polymers that consist of antiaromatic molecules. However, supramolecular polymers based on antiaromatic monomer units have not been reported to date.¹⁵ The reason for

this is the inherent unstable nature of antiaromatic molecules. The common strategy for stabilizing antiaromatic molecules is the introduction of bulky peripheral substituents,¹⁶ which hampers effective intermolecular interactions between monomers in the aggregates. The author have recently discovered that Ni(II) *meso*-diphenylnorcorrole **3-1** (Figure 3-1) exhibits high stability toward air, water, and heat despite its lack of steric protection by bulky *meso*-substituents.^{17,18a} Furthermore, the author have reported that the Ni(II) norcorrole units adopt close π - π stacking with interplanar distances of 3.05–3.26 Å in norcorrole cyclophanes, leading to effective orbital interactions.¹⁸ If such an effective overlap of π -orbitals of norcorrole macrocycles could be achieved in a long-distance periodic manner, highly efficient charge transport within the molecular assembly could potentially be accomplished. Against this background, the author explored the supramolecular polymerization of an antiaromatic norcorrole Ni(II) complex via π -stacking.

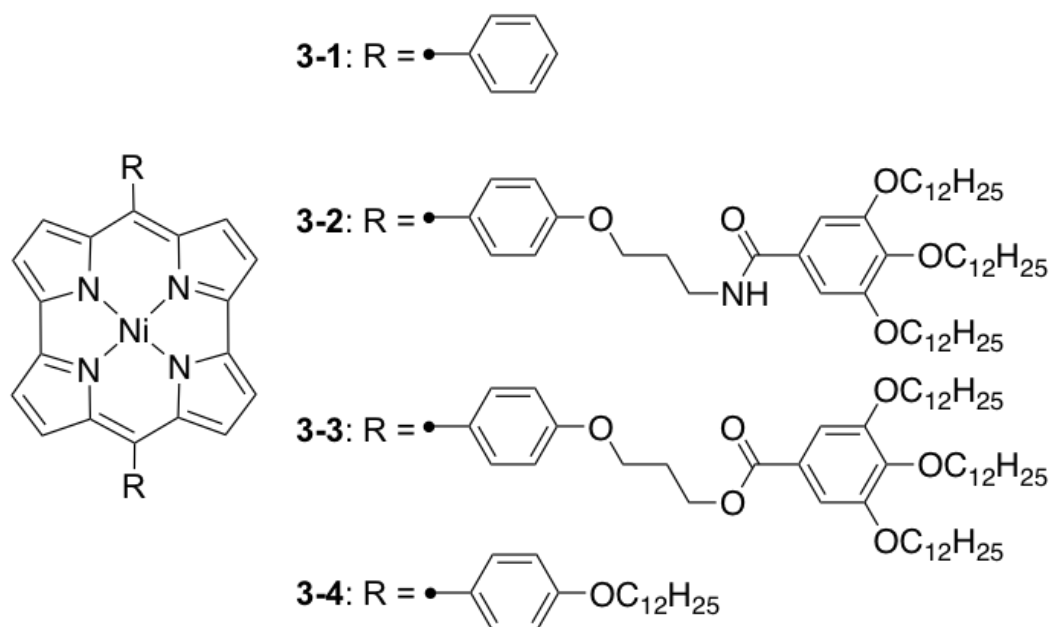
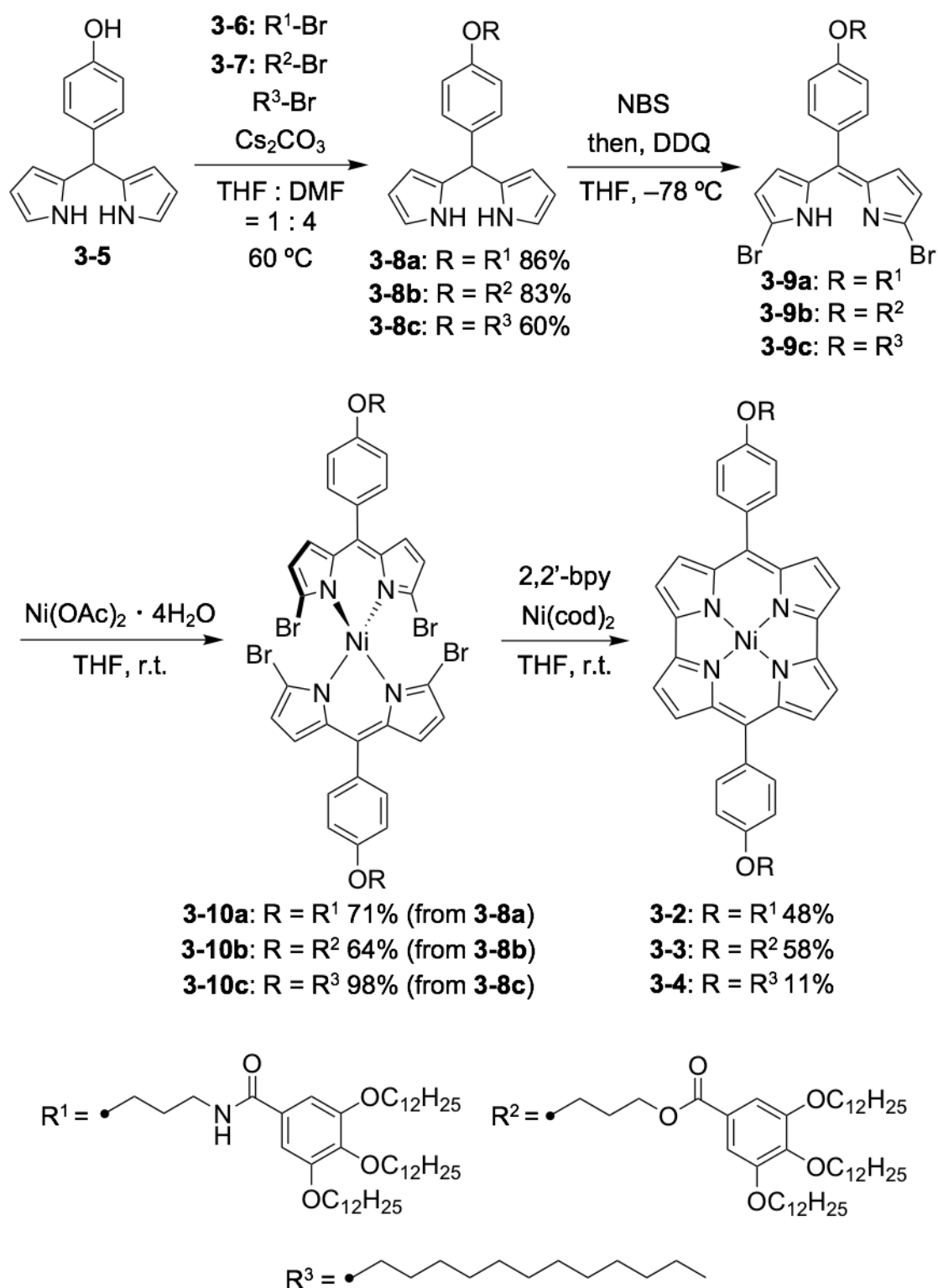


Figure 3-1. Structures of the *meso*-substituted norcorroles **3-1**–**3-4** used in this study.

3-2. Synthesis and characterization of monomers

Inspired by hitherto reported supramolecules that consist of aromatic π -components, the author designed norcorrole Ni(II) complex **3-2** with amide moieties as hydrogen-bonding sites and long alkyl chains. Norcorrole **3-2** is expected to self-assemble via π - π stacking, hydrogen-bonding of the amide groups, and via van der Waals interactions among long alkyl chains. Compound **3-3** and **3-4** was designed for control.

The synthetic route to **3-2**, **3-3** and **3-4** is illustrated in Scheme 3-1. Treatment of 5-(4-hydroxyphenyl)dipyrromethane **3-5** with long-chain alkyl bromides afforded **3-8a**, **3-8b** and **3-8c**. Bromination of **3-8a**, **3-8b** and **3-8c** with N-bromosuccinimide (NBS) followed by oxidation with 2,3-dichloro-5,6-dicyano-p-benzoquinone (DDQ) afforded dipyrromethenes **3-9a**, **3-9b** and **3-9c**. Then, the reaction mixtures were subjected to metalation with Ni(OAc)₂·4H₂O without purification. The reaction provided the corresponding dipyrin Ni(II) complexes **3-10a**, **3-10b**, and **3-10c** in three steps in 71%, 64% and 98% yield, respectively. Reductive coupling of **3-10a**, **3-10b**, and **3-10c** provided Ni(II) norcorroles **3-2**, **3-3**, and **3-4** in 48%, 58% and 11% yield, respectively. These norcorroles were characterized using NMR spectroscopy and high-resolution mass spectrometry. Fortunately, a single crystal of **3-4** was obtained by slow evaporation of a chloroform solution, enabling an unambiguous elucidation of its solid-state structure via X-ray diffraction analysis (Figure 3-2).

Scheme 3-1. Synthesis of norcorrole Ni(II) complexes **3-2**, **3-3**, and **3-4**.

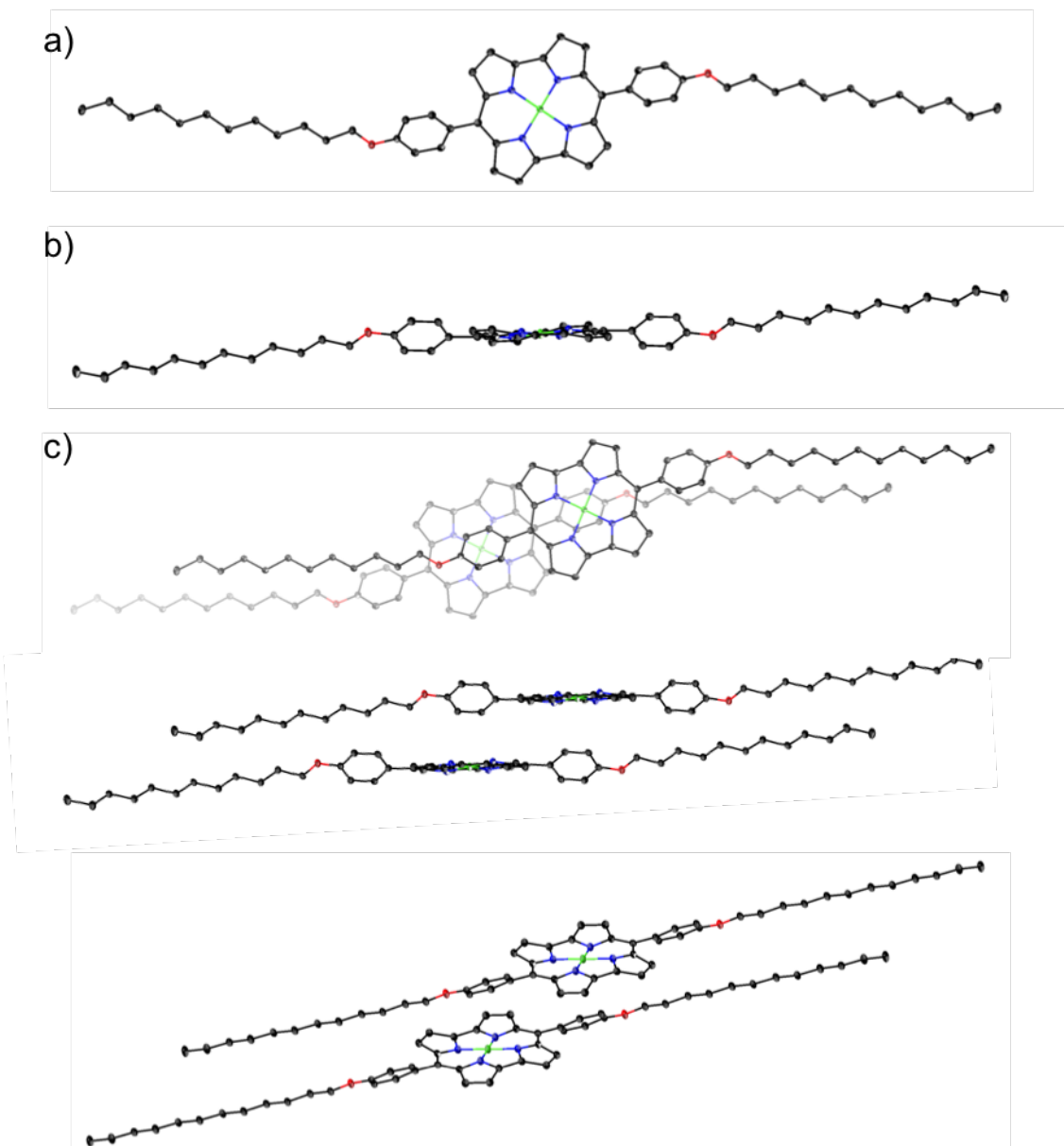
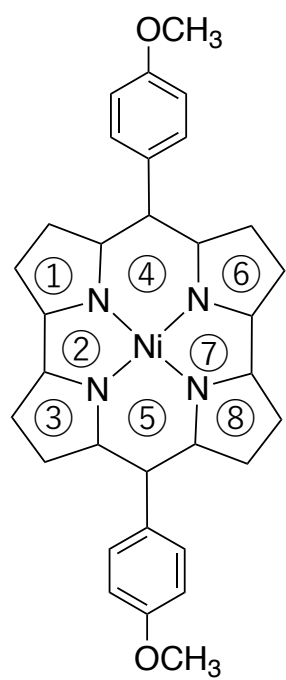


Figure 3-2. X-ray crystal structure of 3-4. (a) Top view, (b) side view, and (c) diagonal view. Thermal ellipsoids are shown at the 20% probability level. All hydrogen atoms are omitted for clarity.

Norcorrole Ni(II) complexes with *meso*-4-alkoxyphenyl groups have not yet been reported. Consequently, the electronic modulation of the 4-alkoxyphenyl groups on the antiaromaticity of **3-2**, **3-3**, and **3-4** was evaluated using ^1H NMR spectral analysis and DFT calculations.³² In the ^1H NMR spectra of **3-2**, **3-3**, and **3-4** in CDCl_3 , the signals of the pyrrole protons appeared in the region $\delta = 2.06\text{--}2.52$ ppm, which is considerably upfield-shifted compared to those of normal pyrroles (δ 6–7 ppm). These chemical shift values are almost identical to those of Ni(II) *meso*-diphenylnorcorrole **3-1**, which corroborates the presence of a distinct paratropic ring current effect. NICS(1) values calculated at the GIAO-BHLYP/6-31G(d)+SDD level ranged from 23.6 to 27.7 ppm except at the pyrrole subunits, which also support the presence of paratropicity of **3-2**, **3-3**, and **3-4** (Table 3-1).^{21,22}

Table 3-1. NICS values of norcorrol substituted para-methoxyphenyl groups.

	NICS(0) [ppm] X-ray structure	NICS(0) [ppm] Optimized structure	NICS(1) [ppm] Optimized structure
	①	1.23	0.88
	②	26.33	26.44
	③	1.24	0.90
	④	26.88	27.52
	⑤	27.01	27.52
	⑥	1.03	0.90
	⑦	26.38	26.44
	⑧	1.36	0.88

The electronic modulation was further investigated using UV/vis/NIR absorption spectroscopy. The UV/vis/NIR absorption spectra of **3-1–3-4** in CH₂Cl₂ are shown in Figure 3-3, and all exhibit broad and weak absorption bands tailing to 900 nm. This absorption feature is characteristic for Ni(II) norcorrole complexes. TD-DFT calculations at the B3LYP/6-31G(d)+SDD level of theory suggest that the weak absorption bands originate from the forbidden HOMO→LUMO and HOMO-1→LUMO transitions (Figure 3-4 and 3-5). These spectroscopic results and DFT calculations confirm the antiaromatic nature of the norcorrole cores of **3-2**, **3-3** and **3-4**. The absorption spectra of **3-2**, **3-3** and **3-4** are similar to each other but differ from that of **3-1** around 500 nm. This is due to the substituent effect of the 4-alkoxyphenyl groups, which was also supported by TD-DFT calculations.

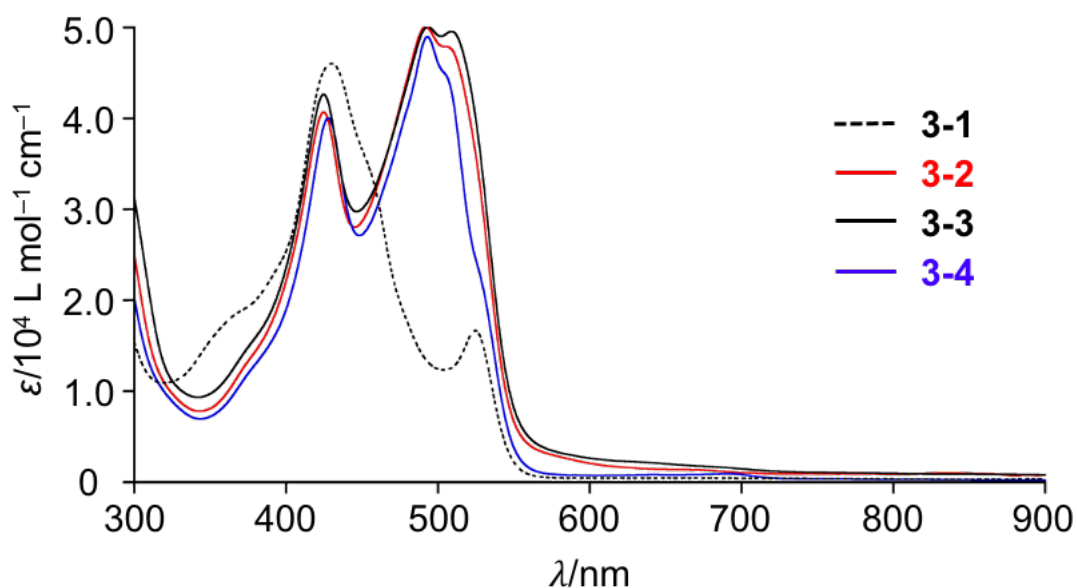


Figure 3-3. UV/Vis/NIR absorption spectra of **3-1** (blue), **3-2** (red), **3-3** (green), and **3-4** (black) in CH₂Cl₂; λ = wavelength.

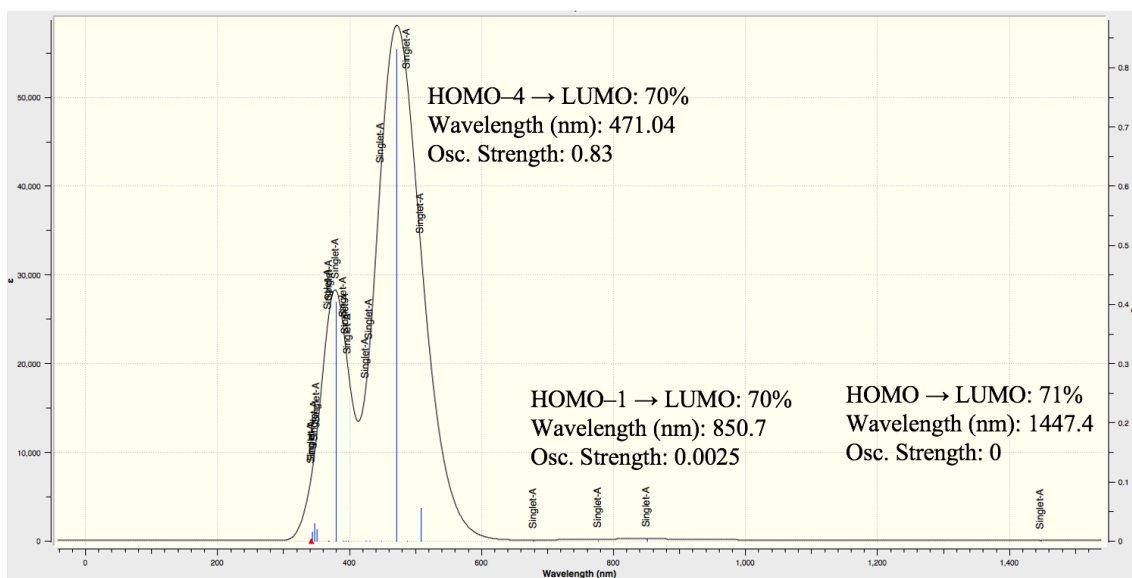


Figure 3-4. Simulated absorption spectrum of **3-4** calculated at the CAM-B3LYP/6-31G(d)+SDD level.

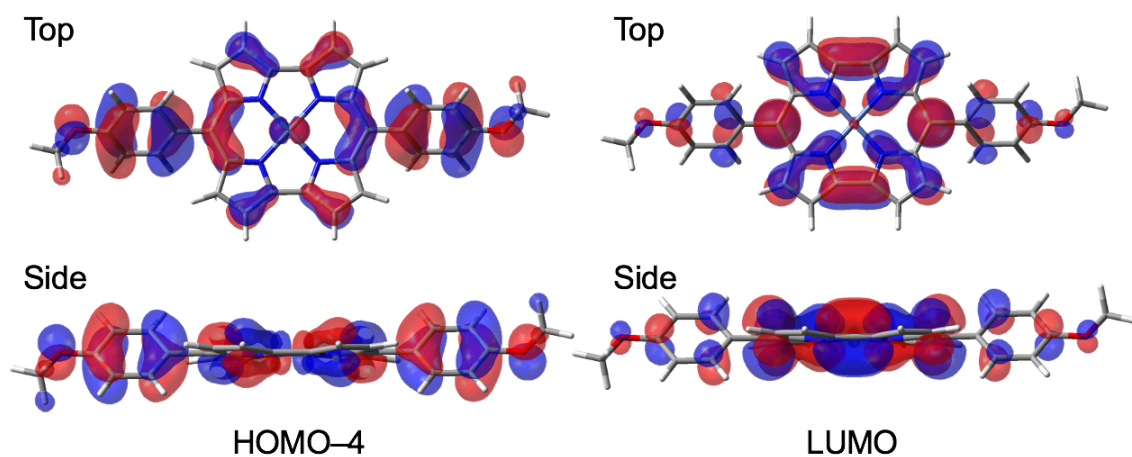


Figure 3-5. HOMO-4 and LUMO of **3-4** calculated at the CAM-B3LYP/6-31G(d)+SDD level.

3-3. Self-assembly behavior

The self-assembly behavior of Ni(II) *meso*-di(4-alkoxyphenyl)norcorrole **3-2** was investigated using temperature-dependent UV/vis/NIR absorption spectroscopy. Upon cooling a hot solution of **3-2** in cyclohexane/benzene (9/1) from 343 K to 283 K, distinct absorption changes were observed at 423 nm and 484 nm (Figure 3-6a). A slow cooling rate of 1 K min⁻¹ was applied to ensure that the self-assembly process occurred under thermodynamic control.¹⁹

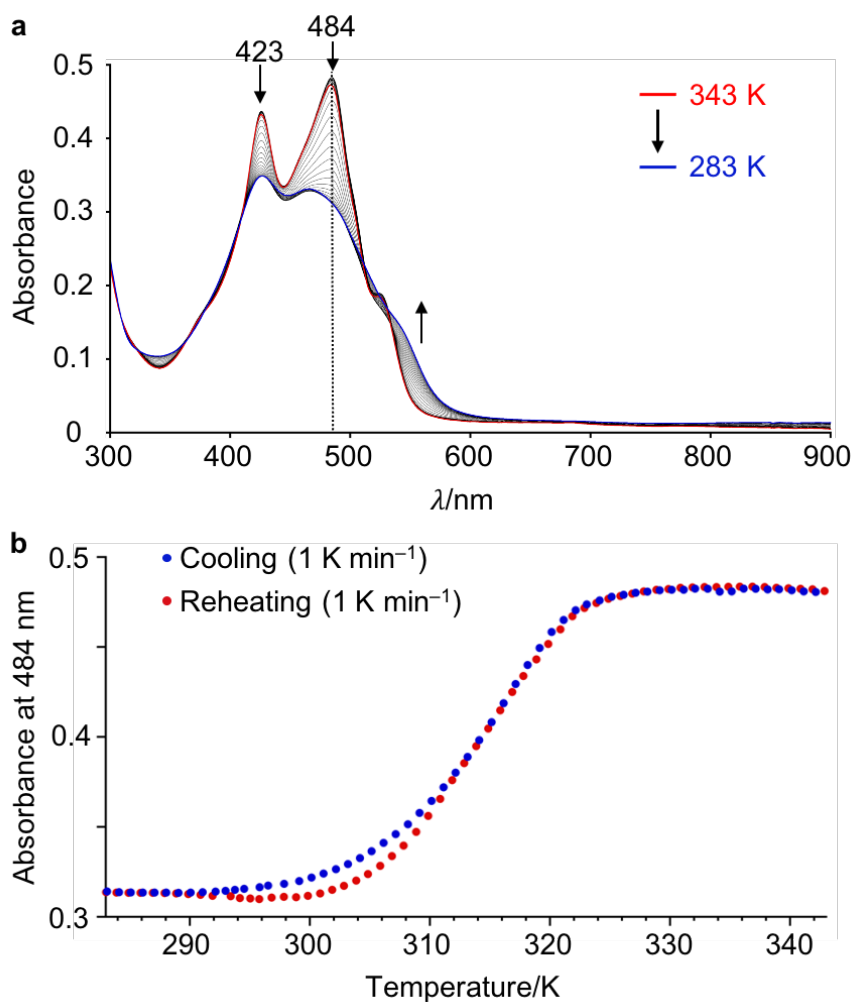


Figure 3-6. (a) UV/vis/NIR absorption changes of **3-2** observed during the cooling process in cyclohexane/benzene (9/1) ($[\mathbf{3-2}] = 10 \mu\text{M}$). (b) Changes in the absorption at 484 nm as a function of temperature during the cooling and reheating processes.

In fact, the heating and cooling rates were varied from 0.5 to 2.0 K min⁻¹, but no hysteresis curves were observed (Figure 3-7). The self-assembly and disassembly processes of **3-2** were monitored via the changes in the absorption band intensity at 484 nm as a function of temperature (Figure 3-6b). The cooling and re-heating processes were essentially reversible. This result indicates that **3-2** is stable toward heating in solution.

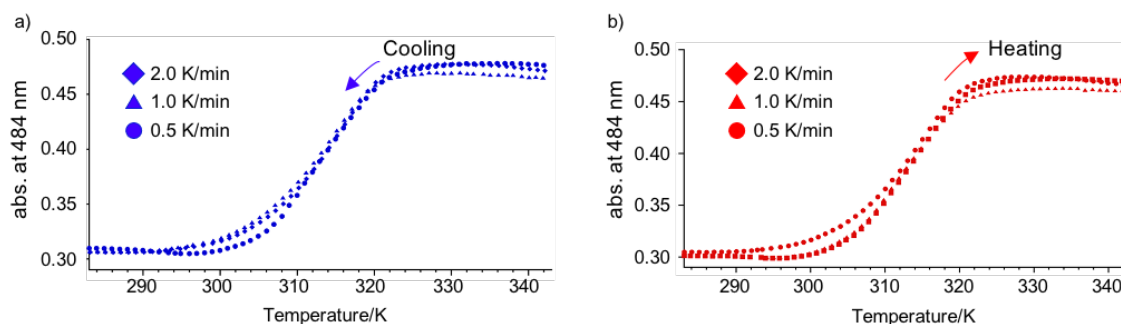


Figure 3-7. Effect of cooling and heating rates on the aggregation (a) (blue) and dissociation (b) (red) processes of **3-2** (total concentration: $C_T = 10 \mu\text{M}$) in cyclohexane/benzene (9:1, v/v).

Because the observed curves seem to be sigmoidal, the author first attempted to analyze the association behavior based on the isodesmic model¹⁹ but could not reproduce the experimental curves. Next, the aggregation behavior was analyzed based on the nucleation–elongation model^{23,24}, which reproduced the curve well. From the analysis of the aggregation parameters affording an enthalpy value of -94 kJ mol^{-1} ($[\mathbf{3-2}] = 10 \mu\text{M}$) (Figure 3-8 and Table 3-1). Lowering the initial concentration of **3-2** resulted in a decrease in the elongation temperature, T_e , but the enthalpy values were almost independent of the concentrations. Plotting the natural logarithm of the concentration as a function of the reciprocal of T_e (van't Hoff plot) yielded an enthalpy and entropy of -96 kJ mol^{-1} and $-203 \text{ J mol}^{-1} \text{ K}^{-1}$, respectively (Figure 3-9), which is in good agreement with the values derived from modeling the melting curves. In addition, the association behavior of the

corresponding ester derivative **3-3** was investigated using temperature-dependent UV/vis/NIR absorption spectroscopy under the same conditions as those for **3-2**. Ester **3-3** exhibited no association behavior, thus confirming the importance of the amide groups to undergo self-assembly in the case of **3-2**.

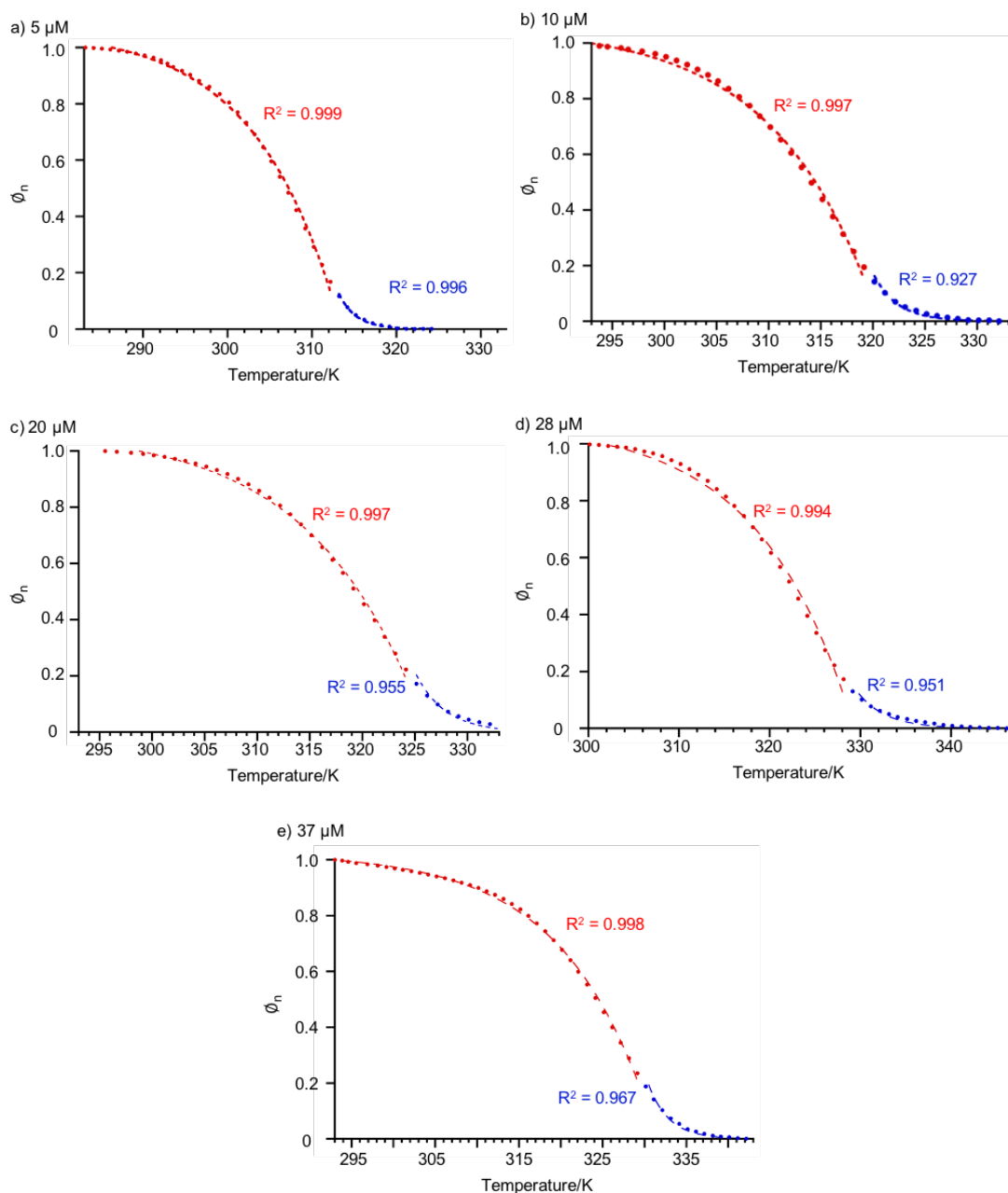


Figure 3-8. Fit of the nucleation-elongation model for the solution of **3-2** in cyclohexane/benzene (9:1, v/v) in the UV/vis/NIR absorption data. The red line corresponds to the fit for the elongation process based on Eq. 1.^{24b} The blue line corresponds to the fit for the

nucleation process based on Eq. 2.^{24b} Concentrations: (a) 5 μM , (b) 10 μM , (c) 20 μM , (d) 27 μM , and (e) 37 μM .

$$\Phi_n = \Phi_{\text{SAT}} \left(1 - \exp \left[\frac{-h_e}{RT_e^2} (T - T_e) \right] \right) \quad (\text{Eq. 1})$$

where h_e is the molecular enthalpy release due to non-covalent interactions during elongation, T is the absolute temperature, T_e is the elongation temperature and R is the gas constant. Φ_{SAT} is introduced as a parameter to ensure that Φ_n/Φ_{SAT} does not exceed unity.^{24b}

$$\Phi_n = K_a^{1/3} \exp \left[\left(\frac{2}{3} K_a^{1/3} - 1 \right) \frac{h_e}{RT_e^2} (T - T_e) \right] \quad (\text{Eq. 2})$$

where K_a is equilibrium constants for the nucleation process.

Table 3-1. Thermodynamic parameters for the self-assembly of **3-2** in cyclohexane/benzene (9:1, v/v), determined by modeling the temperature-dependent spectroscopy. Those parameters were determined according to Eq. 1, Eq. 2, and Eq. 3.^{24b}

Concentration (μM)	Φ_{SAT}	h_e (kJ mol^{-1})	T_e (K)	K_a	$\langle N_n(T_e) \rangle$
5	1.069	-82.5	313.5	1.2×10^{-3}	9
10	1.050	-94.0	320.3	2.2×10^{-3}	8
20	1.077	-85.2	326.2	2.8×10^{-3}	7
28	1.074	-87.2	329.4	4.3×10^{-3}	6
37	1.025	-87.3	331.5	2.1×10^{-3}	8

$$\langle N_n(T_e) \rangle = \frac{1}{K_a^{1/3}} \quad (\text{Eq. 3})$$

Where $\langle N_n(T_e) \rangle$ is the number-averaged degree of polymerization averaged over all active species.

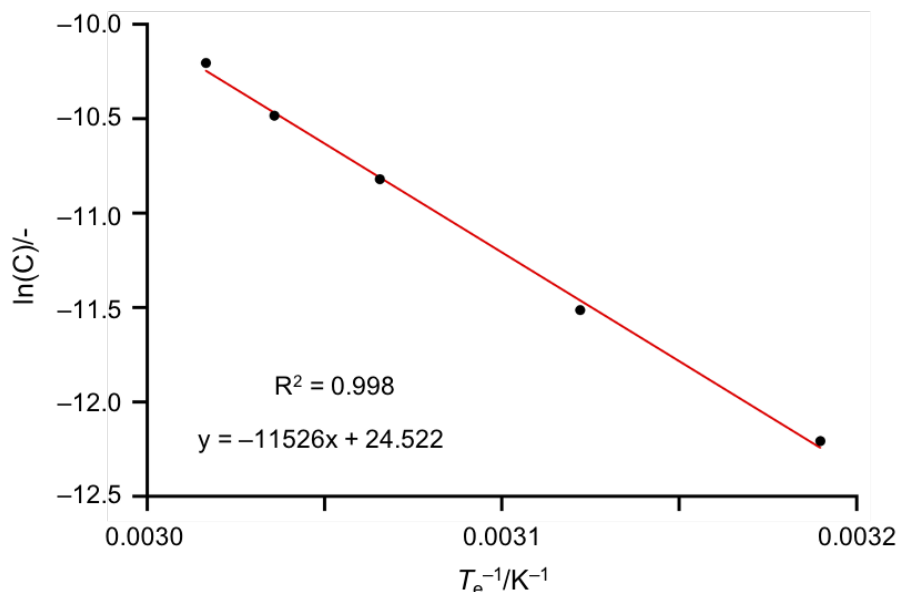


Figure 3-9. Logarithm of concentration versus reciprocal temperature for **3-2** in cyclohexane/benzene (9:1, v/v) for five concentrations from 37 μM to 10 μM . The enthalpy change of elongation process is calculated by multiplying the slope by gas constant: $\Delta H = -96 \text{ kJ mol}^{-1}$. The entropy change of the elongation process is calculated by multiplying the intercept by the gas constant: $\Delta S = -203 \text{ J mol}^{-1} \text{ K}^{-1}$. Fit of the Van't Hoff plot based on Eq. 4.¹⁹

$$\ln K_e = -\frac{\Delta G}{RT} = -\frac{\Delta H}{RT} + \frac{\Delta S}{R} \quad (\text{Eq. 4})$$

Where K_e is equilibrium constants for the elongation process. Here, the author used the equation Eq. 5¹⁹ for the relationship between elongation equilibrium constant K_e and C_T .

$$[C_T] = \frac{1}{K_e} \quad (\text{Eq. 5})$$

Aggregation constants for self-assembled **3-2** in cyclohexane/benzene (9/1, v/v) at different temperatures. The free energy, ΔG , and K_e at each T_e was determined using the enthalpy and entropy obtained from the Van't Hoff plot (Figure 3-9).

3-4. Morphology of aggregates

The morphology of the self-assembled Ni(II) *meso*-di(4-alkoxyphenyl)porphyrin **3-2** formed after the cooling process was investigated. Transmission electron microscopy (TEM) observations of self-assembled **3-2** revealed the formation of bundled fibers (Figure 3-11). Atomic force microscopy (AFM) afforded topological and phase images of films spin-coated from cyclohexane/benzene (9/1), elucidating the presence of many bundled fibers (Figure 3-12a). The height profile along the white line in Figure 3-12a is shown in Figure 3-12b. Figure 3-13 depicts the model structure of **3-2** obtained from DFT calculations at the B3LYP/6-31G(d)+SDD level of theory. The width (10 nm) and height (4 nm) of the peaks shown in Figure 3-12b are in good agreement with the model diameter (7.1 nm) and the short axis length (3.2 nm). These measurements indicate that **3-2** forms one-dimensional supramolecular polymers along the π -stacking axis.

The author then conducted Fourier-transform infrared (FT-IR) spectroscopy measurements to evaluate the presence of hydrogen-bonding interactions. FT-IR measurements showed that the N–H stretching band of self-assembled **3-2** (3270 cm^{-1}) is shifted to lower wavenumbers compared to that observed for the monomeric state in chloroform (3451 cm^{-1}), indicating the existence of hydrogen-bonding networks in the assembly (Figure 3-14). This shifted value is in good agreement with the reported value (3285 cm^{-1}) for H-aggregated porphyrins.²⁰

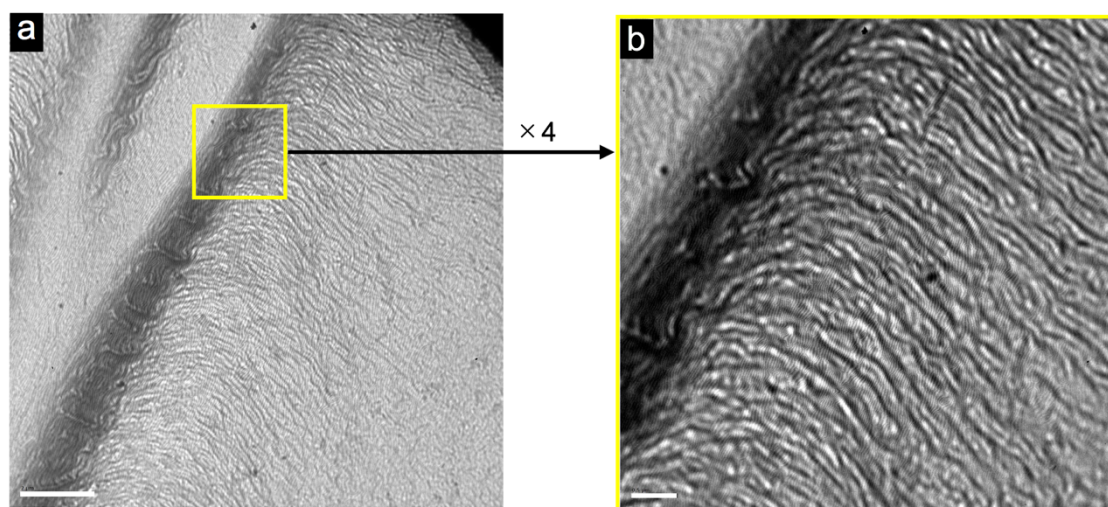


Figure 3-11. TEM image of self-assembled **3-2**. The TEM grid was dipped in a cyclohexane/benzene (9/1) solution of **3-2** ($10 \mu\text{M}$) after cooling and dried at room temperature under reduced pressure. The bar is (a) $2 \mu\text{m}$ (b) $0.5 \mu\text{m}$.

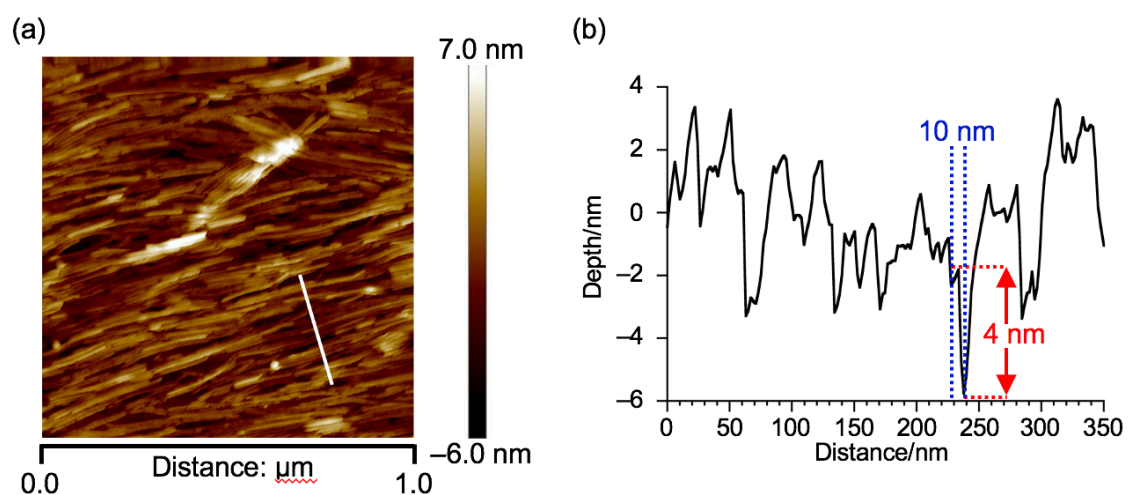


Figure 3-12. (a) AFM topographical image of a film spin-coated from a diluted solution of **3-2** in cyclohexane/benzene (9/1) ($[\mathbf{3-2}] = 10 \mu\text{M}$) onto silicon. (b) Height profile of the fibers measured along the white line in the AFM image

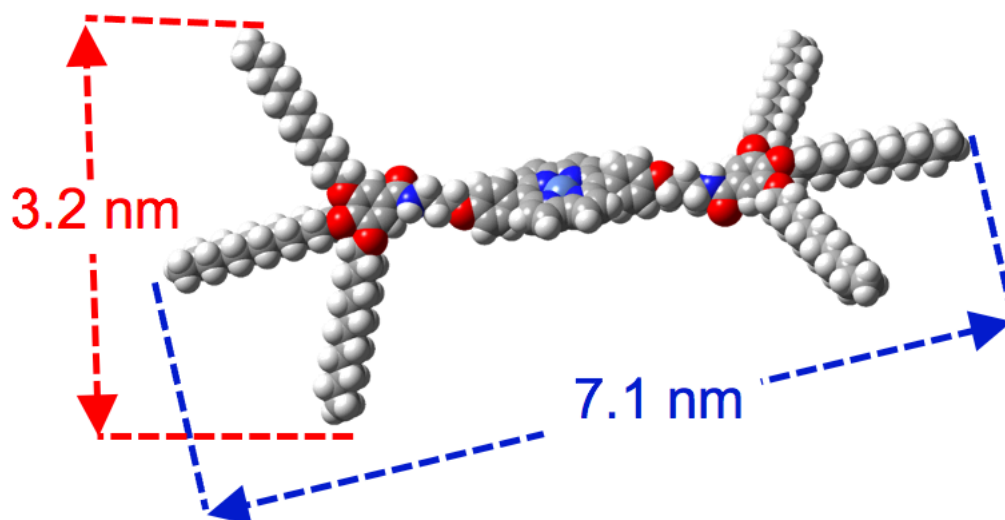


Figure 3-13. Simulated structure of **3-2**; atom color code: Purple, Ni; grey, C; red, O; blue, N; white, H.

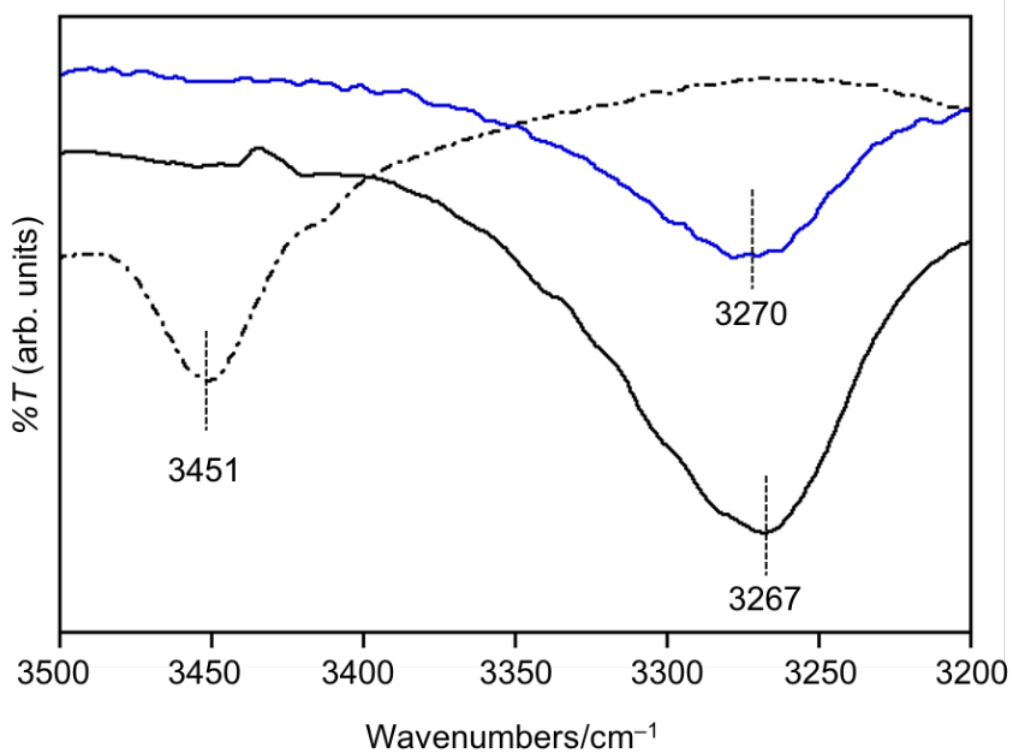


Figure 3-14. FT-IR spectra of NH stretching vibration of **3-2** in CHCl₃ (black dashed line), a solid sample prepared by freeze-drying of a cyclohexane/benzene (13:7, v/v) solution of **3-2** (blue line), and self-assembled **3-2** in cyclohexane/benzene (13:7, v/v) (black solid line).

3-5. π -Stacking mode

Previous studies on stacked Ni(II) norcorrole dimers elucidated that the effective orbital interactions between face-to-face-stacked norcorroles result in a distinct absorption band in the range of 700–1000 nm.¹⁸ In contrast, self-assembled **3-2** exhibited no characteristic absorption band in the NIR region, implying that norcorrole **3-2** does not form a face-to-face stacking arrangement.

The author then estimated the stacking orientation in self-assembled **3-2** using theoretical calculations. The 3,4,5-trialkoxyphenyl moieties were replaced with hydrogen atoms to reduce the computational costs. Two stable conformations, A and B, with slipped and face-to-face stacking structures, respectively, were obtained from the DFT calculations at the B97D3/6-31G(d)+SDD level of theory (Figures 3-15a, 3-15b). TD-DFT calculations at the CAM-B3LYP/6-31G(d)+SDD level were performed to simulate the absorption spectra of A and B. In A, the slipped π - π stacking should exhibit a weak forbidden transition in the range of 500–900 nm (oscillator strengths $f < 0.0085$) (Figures 3-16). This absorption feature is in good agreement with the experimental absorption spectrum of assembled **3-2**. On the other hand, the face-to-face π - π stacking in B should exhibit a distinct absorption band around 660 nm, for which the predominant contribution was assigned to the HOMO→LUMO+1 transition ($f = 0.2508$) (Figures 3-17). However, this situation does not match the experimental spectrum.

To obtain further insights into the self-assembled structure of **3-2**, variable-temperature ¹H NMR (VT-¹H NMR) measurements were conducted (Figure 3-18). Upon cooling of a hot solution of **3-2** in cyclohexane-*d*₁₂/benzene-*d*₆ (13/7) from 343 to 323 K, the pyrrole proton signals shifted from 2.6 ppm to 4.5 ppm. This indicates that the π -systems of **3-2** are close to each other in the aggregates. The ¹H NMR chemical shifts of

the pyrrole protons in A and B were also simulated using DFT calculations at the B3LYP/6-31G(d)+SDD level of theory (Figure 3-19). In the face-to-face stacking structure B, the pyrrole protons appeared in the aromatic region ($\delta = 6.7\text{--}7.7$ ppm), while the chemical-shift changes were smaller in the slipped stacking structure A ($\delta = 4.5\text{--}5.6$ ppm). These results also suggest that the Ni(II) norcorrole unit in assembled **3-2** is likely to adopt the slipped stacking mode.

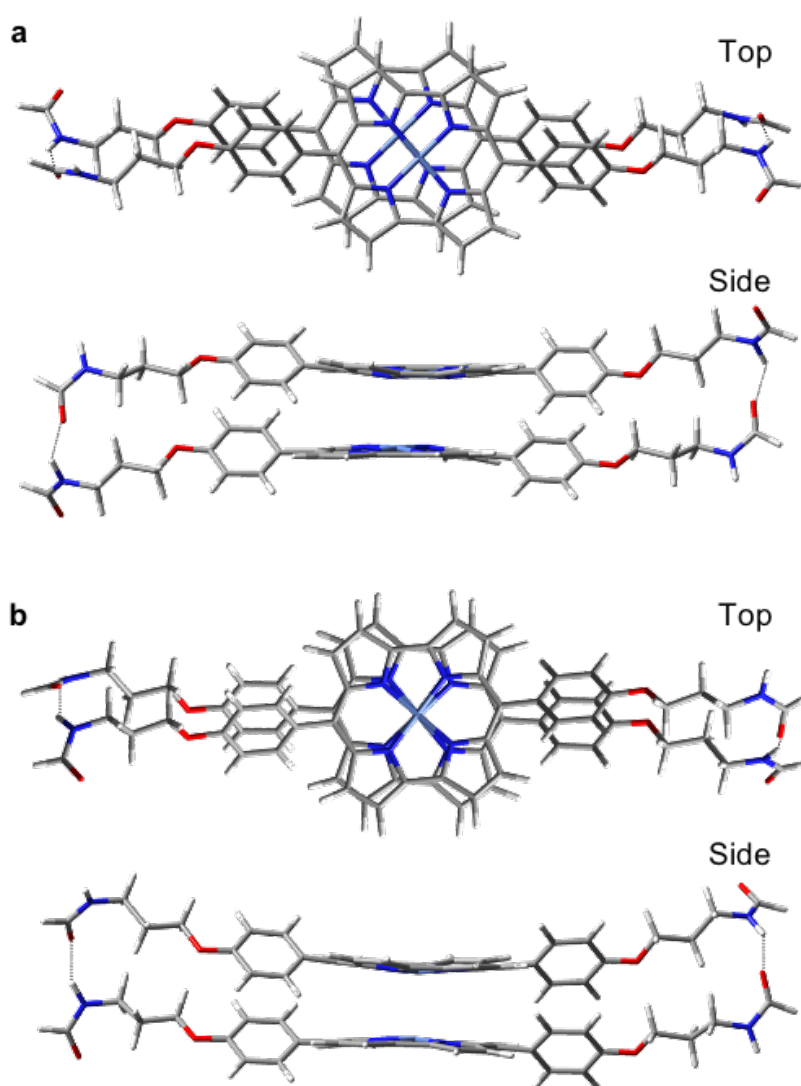


Figure 3-15. (a) Slipped stacking structure A and (b) face-to-face stacking structure B calculated at the B3LYP/6-31G(d)+SDD level of theory; for the calculations, the 3,4,5-trialkoxyphenyl moieties were replaced with hydrogen atoms.

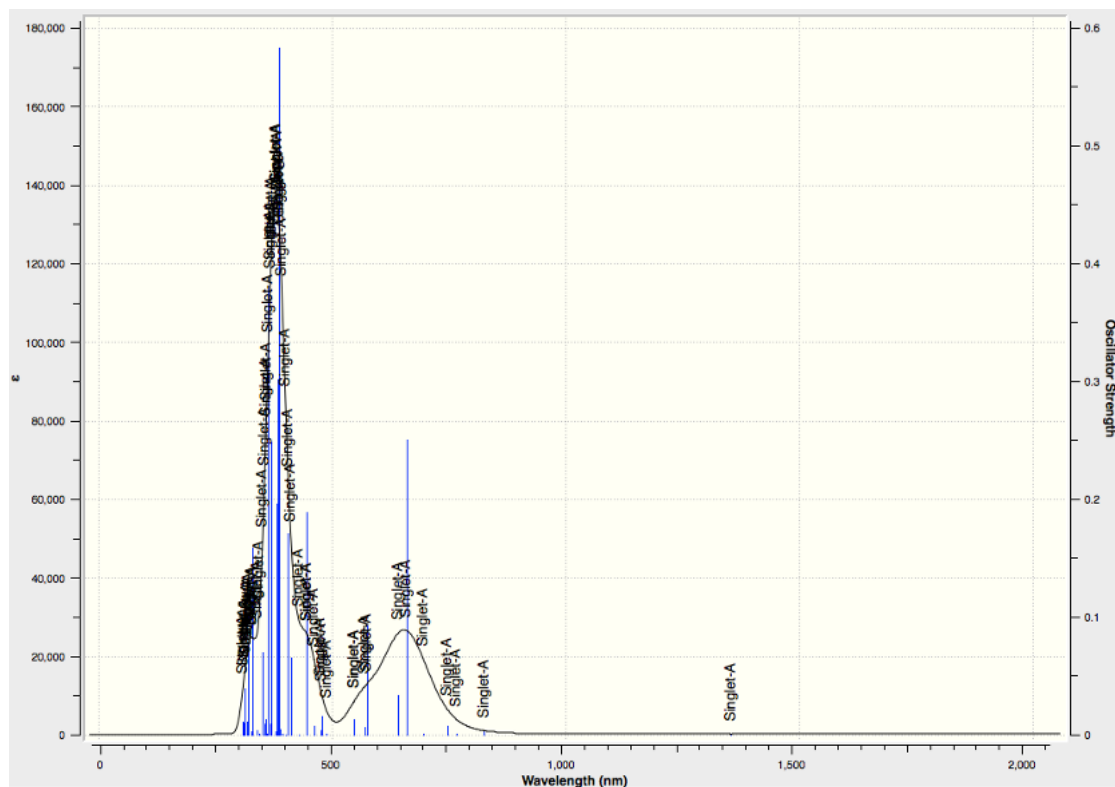


Figure 3-16. Simulated absorption spectrum of face-to-face π - π stacking dimer **3-2** calculated at the CAM-B3LYP/6-31G(d)+SDD level.

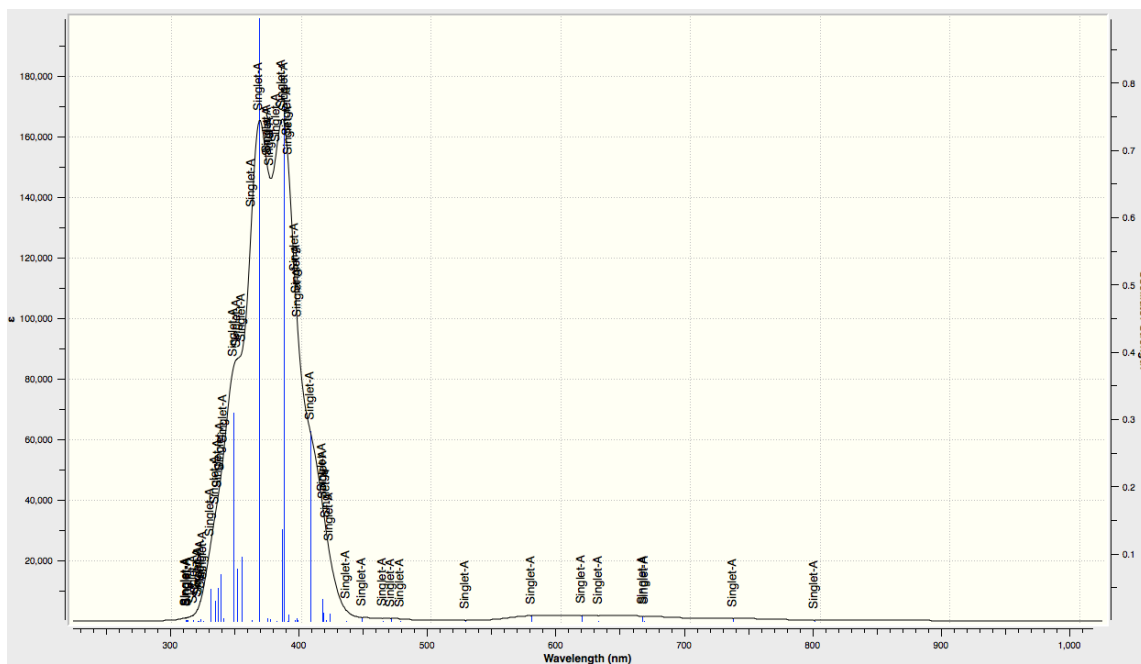


Figure 3-17. Simulated absorption spectrum of slipped π - π stacking dimer **3-2** calculated at the CAM-B3LYP/6-31G(d)+SDD level.

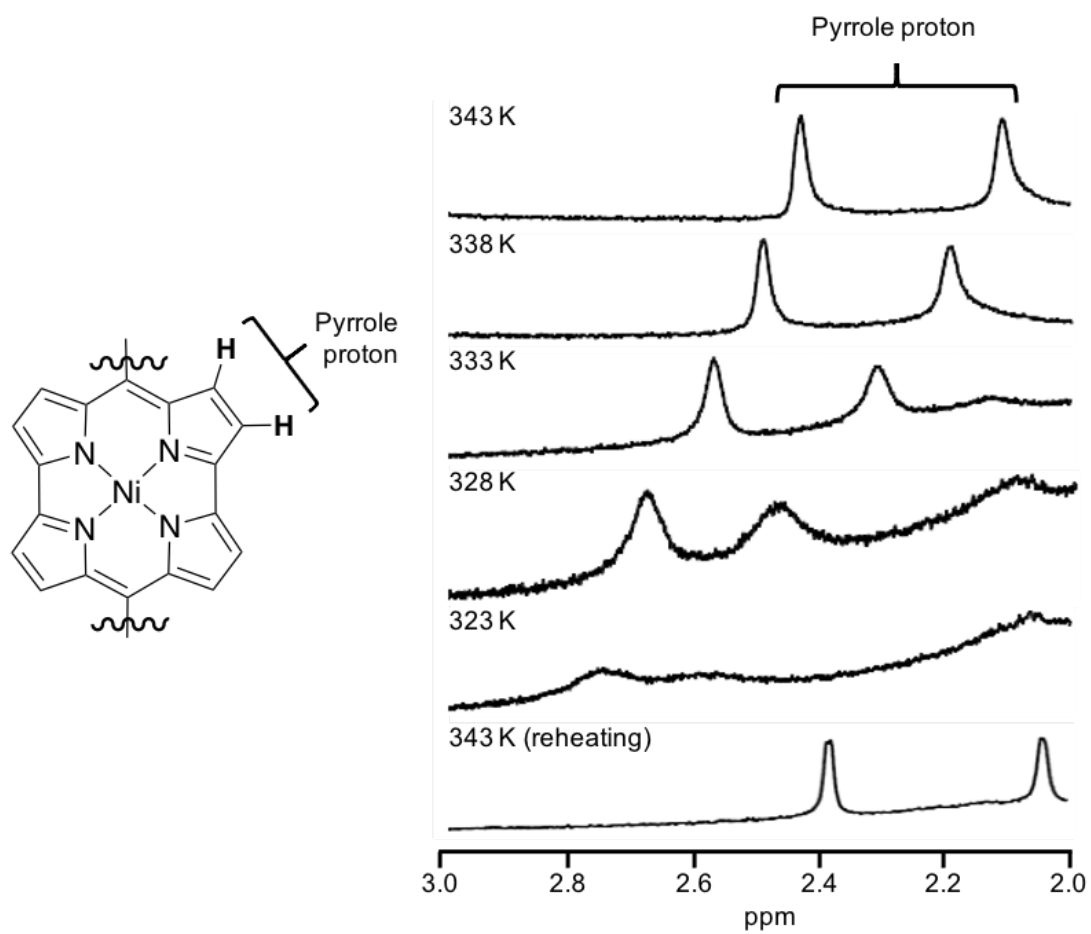


Figure 3-18. Temperature-dependent ^1H NMR spectra of **3-2** in cyclohexane- d_{12} /benzene- d_6 (13/7) from 343 to 323 K.

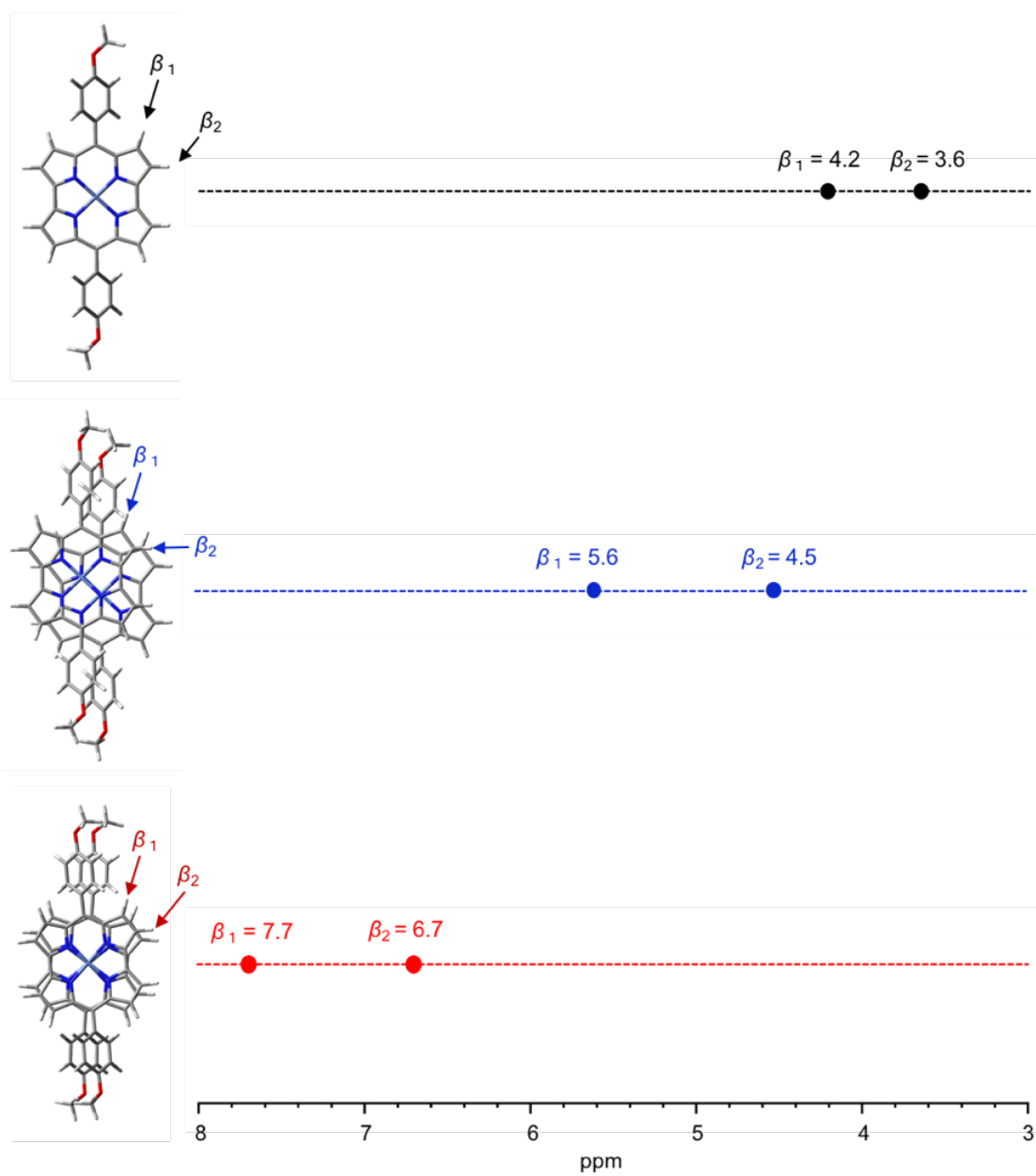


Figure 3-19. Simulated ^1H NMR chemical shift values of pyrrole protons of monomer, slipped π - π stacking dimer, and face-to-face π - π stacking of dimer **3-2** calculated at the B3LYP/6-31G(d)+SDD level.

3-6. Charge-transport properties

Antiaromatic molecules in close proximity should furnish electronically conductive pathways due to their stabilized LUMO and destabilized HOMO levels.²⁵ Previously, the author have reported that the one-dimensional columnar alignment of Ni(II) *meso*-dimethylnorcorrole in a slipped parallel manner provides stable electron-conducting pathways in chapter 2.¹⁷ Thus, the one-dimensional stacking assembly of **3-2** is expected to exhibit charge-transport properties.

The electronic conduction along an isolated chain configuration of **3-2** in solution was examined using flash-photolysis time-resolved microwave conductivity (FP-TRMC) measurements in cyclohexane/benzene (9/1) with chloranil as a mediator for the photo-induced electron-transfer reactions.²⁶ Electrodeless photocarrier injection was performed upon excitation at 355 nm. Upon heating the solution of **3-2** (70 μM) from 293 to 340 K, the photoconductivity signals gradually decreased and then disappeared abruptly at 340 K (Figure 3-20). This result is due to the dissociation of the supramolecular polymer at 340 K, which is consistent with the results observed during the heating process of self-assembled **3-2** in the UV/vis/NIR absorption measurements. A maximum $\varphi\Sigma\mu_{\text{max}}$ value of $6 \times 10^{-5} \text{ cm}^2 \text{ V}^{-1} \text{ s}^{-1}$ (φ : photo-generation efficiency of the charge carriers; $\Sigma\mu$: sum of the isotropic electron and hole mobility) was recorded for self-assembled **3-2** in solution. The quantum efficiency of the charge-carrier generation (φ) was determined to be 4×10^{-2} for **3-2** using transient absorption spectroscopy of chloranil radical anions: counter charges as an indicator. At 298 K, the sum of the isotropic electron and hole mobility is $\Sigma\mu = 1 \times 10^{-3} \text{ cm}^2 \text{ V}^{-1} \text{ s}^{-1}$ for **3-2**.

The author also evaluated the charge transport properties of the corresponding aromatic supramolecular polymer consisting of amide-functionalized Zn(II) porphyrin **3-**

11 reported by Takeuchi, Sugiyasu, and co-workers (Figure 3-21a).^{20b} The author selected **3-11** rather than the corresponding Ni(II) porphyrin as a reference molecule for Ni(II) norcorrole **3-2** because the Ni(II) porphyrin is not suitable for comparison due to its non-planar structure.²⁷ To ensure consistency with the measurement conditions used for **3-2**, the aggregation behavior and structure of **3-11** in cyclohexane/benzene (9/1) were confirmed using UV/vis/NIR absorption spectroscopy, TEM, AFM, and FT-IR measurements. Formation of bundled fibers were observed as is the case of **3-2**. In addition, the elongation enthalpy (-116 kJ mol^{-1})²⁸ and NH stretching band (3267 cm^{-1}) of self-assembled **3-11** are comparable to those of self-assembled **3-2**. These results imply that the stacking mode of self-assembled **3-2** is similar to that of self-assembled **3-11**. The electronic photoconduction of self-assembled **3-11** was examined using the FP-TRMC technique (Figure 3-21b). At 297 K, the $\Sigma\mu$ value for self-assembled **3-11** ($3 \times 10^{-4} \text{ cm}^2 \text{ V}^{-1} \text{ s}^{-1}$) was one quarter of that of self-assembled **3-2**. In addition, the electronic conduction of **3-11** in solid²⁹ was also examined using flash-photolysis time-resolved microwave conductivity (FP-TRMC) measurements revealed that **3-2** has a more stable charge carrier transport transportability than **3-11** (Figure 3-22).

Finally, photoconductivity measurements were performed for solid samples of self-assembled **3-2**, **3-3**³⁰ and Ni(II) *meso*-di(4-dodecyloxyphenyl)norcorrole **3-4** (Figure 3-23).³¹ The TRMC signals were very weak for **3-3** and **3-4**. In the crystal of **3-4**, the distance between the norcorrole π -systems is so long that the effective charge-transport pathway is not formed. In contrast, the maximum $\phi\Sigma\mu_{\text{max}}$ of self-assembled **3-2** ($1 \times 10^{-4} \text{ cm}^2 \text{ V}^{-1} \text{ s}^{-1}$) is comparable to that of *meso*-dimethylnorcorrole Ni(II) ($7 \times 10^{-5} \text{ cm}^2 \text{ V}^{-1} \text{ s}^{-1}$).¹⁷ These results demonstrate that the charge transport property is achieved due to close proximity of the norcorrole π -systems. Furthermore, the alignment of the π -stacking

assembly via hydrogen bonding is important for the formation of conductive paths along the stacking axis.

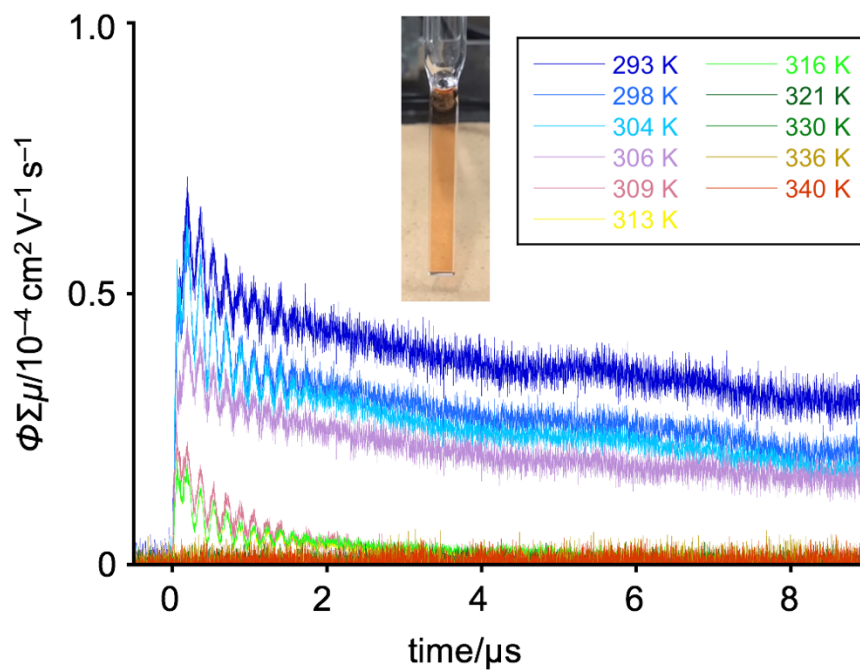


Figure 3-20. Photoconductivity transients of self-assembled **3-2** in cyclohexane/benzene (9/1) with 10 equiv of chloranil at 293–340 K ($[3-2] = 70 \mu\text{M}$); inset: Solution sample in a cell with a 3 mm light path.

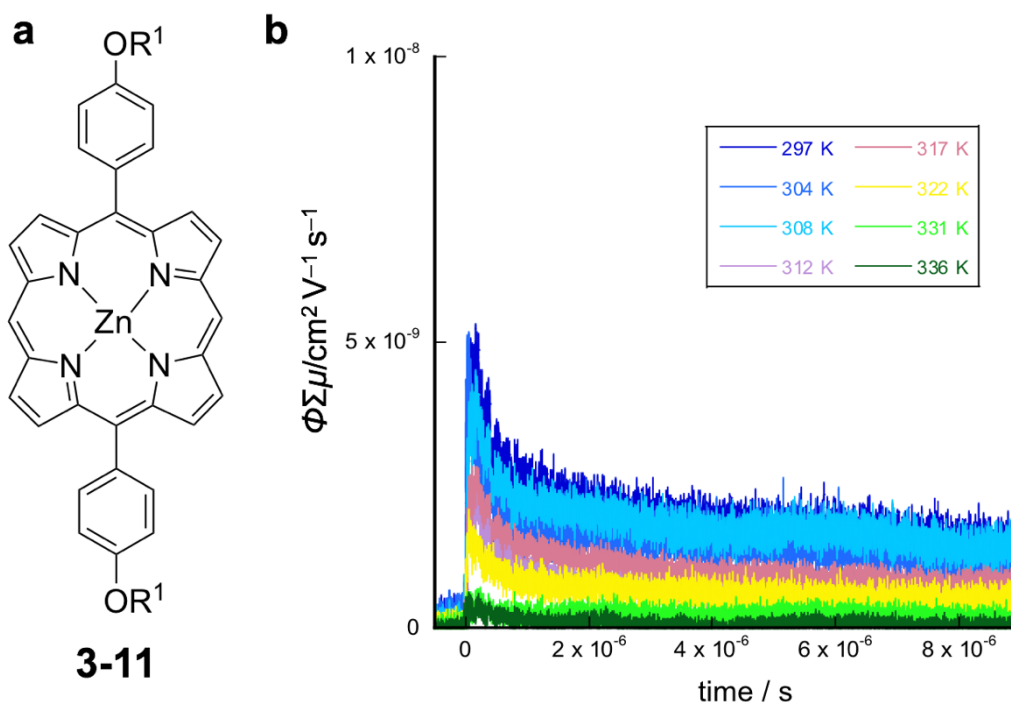


Figure 3-21. (a) Structure of **3-11** (b) Photoconductivity transients of self-assembled **3-11** in cyclohexane/benzene (9/1) with 10 equiv of chloranil at 297–336 K ($[\mathbf{3-11}] = 70 \mu\text{M}$). The solution and solid were excited by Nd:YAG laser pulses with ~ 5 ns duration at 355 nm (third harmonics), 1.4×10^{16} photons cm^{-2} .

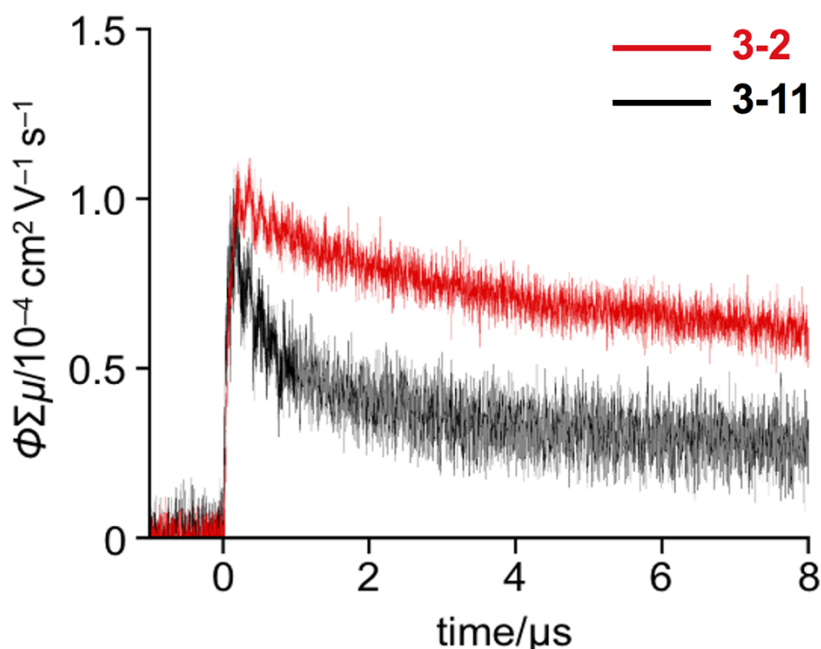


Figure 3-22. Photoconductivity transients of self-assembled **3-2** (red) and **3-11** (black) in thin films. The solid was excited using Nd:YAG laser pulses (duration: ~ 5 ns; 355 nm (third harmonics); 1.4×10^{16} photons cm^{-2}).

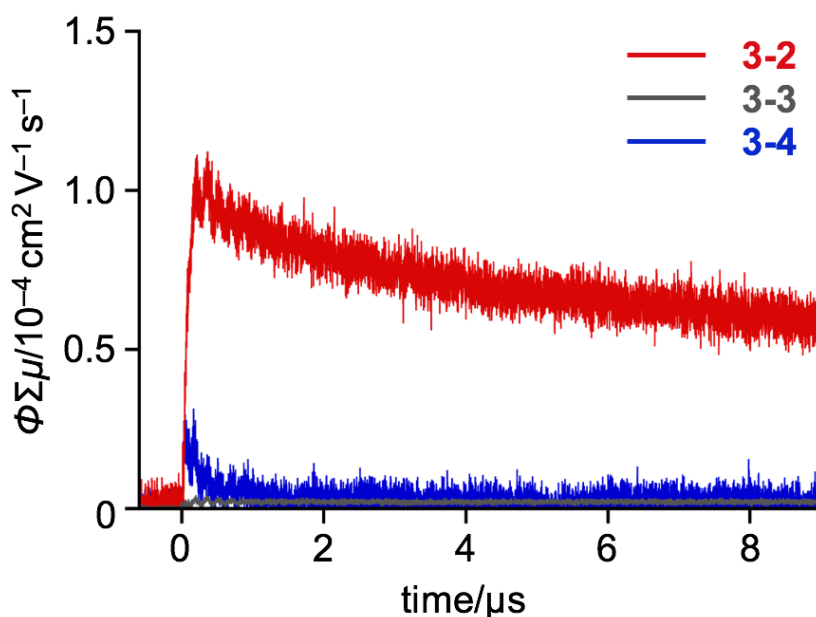


Figure 3-23. Photoconductivity transients of self-assembled **3-2** (red), **3-3** (yellow green) and **3-4** (blue) in thin films. The solution and solid were excited using Nd:YAG laser pulses (duration: ~ 5 ns; 355 nm (third harmonics); 1.4×10^{16} photons cm^{-2}).

3-7. Summary of Chapter 3

The author synthesized amide-functionalized norcorrole Ni(II) complex **3-2**. Spectroscopic and microscopic measurements revealed that self-assembled **3-2** forms a one-dimensional array via hydrogen-bonding interactions and π - π stacking. The stacking conformation of the norcorrole π -systems was investigated using VT- ^1H NMR and UV/vis/NIR analyses, as well as DFT simulations. Importantly, self-assembled **3-2** exhibits superior charge-transporting ability compared to that of Zn(II) porphyrin analogue **3-11**. It should also be noted here that ester-functionalized norcorrole Ni(II) complex **3-3** and Ni(II) *meso*-di(4-dodecyloxyphenyl)norcorrole **3-4** exhibits no charge-transporting abilities. These results demonstrate that the supramolecular polymerization

of antiaromatic molecules represents a promising strategy for the development of effective carrier-transport materials.

3-8. References

1. Liu, Y.; Coppens, M.-O.; Jiang, Z. *Chem. Soc. Rev.* **2021**, *50*, 11747.
2. (a) Breslow, R. *J. Biol. Chem.* **2009**, *284*, 1337. (b) Shigemitsu, H.; Hamachi, I. *Acc. Chem. Res.* **2017**, *50*, 740.
3. (a) Brienne, M.-J.; Gabard, J.; Lehn, J.-M.; Stibor, I. *J. Chem. Soc., Chem. Commun.* **1989**, 1868. (b) Sijbesma, R. P.; Beijer, F. H.; Brunsveld, L.; Folmer, B. J. B.; Hirschberg, J. H. K. K.; Lange, R. F. M.; Lowe, J. K. L.; Meijer, E. W. *Science* **1997**, *278*, 1601. (c) Kobayashi, Y.; Matsunaga, Y. *Bull. Chem. Soc. Jpn.* **1987**, *60*, 3515. (d) Fouquey, C.; Lehn, J.-M.; Levelut, A.-M. *Adv. Mater.* **1990**, *2*, 254. (e) Sikder, A.; Ghosh, S. *Mater. Chem. Front.* **2019**, *3*, 2602.
4. (a) Velten, U.; Rehahn, M. *Chem. Commun.* **1996**, 2639. (b) Winter, A.; Schubert, U. S. *Chem. Soc. Rev.* **2016**, *45*, 5311. (c) Bentz, K. C.; Cohen, S. M. *Angew. Chem. Int. Ed.* **2018**, *57*, 14992. (d) Fujita, M.; Sasaki, O.; Mitsuhashi, T.; Fujita, T.; Yazaki, J.; Yamaguchi, K.; Ogura, K. *Chem. Commun.* **1996**, 1535. (e) Fujita, D.; Ueda, Y.; Sato, S.; Mizuno, N.; Kumasaka, T.; Fujita, M. *Nature* **2016**, *540*, 563. (f) Kambe, T.; Sakamoto, R.; Hoshiko, K.; Takada, K.; Miyachi, M.; Ryu, J.-H.; Sasaki, S.; Kim, J.; Nakazato, K.; Takata, M.; Nishihara, H. *J. Am. Chem. Soc.* **2013**, *135*, 2462.
5. (a) Chen, Z.; Lohr, A.; Saha-Möller, C. R.; Würthner, F. *Chem. Soc. Rev.* **2009**, *38*, 564. (b) Babu, S. S.; Praveen, V. K.; Ajayaghosh, A. *Chem. Rev.* **2014**, *114*, 1973.
6. (a) Brunsveld, L.; Folmer, B. J. B.; Meijer, E. W.; Sijbesma, R. P. *Chem. Rev.* **2001**, *101*, 4071. (b) Dumele, O.; Chen, J.; Passarelli, J. V.; Stupp, S. I. *Adv. Mater.* **2020**,

- 32, 1907247. (c) Yang, L.; Tan, X.; Wang, Z.; Zhang, X. *Chem. Rev.* **2015**, *115*, 7196.
- (d) Aida, T.; Meijer, E. W.; Stupp, S. I. *Science* **2012**, *335*, 813.
7. (a) Zhang, W.; Jin, W.; Fukushima, T.; Saeki, A.; Seki, S.; Aida, T. *Science* **2011**, *334*, 340. (b) Schenning, A. P. H. J.; Meijer, E. W. *Chem. Commun.* **2005**, 3245. (c) Picini, F.; Schneider, S.; Gavat, O.; Vargas Jentzsch, A.; Tan, J.; Maaloum, M.; Strub, J.-M.; Tokunaga, S.; Lehn, J.-M.; Moulin, E. *J. Am. Chem. Soc.* **2021**, *143*, 6498.
8. (a) Tamaki, H.; Zhong, Z. J.; Matsumoto, N.; Kida, S.; Koikawa, M.; Achiwa, N.; Hashimoto, Y.; Okawa, H. *J. Am. Chem. Soc.* **1992**, *114*, 6974. (b) Decurtins, S.; Schmale, H. W.; Schneuwly, P.; Enslin, J.; Guetlich, P. *J. Am. Chem. Soc.* **1994**, *116*, 9521. (c) Bodenthin, Y.; Pietsch, U.; Möhwald, H.; Kurth, D. G. *J. Am. Chem. Soc.* **2005**, *127*, 3110.
9. (a) Frischmann, P. D.; Gerber, L. C. H.; Doris, S. E.; Tsai, E. Y.; Fan, F. Y.; Qu, X.; Jain, A.; Persson, K. A.; Chiang, Y.-M.; Helms, B. A. *Chem. Mater.* **2015**, *27*, 6765. (b) Kwon, T.; Choi, J. W.; Coskun, A. *Joule* **2019**, *3*, 662.
10. (a) Hoeben, F. J. M.; Jonkheijm, P.; Meijer, E. W.; Schenning, A. P. H. J. Schenning, *Chem. Rev.* **2005**, *105*, 1491. (b) Ghosh, G.; Dey, P.; Ghosh, S. *Chem. Commun.* **2020**, *56*, 6757. (c) Elemans, J. A. A. W.; van Hameren, R.; Nolte, R. J. M.; Rowan, A. E. *Adv. Mater.* **2006**, *18*, 1251.
11. Reviews: (a) Wiberg, K. B. *Chem. Rev.* **2001**, *101*, 1317. (b) Nishinaga, T.; Ohmae, T.; Iyoda, M. *Symmetry* **2010**, *2*, 76. (c) Braunschweig, H.; Kupfer, T. *Chem. Commun.* **2011**, *47*, 10903. (d) Hopf, H. *Angew. Chem. Int. Ed.* **2013**, *52*, 12224. (e) Rosenberg, M.; Dahlstrand, C.; Kilså, K.; Ottosson, H. *Chem. Rev.* **2014**, *114*, 5379. (f) Frederickson, C. K.; Rose, B. D.; Haley, M. M. *Acc. Chem. Res.* **2017**, *50*, 977. (g) Sung, Y. M.; Oh, J.; Cha, W.-Y.; Kim, W.; Lim, J. M.; Yoon, M.-C.; Kim, D.

Chem. Rev. **2017**, *117*, 2257.

12. (a) Kawase, T.; Fujiwara, T.; Kitamura, C.; Konishi, A.; Hirao, Y.; Matsumoto, K.; Kurata, H.; Kubo, T.; Shinamura, S.; Mori, H.; Miyazaki, E.; Takimiya, K. *Angew. Chem., Int. Ed.* **2010**, *49*, 7728. (b) Chase, D. T.; Fix, A. G.; Kang, S. J.; Rose, B. D.; Weber, C. D.; Zhong, Y.; Zakharov, L. N.; Loneragan, M. C.; Nuckolls, C.; Haley, M. M. *J. Am. Chem. Soc.* **2012**, *134*, 10349. (c) Nishinaga, T.; Ohmae, T.; Aita, K.; Takase, M.; Iyoda, M.; Arai, T.; Kunugi, Y. *Chem. Commun.* **2013**, *49*, 5354. (d) Nakano, M.; Osaka, I.; Takimiya, K.; Koganezawa, T. *Mater. Chem. C* **2014**, *2*, 64. (e) Marshall, J. L.; Uchida, K.; Frederickson, C. K.; Schütt, C.; Zeidell, A. M.; Goetz, K. P.; Finn, T. W.; Jarolimek, K.; Zakharov, L. N.; Risko, C.; Herges, R.; Jurchescu, O. D.; Haley, M. M. *Chem. Sci.* **2016**, *7*, 5547.
13. (a) Konishi, A.; Okada, Y.; Nakano, M.; Sugisaki, K.; Sato, K.; Takui, T.; Yasuda, M. *J. Am. Chem. Soc.* **2017**, *139*, 15284. (b) Yoshida, T.; Takahashi, K.; Ide, Y.; Kishi, R.; Fujiyoshi, J.; Lee, S.; Hiraoka, Y.; Kim, D.; Nakano, M.; Ikeue, T.; Yamada, H.; Shinokubo, H. *Angew. Chem.* **2018**, *130*, 2231; *Angew. Chem., Int. Ed.* **2018**, *57*, 2209.
14. (a) Shin, J.-Y.; Yamada, T.; Yoshikawa, H.; Awaga, K.; Shinokubo, H. *Angew. Chem. Int. Ed.* **2014**, *53*, 3096. (b) Hwang, J.; Hagiwara, R.; Shinokubo, H.; Shin, J.-Y. *Mater. Adv.* **2021**, *2*, 2263.
15. An antiaromatic supramolecular cage has been reported; for details, see: Yamashina, M.; Tanaka, Y.; Lavendomme, R.; Ronson, T. K.; Pittelkow, M.; Nitschke, J. R. *Nature* **2019**, *574*, 511.
16. (a) Hafner, K.; Süß, H. U. *Angew. Chem. Int. Ed. Engl.* **1973**, *12*, 575. (b) Chase, D. T.; Rose, B. D.; McClintock, S. P.; Zakharov, L. N.; Haley, M. M. *Angew. Chem. Int.*

- Ed.* **2011**, *50*, 1127. (c) Shimizu, A.; Tobe, Y. *Angew. Chem. Int. Ed.* **2011**, *50*, 6906.
- (d) Iida, A.; Yamaguchi, S. *J. Am. Chem. Soc.* **2011**, *133*, 6952. (e) Wakamiya, A.; Mishima, K.; Ekawa, K.; Yamaguchi, S. *Chem. Commun.* **2008**, 579.
17. Ukai, S.; Koo, Y. H.; Fukui, N.; Seki, S.; Shinokubo, H. *Dalton Trans.* **2020**, *49*, 14383.
18. (a) Nozawa, R.; Tanaka, H.; Cha, W.-Y.; Hong, Y.; Hisaki, I.; Shimizu, S.; Shin, J.-Y.; Kowalczyk, T.; Irle, S.; Kim, D.; Shinokubo, H. *Nat. Commun.* **2016**, *7*, 13620.
- (b) Nozawa, R.; Kim, J.; Oh, J.; Lamping, A.; Wang, Y.; Shimizu, S.; Hisaki, I.; Kowalczyk, T.; Fliegl, H.; Kim, D.; Shinokubo, H. *Nat. Commun.* **2019**, *10*, 3576.
- (c) Kawashima, H.; Ukai, S.; Nozawa, R.; Fukui, N.; Fitzsimmons, G.; Kowalczyk, T.; Fliegl, H.; Shinokubo, H. *J. Am. Chem. Soc.* **2021**, *143*, 10676.
19. Smulders, M. M. J.; Nieuwenhuizen, M. M. L.; de Greef, T. F. A.; van der Schoot, P.; Schenning, A. P. H. J.; Meijer, E. W. *Chem. Eur. J.* **2010**, *16*, 362.
20. (a) Ogi, S.; Sugiyasu, K.; Manna, S.; Samitsu, S.; Takeuchi, M. *Nat. Chem.* **2014**, *6*, 188. (b) Ogi, S.; Fukui, T.; Jue, M. L.; Takeuchi, M.; Sugiyasu, K. *Angew. Chem., Int. Ed.* **2014**, *53*, 14363.
21. Chen, Z.; Wannere, C. S.; Corminboeuf, C.; Puchta, R.; Schleyer, P. von R. *Chem. Rev.* **2005**, *105*, 3842.
22. (a) Valiev, R. R.; Fliegl, H.; Sundholm, D. *Chem. Commun.* **2017**, *53*, 9866. (b) Lehtola, S.; Dimitrova, M.; Fliegl, H.; Sundholm, D. *J. Chem. Theory Comput.* **2021**, *17*, 1457.
23. For selected reviews, see: (a) Zhao, D.; Moore, J. S. *Org. Biomol. Chem.* **2003**, *1*, 3471. (b) Martin, R. B. *Chem. Rev.* **1996**, *96*, 3043. (c) Rest, C.; Kandanelli, R.; Fernández, G. *Chem. Soc. Rev.* **2015**, *44*, 2543. (d) De Greef, T. F. A.; Smulders, M.

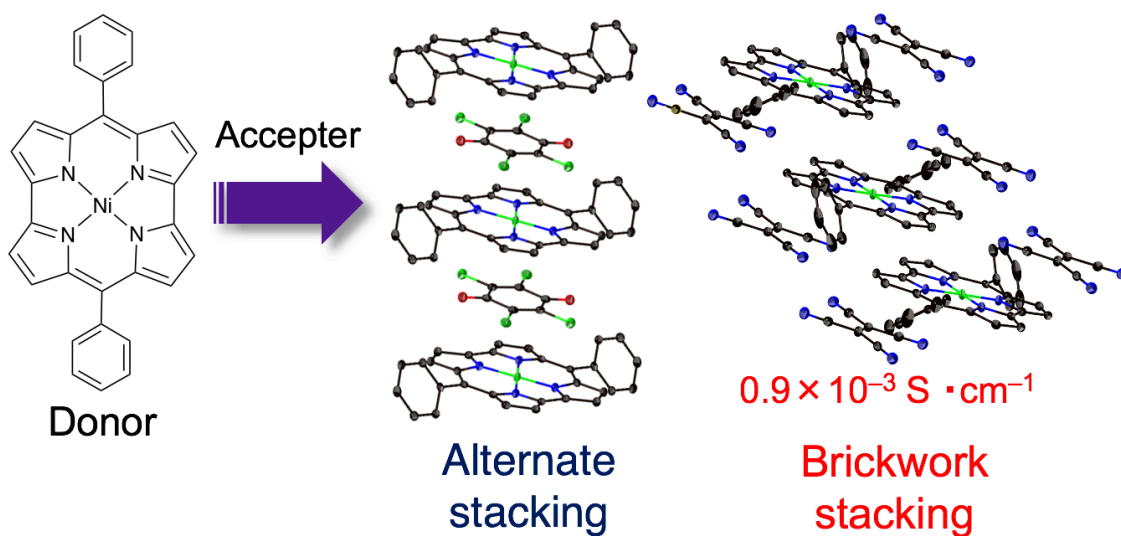
- M. J.; Wolffs, M.; Schenning, A. P. H. J.; Sijbesma, R. P.; Meijer, E. W. *Chem. Rev.* **2009**, *10*, 5687.
24. (a) Jonkheijm, P.; van der Schoot, P.; Schenning, A. P. H. J.; Meijer, E. W. *Science* **2006**, *313*, 80. (b) Smulders, M. M. J.; Schenning, A. P. H. J.; Meijer, E. W. *J. Am. Chem. Soc.* **2008**, *130*, 606.
25. Fujii, S.; Marqués-González, S.; Shin, J.-Y.; Shinokubo, H.; Masuda, T.; Nishino, T.; Arasu, N. P.; Vázquez, H.; Kiguchi, M.S. *Nat. Commun.* **2017**, *8*, 15984.
26. (a) Seki, S.; Saeki, A.; Sakurai, T.; Sakamaki, D. *Phys. Chem. Chem. Phys.* **2014**, *16*, 11093. (b) S. Kato, Y. Serizawa, D. Sakamaki, S. Seki, Y. Miyake, H. Shinokubo, *Chem. Commun.* **2015**, *51*, 16944. (c) K. Tajima, K.; Matsuo, H. Yamada, S. Seki, N. Fukui, H. Shinokubo. *Angew. Chem., Int. Ed.* **2021**, *60*, 14060.
27. Kingsbury, C. J.; Senge, M. O. *Coord. Chem. Rev.* **2021**, *431*, 213760.
28. The value was estimated on the cooling process. From the re-heating process, the enthalpy was estimated to be -116 kJ mol^{-1}
29. The solid sample was prepared by freeze-drying the solution of **3-11**. The FT-IR peak due to the hydrogen-bonding interactions is similar to that observed in solution.
30. The solid sample was prepared by dripping a $70 \text{ }\mu\text{M}$ solution of **3-3** in cyclohexane/benzene (9/1) onto a thin film and drying slowly at room temperature under reduced pressure.
31. The solid sample was prepared by freeze-drying the solution of **3-2**. The FT-IR peak due to the hydrogen-bonding interactions is similar to that observed in solution (Figure 3-14).
32. Gaussian 09, Revision D.01, Frisch, M. J.; Trucks, G. W.; Schlegel, H. B.; Scuseria, G. E.; Robb, M. A.; Cheeseman, J. R.; Scalmani, G.; Barone, V.; Mennucci, B.;

Petersson, G. A.; Nakatsuji, H.; Caricato, M.; Li, X.; Hratchian, H. P.; Izmaylov, A. F.; Bloino, J.; Zheng, G.; Sonnenberg, J. L.; Hada, M.; Ehara, M.; Toyota, K.; Fukuda, R.; Hasegawa, J.; Ishida, M.; Nakajima, T.; Honda, Y.; Kitao, O.; Nakai, H.; Vreven, T.; Montgomery, Jr., J. A.; Peralta, J. E.; Ogliaro, F.; Bearpark, M.; Heyd, J. J.; Brothers, E.; Kudin, K. N.; Staroverov, V. N.; Kobayashi, R.; Normand, J.; Raghavachari, K.; Rendell, A.; Burant, J. C.; Iyengar, S. S.; Tomasi, J.; Cossi, M.; Rega, N.; Millam, J. M.; Klene, M.; Knox, J. E.; Cross, J. B.; Bakken, V.; Adamo, C.; Jaramillo, J.; Gomperts, R.; Stratmann, R. E.; Yazyev, O.; Austin, A. J.; Cammi, R.; Pomelli, C.; Ochterski, J. W.; Martin, R. L.; Morokuma, K.; Zakrzewski, V. G.; Voth, G. A.; Salvador, P.; Dannenberg, J. J.; Dapprich, S.; Daniels, A. D.; Farkas, Ö.; Foresman, J. B.; Ortiz, J. V.; Cioslowski, J.; Fox, D. J. Gaussian, Inc., Wallingford CT, 2009.

Chapter 3

Chapter 4

Charge transfer complexes of antiaromatic Ni(II) norcorroles



Contents

4-1. Introduction	82
4-2. Preparation of CT complexes	85
4-3. Charge transport properties	88
4-4. ESR measurements.....	89
4-5. Conductivity of TCNE co-crystal	90
4-6. Summary of Chapter 4	92
4-7. References	93

4-1. Introduction

Electronic characters of solid materials dramatically change depending on the type and arrangement of their constituent atoms and molecules. In particular, solid molecular materials enable a greater diversity of material designs than inorganic materials due to their flexibility in tuning the electronic structure and the shape of the constituent molecules. The challenge of developing solid-state materials based on organic molecules in the first stages focused on creating conductive functions. Half a century of scientists' efforts to control the electronic structure and crystallinity of molecules has succeeded in the development of organic metals¹ and organic superconductors.²

“Charge-Transfer (CT) complexes” are aggregates composed of electron donors and electron acceptors. In recent years, charge transfer complexes have attracted much attention over the last few decades because of their potential for electronic properties such as semiconductivity,³ ferroelectricity,⁴ photoresponsivity,⁵ and stimuli responsivity.⁶ In addition, CT complexes often form higher-order aggregates in the solid state, where both stacking pattern and ionicity are important factors dominating their electronic properties (Figure 4-1).⁷

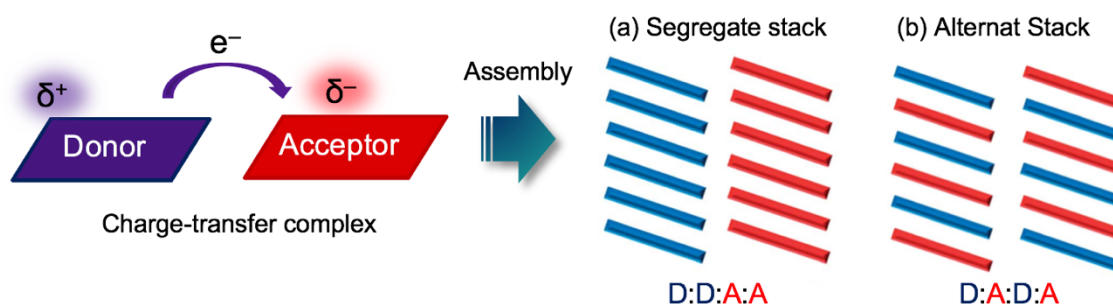


Figure 4-1. Formation of charge transfer complexes and typical observed two types stacking structures (a) segregate stack (b) alternate stack; D: donor A: acceptor.

To form the CT complexes, polycyclic aromatic hydrocarbons (PAHs: such as perylene and pyrene) were used as donors in early studies (Figure 4-2a).⁸ However, the charge-transfer complexes of PAHs with strong oxidants gradually decompose due to the instability of the aggregates. Consequently, strongly electron-donating compounds that form stable CT complexes are necessary for material applications. Weitz-type is well known for strong donors and charge-stabilizing properties due to the formation of stable aromatic rings upon oxidation.⁹ However, there are limited examples of molecules that can exhibit such properties and the TTF analogues have been the most commonly used electron donor in this field (Figure 4-2b).

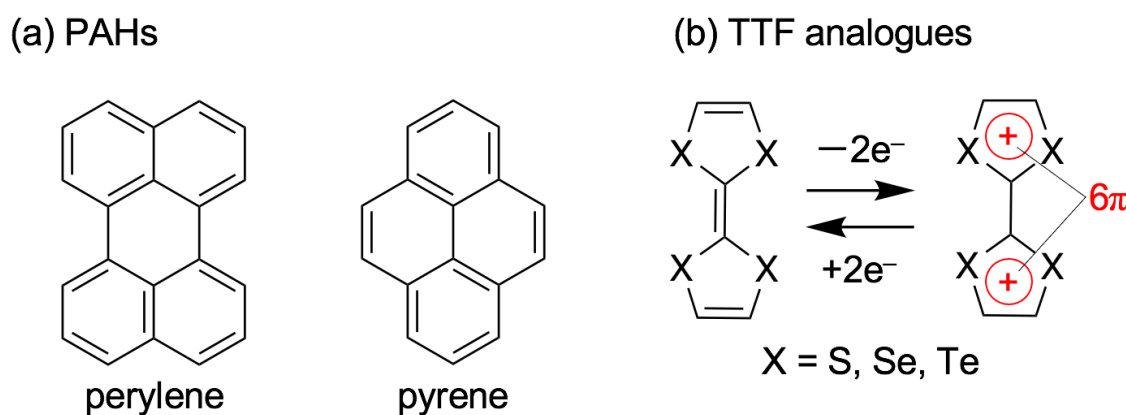


Figure 4-2. Structure of electron donors (a) perylene and pyrene examined in early studies (b) TTF analogues and redox-mechanism.

Against this background, the author focused on antiaromatic compounds. These compounds have a destabilized HOMO and a stabilized LUMO, thus they would possess potentials for excellent electron donors and acceptors.¹⁰ However, antiaromatic molecules are inherently unstable and require kinetic stabilization by bulky substituents, which hamper effective intermolecular interactions between donors and acceptors in aggregates.¹¹

Ni(II) *meso*-dimesitylnorcorrole is a stable and distinctly antiaromatic molecule

with a 16 π -electronic system, which exhibits reversible multi-redox abilities due to their narrow HOMO–LUMO energy gap.^{12,13} Furthermore, Ni(II) norcorrole exhibits high stability despite the lack of steric protection by bulky *meso*-substituents, as discussed in Chapter 2.¹⁴ These features well satisfy the requirements for CT complex formation. In Chapter 4, the author describes the formation of CT complexes based on antiaromatic Ni(II) norcorrole (Figure 4-1).

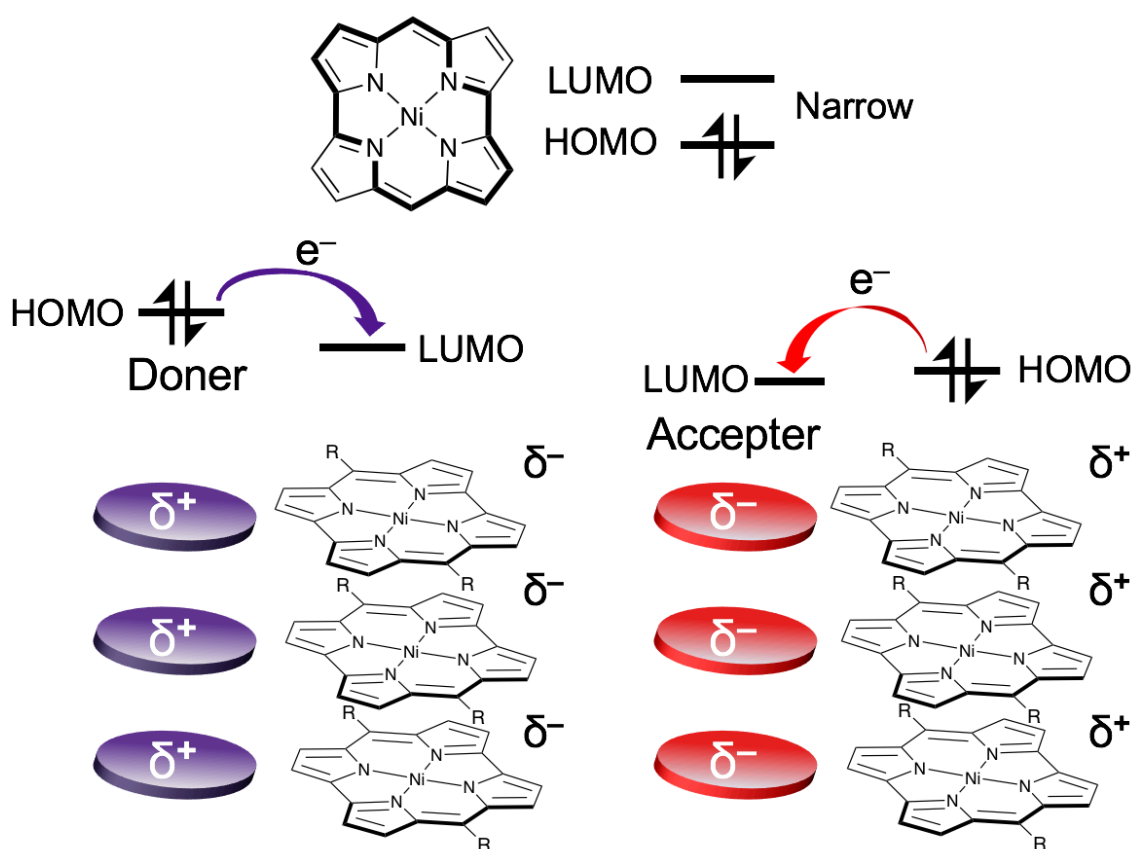


Figure 4-3. Formation of CT complexes based on antiaromatic Ni(II) norcorroles.

4-2. Preparation of CT complexes

Trial and error are necessary to obtain single crystals of CT complexes suitable for X-ray structural analysis. Furthermore, the raw material should be pure and available in sufficient quantities to obtain a single crystal reproducibly. To satisfy these requirements, Ni(II) *meso*-diphenylporphyrin **4-1** was chosen as the antiaromatic molecule.¹⁵ In 2020, the author reported that **4-1** shows excellent stability in solution without bulky substituents stabilization. In addition, **4-1** can be easily synthesized without purification using silica gel column chromatography.¹⁴ Next, the first oxidation and reduction potentials of **4-1** obtained from the CV measurements were evaluated to judge whether **4-1** is a suitable donor or acceptor molecule (Figure 4-4). The first oxidation wave of **4-1** was observed at 0.0 V vs. a ferrocene/ferrocenium couple (Fc/Fc⁺) in CH₂Cl₂. This value shows that **4-1** has superior donor properties than common aromatic molecules such as pyrene, perylene, and coronene. The value is comparable to TTF (−0.01 V). On the other hand, the first reduction wave of **4-1** was observed at −0.82 V vs. Fc/Fc⁺, which means **4-1** would be a weaker acceptor compared to benzoquinone, TCNE, and TCNQ. According to these considerations, Formation of CT complexes was carried out using **4-1** as a donor.

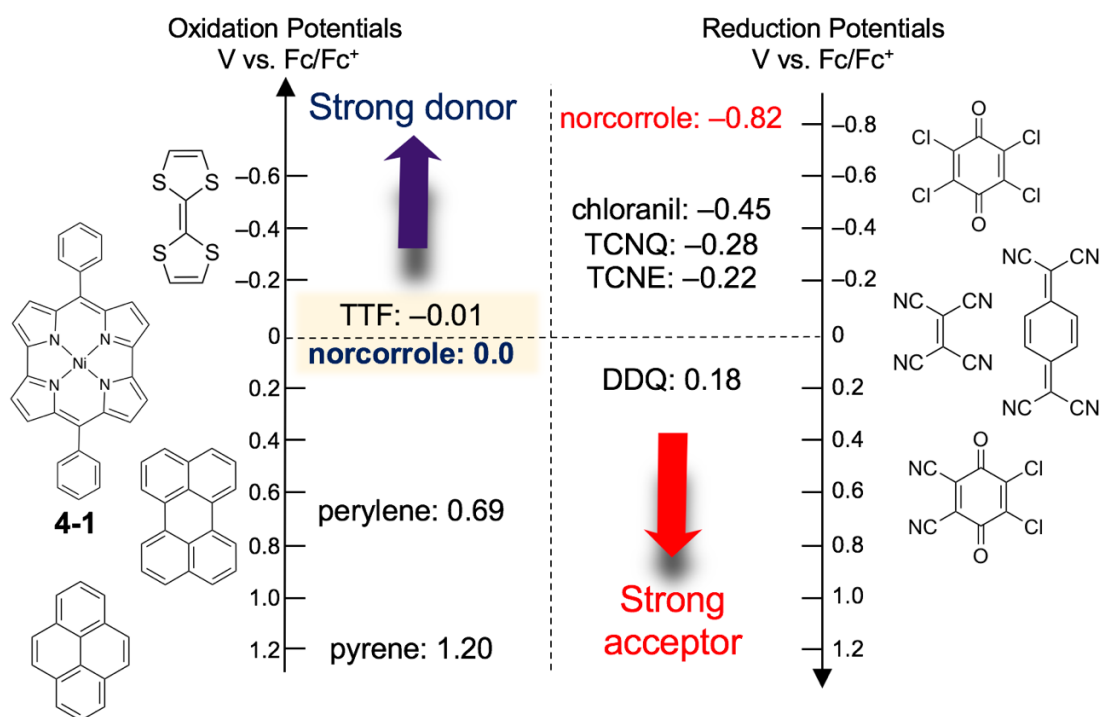


Figure 4-4. Redox potentials of **4-1** along with those of various donors and acceptors.

A mixture of **4-1** and an acceptor in solution was co-crystallized by vapor diffusion. As a result, four co-crystals of **4-1**•chloranil, **4-1**•bromanil, **4-1**•fluoranil, and **4-1**•TCNE were obtained, of which structures were unambiguously elucidated by single-crystal X-ray structure analysis. All of these co-crystals contained **4-1** and the acceptor in a ratio of 1:1. All the co-crystals with benzoquinones showed an alternate stacking structure (Figure 4-3, 4-4, and 4-5). In the co-crystals of **4-1**•chloranil and **4-1**•bromanil, a highly symmetric crystal system (trigonal) was observed than **4-1**•fluoranil (monoclinic), in which the stacked columns were arranged in a hexagonal pattern. The co-crystal of **4-1**•TCNE showed a brickwork structure with a partial contact between the norcorrole π -planes (Figure 4-6).

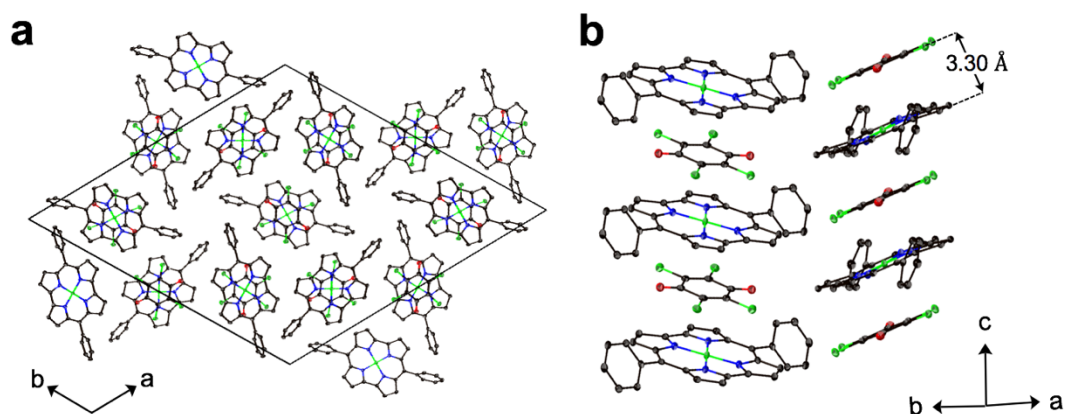


Figure 4-5. X-ray crystal structure of 4-1•chloranil co-crystal (a) top (b) side view. Thermal ellipsoids are drawn at the 50% probability level. All hydrogen atoms are omitted for clarity.

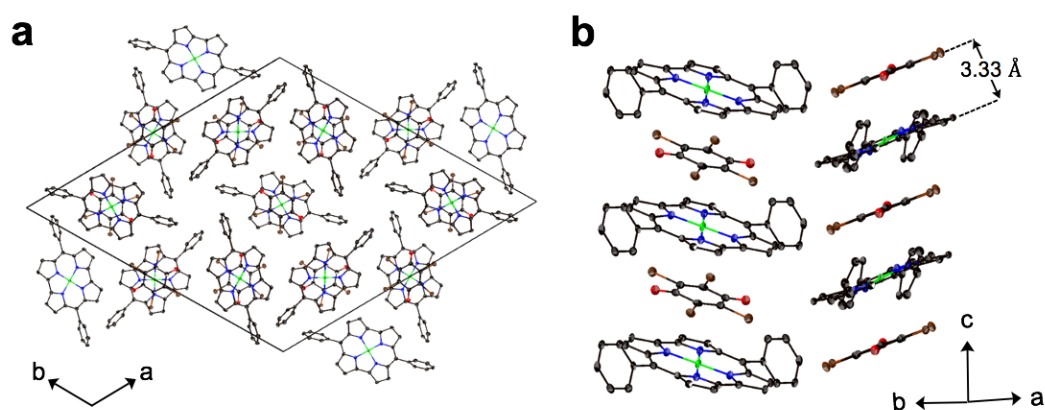


Figure 4-6. X-ray crystal structure of 4-1•bromanil co-crystal (a) top (b) side view. Thermal ellipsoids are drawn at the 50% probability level. All hydrogen atoms are omitted for clarity.

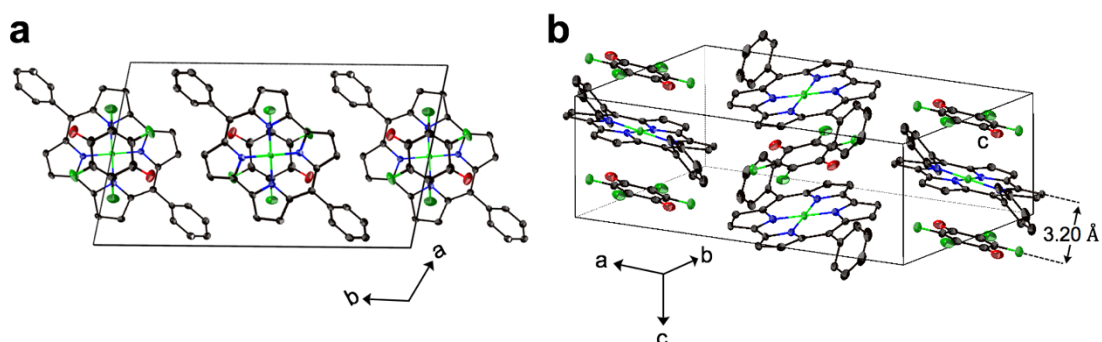


Figure 4-7. X-ray crystal structure of 4-1•fluoranil co-crystal (a) top (b) side view. Thermal ellipsoids are drawn at the 50% probability level. All hydrogen atoms are omitted for clarity.

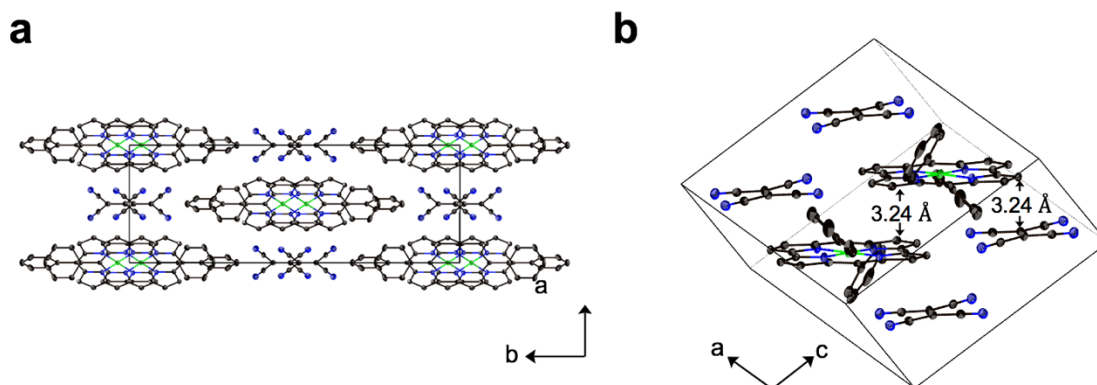


Figure 4-8. X-ray crystal structure of **4-1•TCNE** co-crystal (a) top (b) side view. Thermal ellipsoids are drawn at the 50% probability level. All hydrogen atoms are omitted for clarity.

4-3. Charge transport properties

The author examined the electronic photo-conduction of Ni(II) *meso*-diphenylporphyrin **4-1•benzoquinones** (fluoranil, bromanil, and chloranil) and **4-1•TCNE** co-crystals by flash-photolysis time-resolved microwave conductivity (FP-TRMC) measurement in their microcrystalline states. Electrodeless photocarrier injection was performed upon excitation at 355 nm where the electronic transitions of the series of molecules are minimum, securing the homogeneous photocarrier distribution in their crystalline states. The observed photoconductivity transients are shown in Figure 4-9. The **4-1•TCNE** co-crystal showed the highest photoconductivity than the other benzoquinone co-crystals in all-time ranges up to $\sim 100 \mu\text{s}$. Notably, the TRMC signal of **4-1•TCNE** co-crystal was highly stable over a long period of time, which suggests that a long conductive pathway stabilizes the generated carriers.

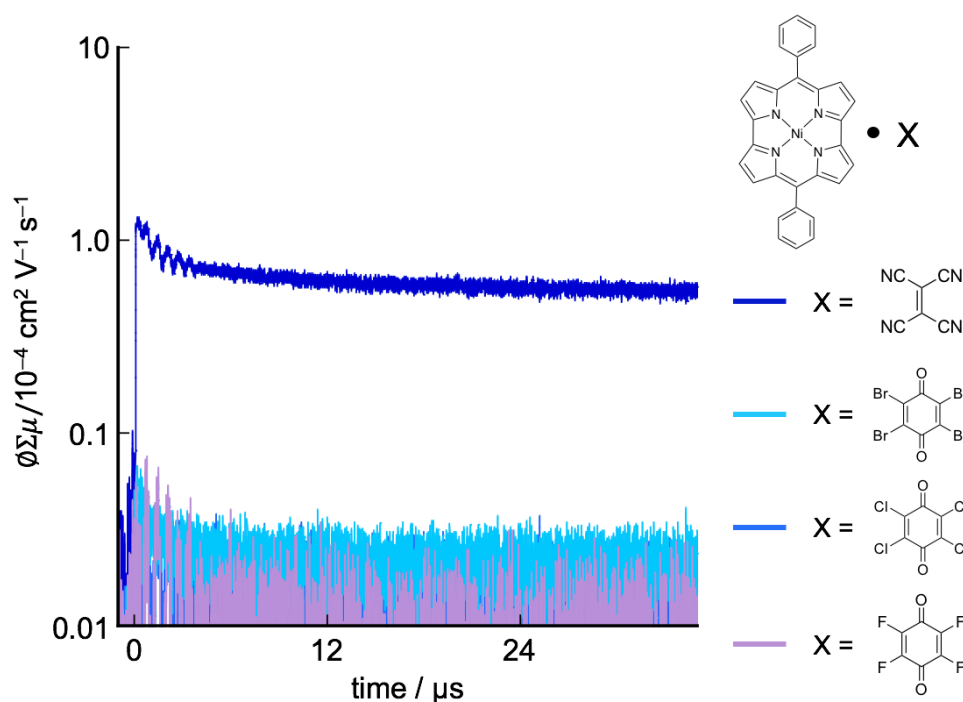


Figure 4-9. Photoconductivity transients recorded in microcrystalline **4-1**•TCNE (blue), **4-1**•bromanil (pink), **4-1**•bromanil (light blue), and **4-1**•fluoranil (red), respectively upon excitation at 355 nm, $0.2\text{--}1.3 \times 10^{15}$ photons cm^{-2} , r.t.

4.4. ESR measurements

To observe the carrier generation by the charge transfer, solid ESR measurements were carried out at room temperature (Figure 4-10). Weak ESR signals were observed for the Ni(II) *meso*-diphenylporphyrin **4-1**•benzoquinones (fluoranil, bromanil, and chloranil), suggesting that the charge transfer in these complexes is almost negligible. In contrast, a stronger ESR signal was observed for **4-1**•TCNE than for **4-1**•benzoquinones. Next, the spin density was estimated to be ca. 0.2% for each benzoquinone, while a value of 2.4% was estimated for **4-1**•TCNE.¹⁶ In addition, the *g*-values of 2.005, 2.005, 2.004, and 2.005 were obtained for **4-1**•TCNE, **4-1**•bromanil, **4-1**•chloranil, and **4-1**•fluoranil, which indicates that the electronic spins are delocalized over the porphyrin unit and each acceptor.

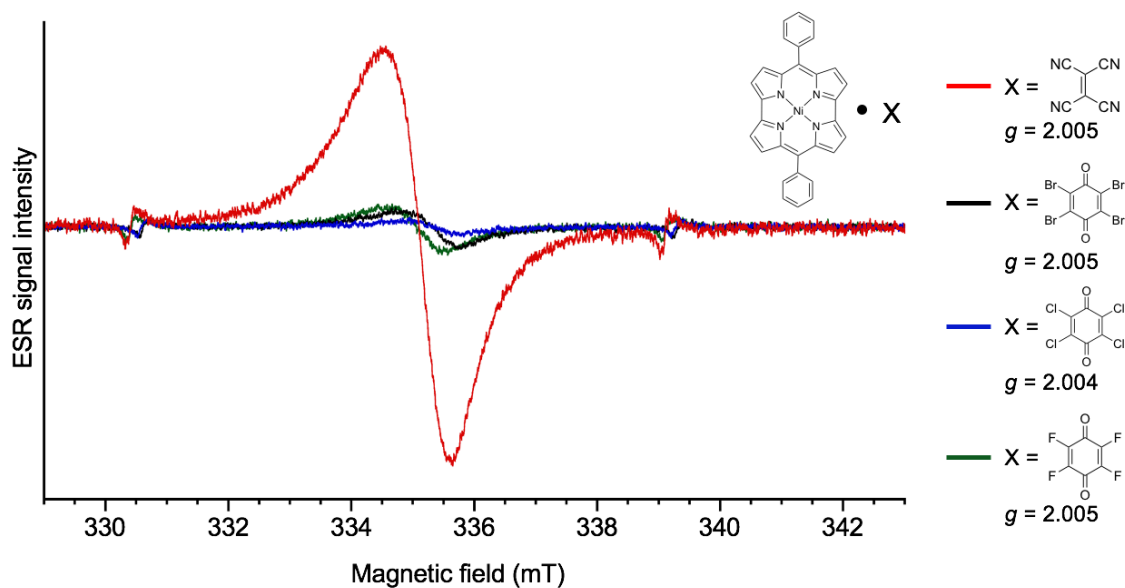


Figure 4-10. ESR measurements of **4-1**•TCNE (blue), **4-1**•bromanil (pink), **4-1**•chloranil (light blue), and **4-1**•fluoranil (red) in the solid state at room temperature.

4-5. Conductivity of TCNE co-crystal

TRMC and ESR measurements revealed the formation of conductive pathways and the generation of carriers in the Ni(II) *meso*-diphenylporphyrin **4-1**•TCNE co-crystal. Then, the author investigated the electrical conductivity of the single crystal. However, large crystals could not be obtained with **4-1**•TCNE co-crystal. Therefore, the conductivity was investigated by the two-terminal method the following procedure: placing a crystal on a silicon substrate and then coating silver paste on both ends of the crystal and contacting the electrodes (Figure 4-11a,b).

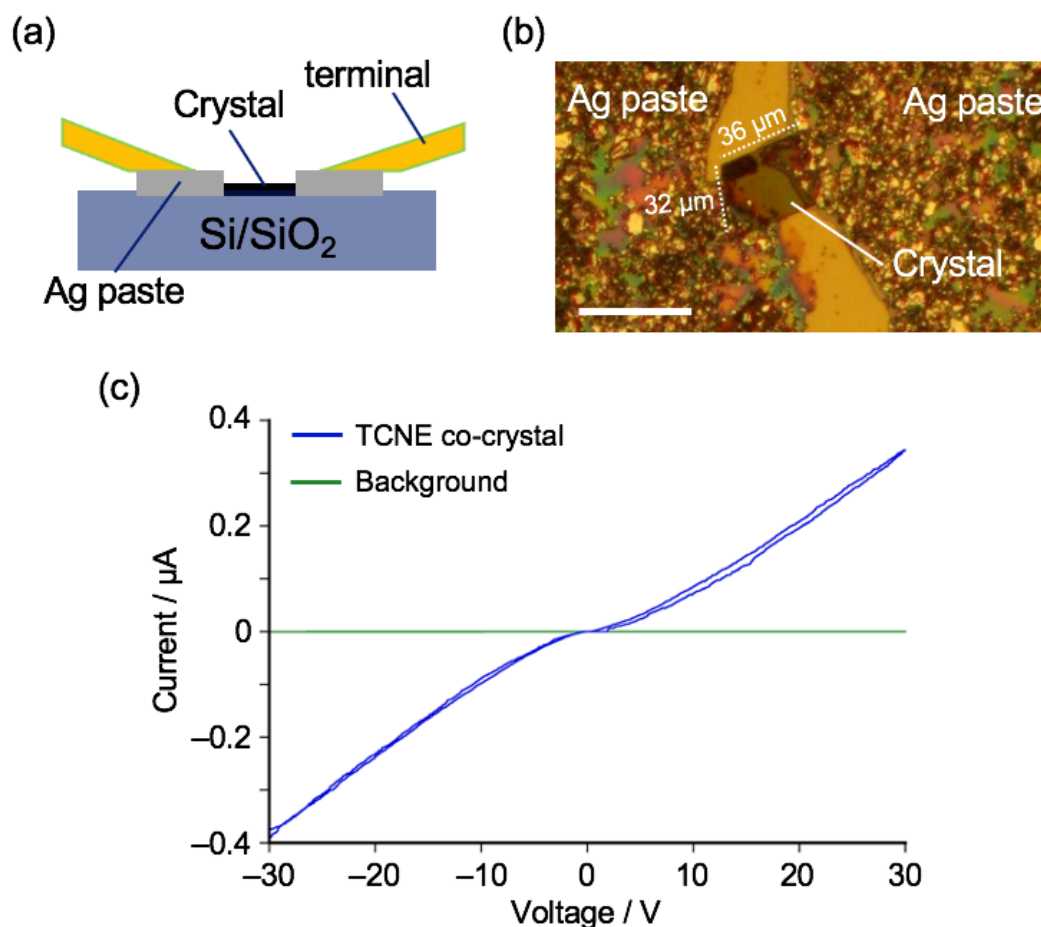


Figure 4-11. (a) Schematic diagram of conductivity measurement. (b) Microscope picture. The bar is 50 μm. (c) Measurement of conductivity in the 4-1•TCNE co-crystal (blue) and a silicon substrate (red) under air, r.t.

Upon applying a voltage to the crystal, the current was almost proportional to the voltage. In contrast, the conductivity of the silicon substrate was not observed, which supports the conductive nature of the TCNE co-crystal (Figure 4-11c). Furthermore, no hysteresis currents were observed, despite the atmospheric conditions. These results of TRMC and conductivity measurements indicate that the carriers are sufficiently stable.

To determine the conductivity, the crystal size was estimated. The surface area was determined from the microscopic measurement (Figure 4-11b). The height of the crystal was measured by atomic force microscopy (AFM) and the topology phase image of the

crystal showed the presence of a smooth flat surface (Fig. 4-12a). The height profile is shown along the white line in Fig. 4-10a. A step with the substrate was observed, the height was determined to be about ca. 300 nm (Fig. 4-10b). From these results, the conductivity was estimated to be $0.9 \times 10^{-3} \text{ S cm}^{-1}$, which value is much higher than those of most of single-component closed-shell aromatic molecules but lower than those of the segregated stacked charge-transfer complexes.¹⁷ The overlap between the TCNEs may not act as a conduction pathway due to the small π -systems. In other words, the conduction pathway in **4-1**•TCNE co-crystal is mainly formed by the overlap norcorrole π -systems.

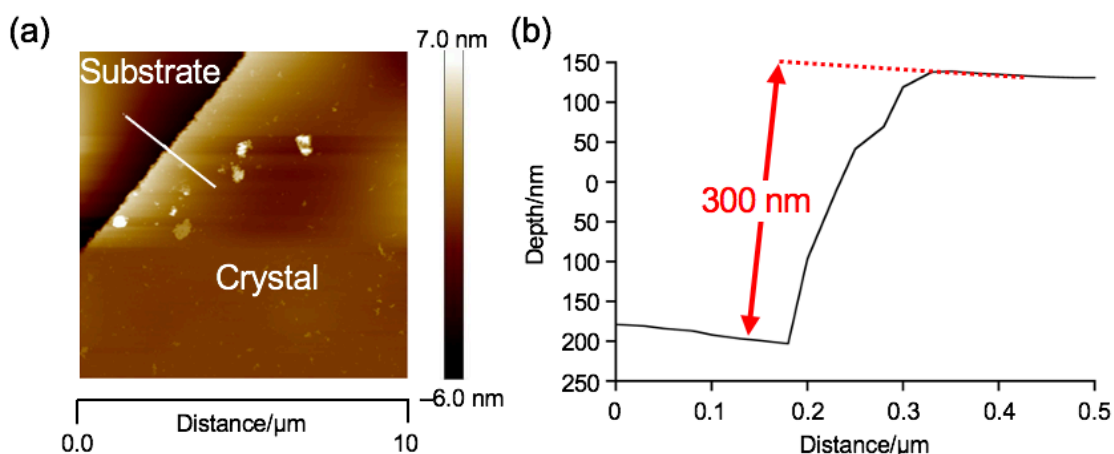


Figure 4-12. (a) AFM topological image of a **4-1**•TCNE co-crystal onto silicon. (b) Height profile of the fibers measured along the white line in the AFM image.

4-6. Summary of Chapter 4

In summary, the formation of CT complexes based on antiaromatic Ni(II) *meso*-diphenylporcorrole **4-1** as a donor was successful. Alternate stacking was observed in co-crystals with benzoquinones as an acceptor. Interestingly, **4-1**•chloranil and **4-1**•bromanil co-crystals exhibited a highly symmetric crystal system, in which the stacked columns were arranged in a hexagonal pattern. In co-crystal with TCNE, brickwork stacking was

observed. X-ray structure analysis and TRMC measurements revealed that stable conductive pathways were formed in the 4-1•TCNE co-crystal. The co-crystal exhibited moderate conductivity. These results indicate the potential of CT complexes based on Ni(II) norcorroles as electronic materials in the future.

4-7. References

- 1 (a) Ferraris, John.; Cowan, D. O.; Walatka, V.; Perlstein, J. H. *J. Am. Chem. Soc.* **1973**, *95*, 948. (b) Shirakawa, H.; Louis, E. J.; MacDiarmid, A. G.; Chiang, C. K.; Heeger, A. J. *J. Chem. Soc., Chem. Commun.* **1977**, 578.
- 2 (a) Jérôme, D.; Mazaud, A.; Ribault, M.; Bechgaard, K. *J. Phys. Lett.* **1980**, *41*, 95. (b) Bechgaard, K.; Carneiro, K.; Rasmussen, F. B.; Olsen, M.; Rindorf, G.; Jacobsen, C. S.; Pedersen, H. J.; Scott, J. C. *J. Am. Chem. Soc.* **1981**, *103*, 2440. (c) Saito, G.; Yoshida, Y. *Chem. Rec.* **2011**, *11*, 124.
- 3 (a) Niwa, S. *Synth. Met.* **1987**, *18*, 665. (b) Takahashi, Y.; Hasegawa, T.; Abe, Y.; Tokura, Y.; Saito, G. *Appl. Phys. Lett.* **2006**, *88*, 073504.
- 4 (a) Tayi, A. S.; Shveyd, A. K.; Sue, A. C.-H.; Szarko, J. M.; Roleczynski, B. S.; Cao, D.; Kennedy, T. J.; Sarjeant, A. A.; Stern, C. L.; Paxton, W. F.; Wu, W.; Dey, S. K.; Fahrenbach, A. C.; Guest, J. R.; Mohseni, H.; Chen, L. X.; Wang, K. L.; Stoddart, J. F.; Stupp, S. *Nature* **2012**, *488*, 485. (b) Kobayashi, K.; Horiuchi, S.; Kumai, R.; Kagawa, F.; Murakami, Y.; Tokura, Y. *Phys. Rev. Lett.* **2012**, *108*. (c) Kagawa, F.; Horiuchi, S.; Matsui, H.; Kumai, R.; Onose, Y.; Hasegawa, T.; Tokura, Y. *Phys. Rev. Lett.* **2010**, *104*.
- 5 Wang, W.; Luo, L.; Sheng, P.; Zhang, J.; Zhang, Q. *Chem. Eur. J.* **2020**, *27*, 464.
- 6 Sun, L.; Yang, F.; Zhang, X.; Hu, W. *Mater. Chem. Front.* **2020**, *4*, 715.

Chapter 4

- 7 (a) Torrance, J. B. *Acc. Chem. Res.* **1979**, *12*, 79. (b) Torrance, J. B.; Vazquez, J. E.; Mayerle, J. J.; Lee, V. Y. *Phys. Rev. Lett.* **1981**, *46*, 253. (c) Saito, G.; Murata, T. *Philos. Trans. Royal Soc. A.* **2007**, *366*, 139.
- 8 (a) AKAMATU, H.; INOKUCHI, H.; MATSUNAGA, Y. *Nature* **1954**, *173*, 168. (b) Akamatu, H.; Inokuchi, H.; Matsunaga, Y. *Bull. Chem. Soc. Jpn.* **1956**, *29*, 213.
- 9 Deuchert, K.; Hünig, S. *Angew. Chem. Int. Ed.* **1978**, *17*, 875.
- 10 (a) Minsky, A.; Meyer, A. Y.; Rabinovitz, M. *Tetrahedron* **1985**, *41*, 785. (b) Wiberg, K. B. *Chem. Rev.* **2001**, *101*, 1317. (c) Nishinaga, T.; Ohmae, T.; Iyoda, M. *Symmetry*, **2010**, *2*, 76. (d) Nishinaga, T.; Ohmae, T.; Aita, K.; Takase, M.; Iyoda, M.; Arai, T.; Kunugi, Y. *Chem. Commun.* **2013**, *49*, 5354. (e) Braunschweig, H.; Kupfer, T. *Chem. Commun.* **2011**, *47*, 10903.
- 11 (a) Hafner, K.; Süss, H. U. *Angew. Chem. Int. Ed. Engl.* **1973**, *12*, 575. (b) Chase, D. T.; Rose, B. D.; McClintock, S. P.; Zakharov, L. N.; Haley, M. M. *Angew. Chem. Int. Ed.* **2011**, *50*, 1127. (c) Shimizu, A.; Tobe, Y. *Angew. Chem. Int. Ed.* **2011**, *50*, 6906. (d) Iida, A.; Yamaguchi, S. *J. Am. Chem. Soc.* **2011**, *133*, 6952. (e) Wakamiya, A.; Mishima, K.; Ekawa, K.; Yamaguchi, S. *Chem. Commun.* **2008**, 579.
- 12 Ito, T.; Hayashi, Y.; Shimizu, S.; Shin, J.; Kobayashi, N.; Shinokubo, H. *Angew. Chem. Int. Ed.* **2012**, *51*, 8542.
- 13 (a) Shin, J.-Y.; Yamada, T.; Yoshikawa, H.; Awaga, K.; Shinokubo, H. *Angew. Chem. Int. Ed.* **2014**, *53*, 3096. (b) Hwang, J.; Hagiwara, R.; Shinokubo, H.; Shin, J.-Y. *Mater. Adv.* **2021**, *2*, 2263.
- 14 Ukai, S.; Koo, Y. H.; Fukui, N.; Seki, S.; Shinokubo, H. *Dalton Trans.* **2020**, *49*, 14383.

- 15 Nozawa, R.; Tanaka, H.; Cha, W.-Y.; Hong, Y.; Hisaki, I.; Shimizu, S.; Shin, J.-Y.; Kowalczyk, T.; Irle, S.; Kim, D.; Shinokubo, H. *Nat. Commun.* **2016**, *7*, 13620.
- 16 These values were determined using stable radical 1-Oxyl-2,2,6,6-tetramethyl-4-hydroxypiperidine (TEMPOL) as the reference molecule. The amount of substance of unpaired electrons was determined from the ESR intensity of TEMPOL and the ESR intensity ratio of each crystals, and the obtained value was divided by the sum of the number of molecules in each crystals.
- 17 Goetz, K. P.; Vermeulen, D.; Payne, M. E.; Kloc, C.; McNeil, L. E.; Jurchescu, O. *D. J. Mater. Chem. C*, **2014**, *2*, 3065.

Chapter 4

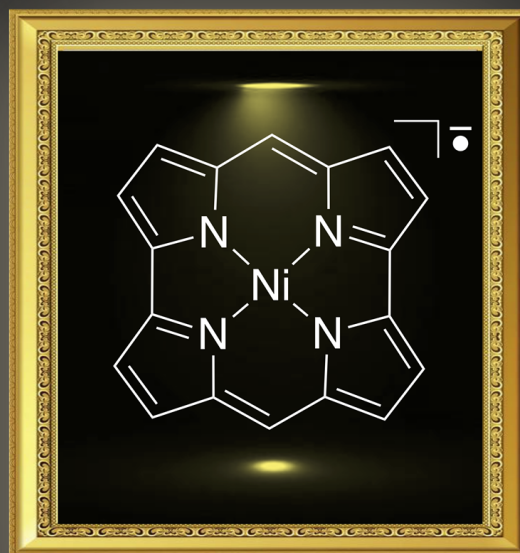
Chapter 5

Isolation and structure analysis of a Ni(II) norcorrole radical anion

Find the differences

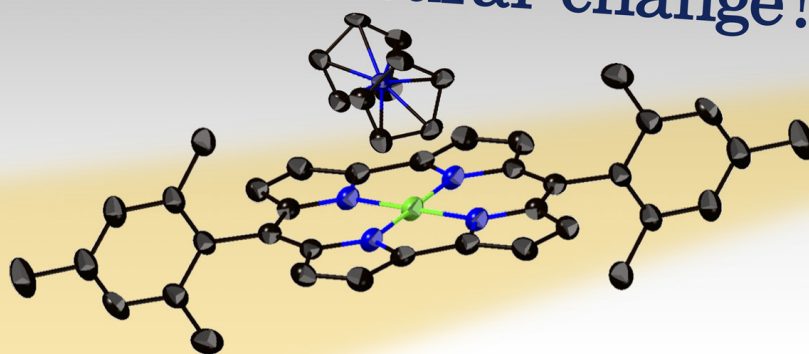


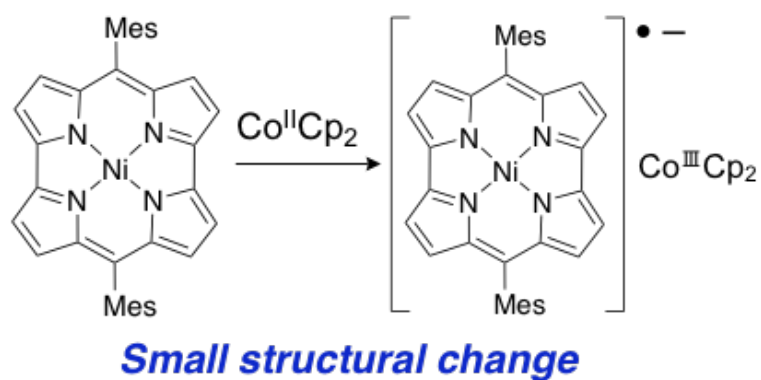
Neutral



Radical anion

Small structural change!





Contents

5-1. Introduction.....	99
5-2. Chemical reduction of 5-1.....	100
5-3. Structural analysis.....	102
5-4. Electronic structure.....	103
5-5. Electronic structure.....	106
5-6. Reorganization energy.....	107
5-7. Summary of Chapter 5.....	110
5-8. References.....	110

5-1. Introduction

The development of both p-type and n-type organic semiconductors is essential for the creation of next-generation materials such as organic transistors, diodes, and solar cells.¹ However, practical n-type organic materials with high electron mobility are fewer than p-type ones, thus being an attractive research target.² One general guideline to realize high carrier mobility is to suppress structural change upon charge injection, leading to small reorganization energies.³ Consequently, the creation of π -conjugated molecules with small structural changes upon electron injection should be attractive targets.

Ni(II) *meso*-dimesitylnorcorrole **5-1** is a stable and distinctly antiaromatic molecule with a 16 π -electronic system, which exhibits multi-redox abilities due to their narrow HOMO–LUMO energy gap (Figure 5-1).⁴ Owing to the excellent reversibility of its redox process, rechargeable batteries were successfully fabricated using **5-1** as the electrode active material.⁵ Furthermore, the author demonstrated that *meso*-dimethylnorcorrole **5-2** formed one-dimensional π -stacking in the solid state, leading to its n-type semiconducting property as shown in Chapter 2.⁶ Against this background, isolation and characterization of the radical ion species are required to understand the redox process of norcorroles. However, the isolation of a radical anion of norcorrole without electronic modulation has not been reported. The isolation of radical anion has been limited to the work of Li, Chmielewski, and co-workers in 2016, in which they reported the synthesis of Ni(II) *meso*-dimesityl tetranitronorcorrole **5-3** and succeeded in isolation of its radical anion **5-4** stabilized by the electron-withdrawing substituents.⁷

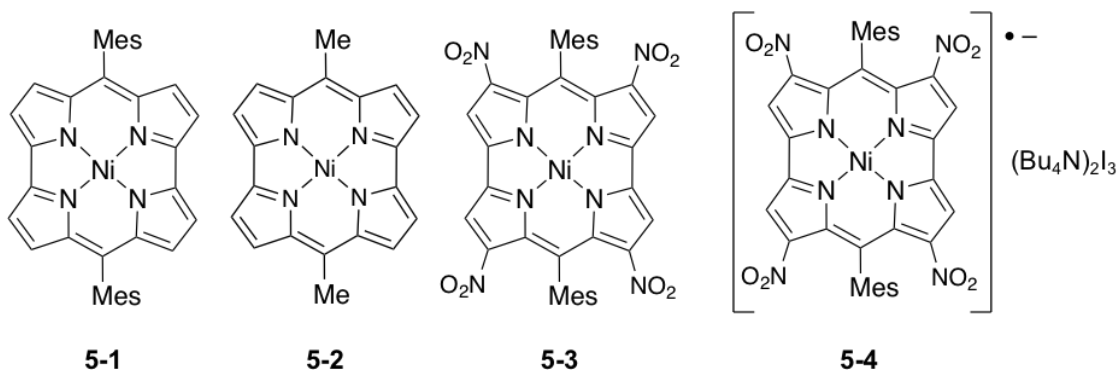
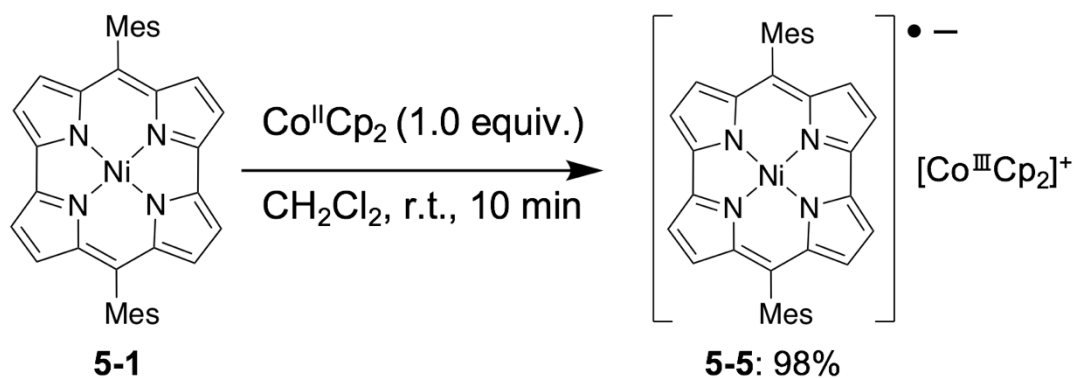


Figure 5-1. Structure of Ni(II) *meso*-dimesitylnorcorrole **5-1**, Ni(II) *meso*-dimethylnorcorrole **5-2**, nitrated Ni(II) norcorrole **5-3**, and radical anion **5-4**.

In Chapter 5, the author described that one-electron reduction of Ni(II) *meso*-dimesitylnorcorrole **5-1** with cobaltocene (Co^{II}Cp²) provided its radical anion **5-5**. Even without thermodynamic stabilization with electron-withdrawing groups, **5-5** exhibited high stability in the solid state and can be handled in a degassed solution for a long period. Furthermore, the X-ray diffraction analysis of radical anion **5-5** elucidated that one-electron reduction of **5-1** resulted in small changes in its bond lengths. The small reorganization energy upon one-electron injection has been further supported by theoretical calculations.

5-2. Chemical reduction of 5-1

The first reduction wave of **5-1** was observed at -0.92 V vs a ferrocene/ferrocenium couple (Fc/Fc⁺).⁴ Accordingly, Co^{II}Cp₂, whose first oxidation potential is -1.33 V (vs Fc/Fc⁺) in CH₂Cl₂, was selected as a one-electron reducing agent.⁸ Treatment of **5-1** with Co^{II}Cp₂ afforded its radical anion salt **5-5** in 95% yield as a green solid (Scheme 5-1). The ¹H NMR spectrum of **5-5** was broad because of its paramagnetic nature. A peak for the counter cation ([Co^{III}Cp₂]⁺) was detected at $\delta = 5.85$ ppm (Figure 5-2).



Scheme 5-1. Reduction of **5-1** to provide radical anion **5-5**.

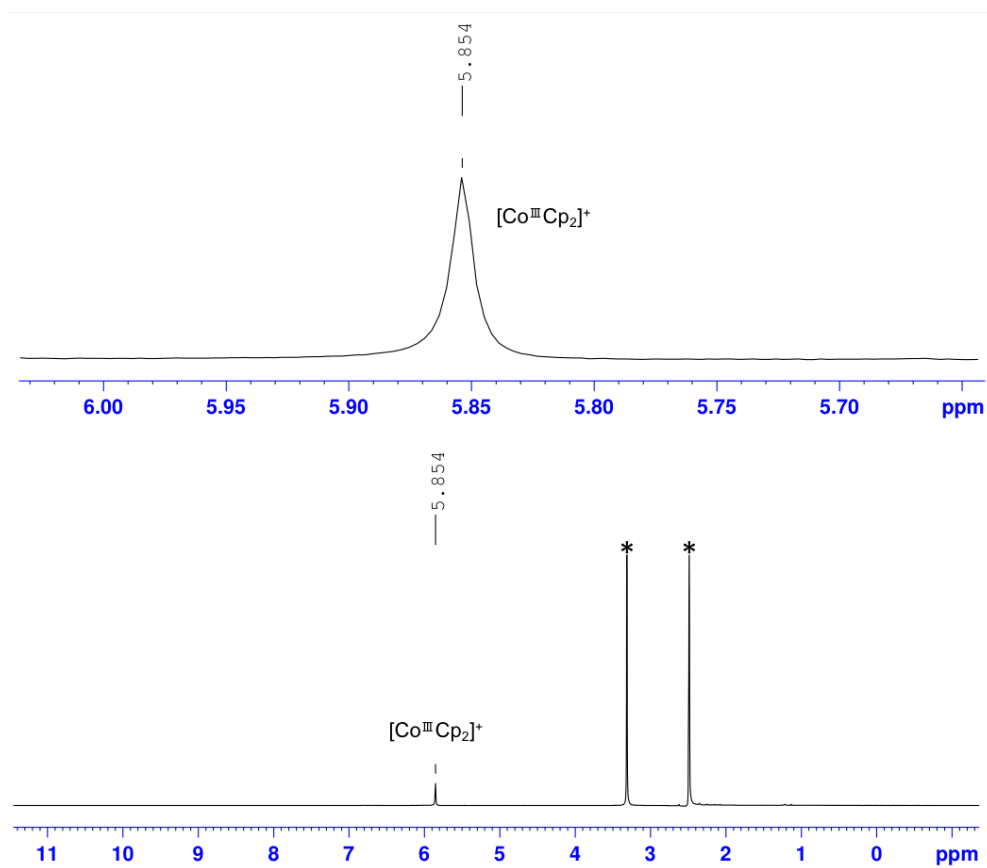


Figure 5-2. ^1H NMR spectrum of **5-5** in $\text{DMSO}-d_6$ at 25 °C. *Solvent peaks.

5-3. Structural analysis

The structure of **5-5** was unambiguously elucidated by single-crystal X-ray structure analysis (Figure 5-3). The single crystal was obtained by slow evaporation of DMSO under reduced pressure. The norcorrole radical anion accompanied the counter ion ($[\text{Co}^{\text{III}}\text{Cp}_2]^+$) in a ratio of 1:1. Norcorrole radical anion **5-5** exhibits a highly planar structure with the mean plane deviation (MPD) of 0.011 Å, which is comparable to that of neutral Ni(II) *meso*-dimesitylnorcorrole **5-2** (0.041 Å). This high planarity is suitable for the effective delocalization of electronic spin over the norcorrole π -systems. In the crystal packing, the norcorrole radical anion and cobaltocenium are alternatively stacked. The magnetic interaction between norcorrole radical anions and cobaltocenium cation is assumed to be negligible.

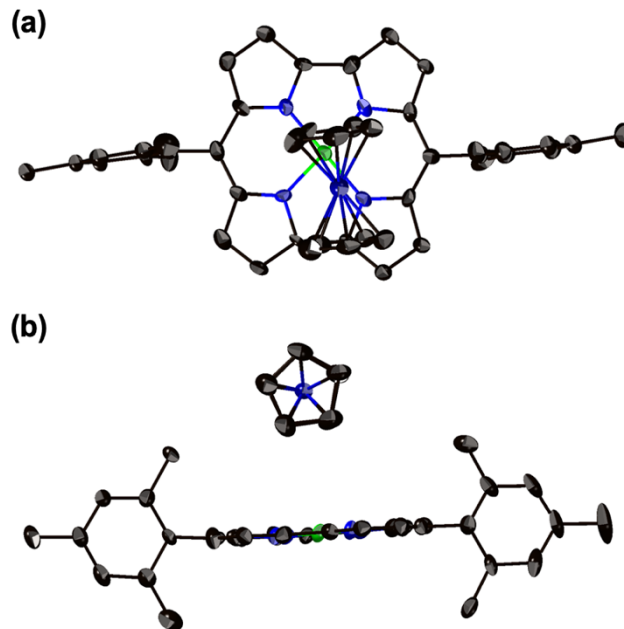


Figure 5-3. X-ray crystal structure of **5-5**. (a) Top and (b) side view of **5-5**. Thermal ellipsoids are drawn at the 50% probability level. All hydrogen atoms are omitted for clarity.

5-4. Electronic structure

The electronic structure was evaluated using UV/vis/NIR absorption spectroscopy. The UV/vis/NIR absorption spectra of Ni(II) *meso*-dimesitylnorcorrole **5-1** and **5-5** in DMSO are shown in Figure 5-4. Neutral norcorrole **5-1** exhibited broad and weak absorption bands tailing to 900 nm. Radical anion **5-5** exhibited a sharp and strong absorption band at 924 nm along with weak absorption tailing to ca. 1400 nm. In addition, new peaks at 488 and 649 nm appeared. These absorption changes are consistent with those previously observed by the spectroelectrochemical measurements.^{5a} Time-dependent density functional theory (TD-DFT) calculations at the UB3LYP/6-31G(d)+SDD level suggested that the strong absorption at 924 nm is originated from the SOMO→LUMO transition (Figure 5-5).

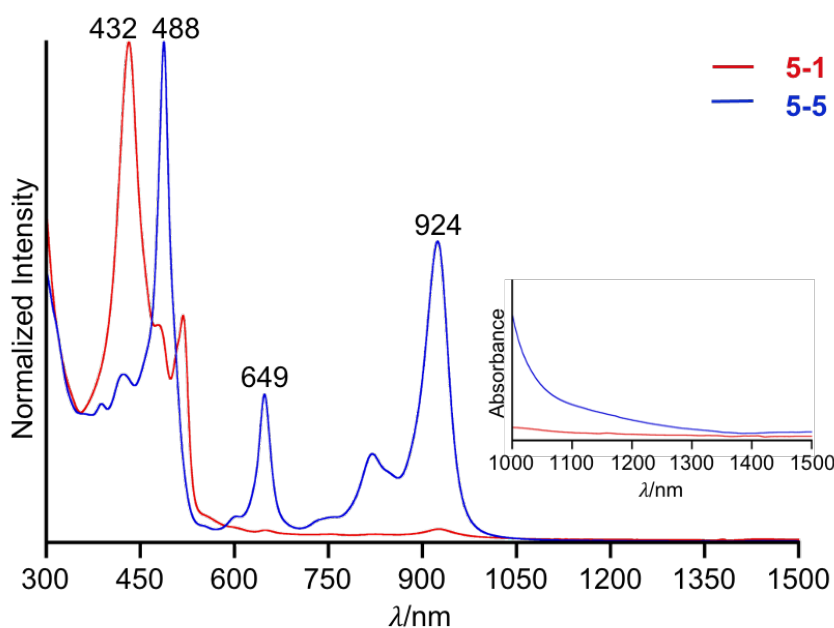


Figure 5-4. UV/Vis/NIR absorption spectra of **5-1** (red) and **5-5** (blue) in DMSO. λ = wavelength.

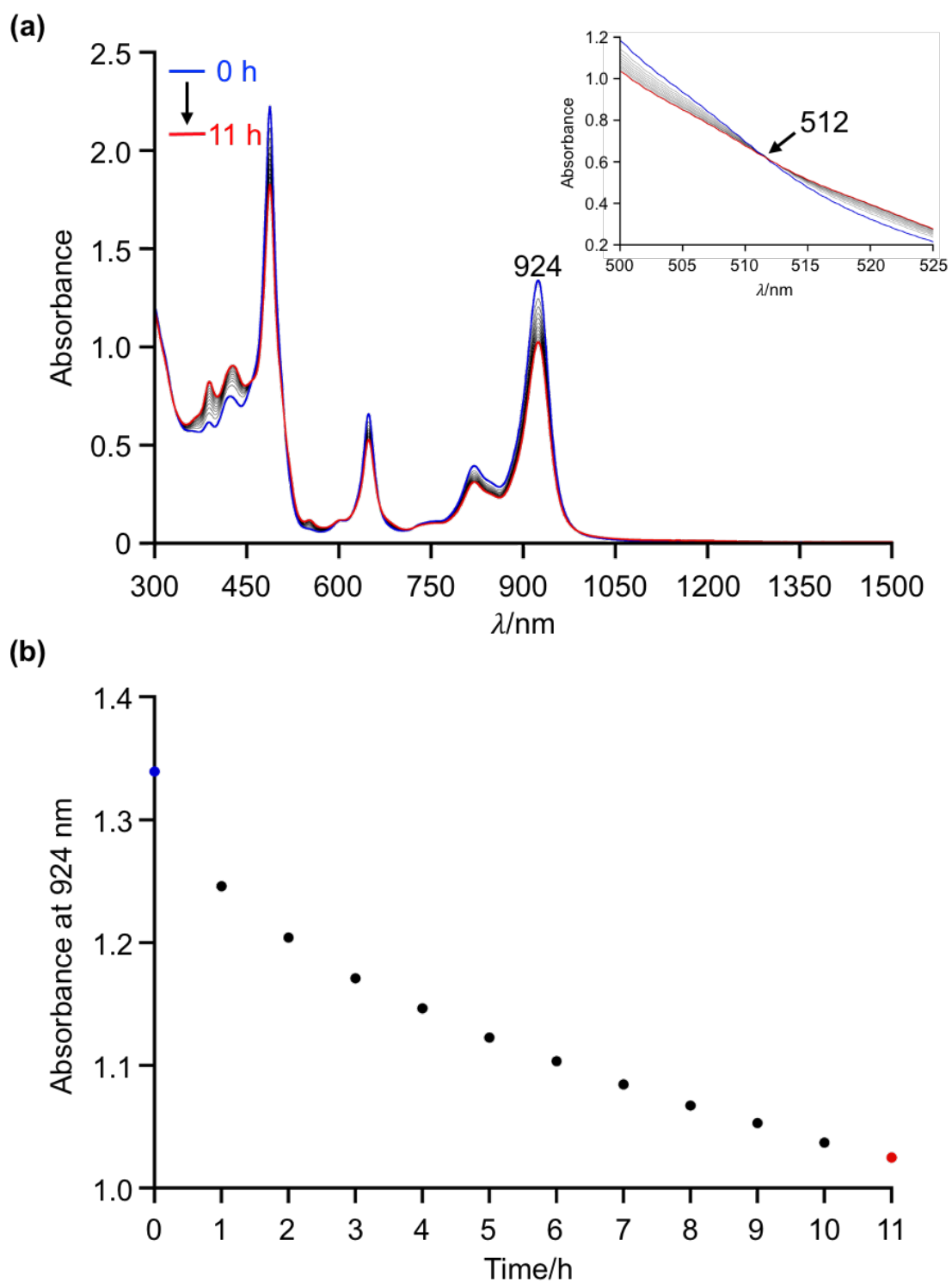


Figure 5-6. a) Time dependence of UV/vis/NIR absorption changes of 5-5 in DMSO under air at room temperature. b) at 924 nm.

5-5. Electronic structure

To obtain information on the magnetic property of **5-5**, the author conducted electron spin resonance (ESR) measurements. The ESR spectra of **5-5** recorded in a DMSO solution¹⁰ at 15 K exhibited a signal at g -value 2.0026, indicating that the electronic spin is delocalized on the norcorrole ligand (Figure 5-7). The spin-density distribution of **5-5** was calculated at the UB3LYP/6-31G+SDD level (Figure 5-8a,b). Negligible spin-densities were detected on the nickel center, which result explains well the g -value obtained by ESR measurements. On the other hand, the electronic spin is highly delocalized over the norcorrole π -systems.

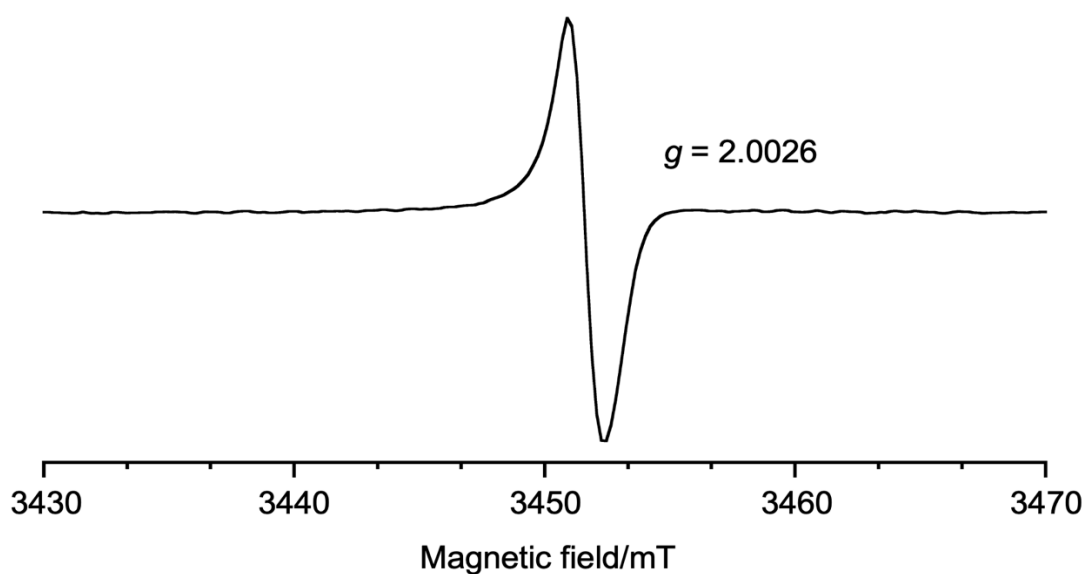


Figure 5-7. ESR spectrum of **5-5** recorded in DMSO at 15 K.

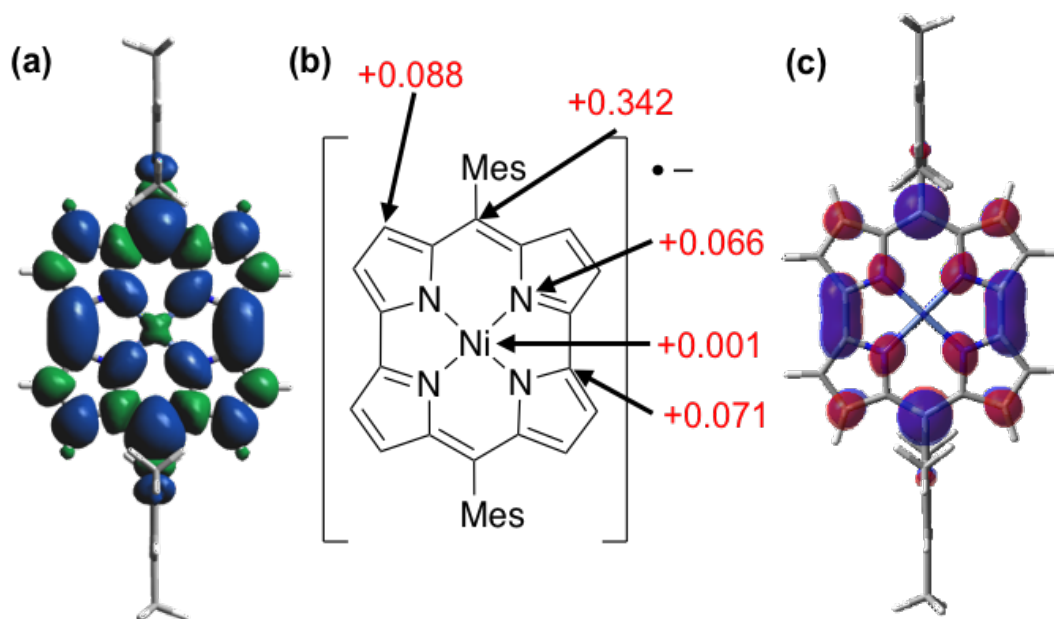


Figure 5-8. (a) Spin-density distribution of **5-5** calculated at the UB3LYP/6-31G+SDD level (isovalue: 0.001, blue: positive spin, green: negative spin). (b) The value of the positive spin-density assigned to each atom. (c) LUMO of **5-5** calculated at the B3LYP/6-31G+SDD level (isovalue: 0.03).

5-6. Reorganization energy

The detailed structure of **5-5** was compared with those of Ni(II) *meso*-dimesitylnorcorrole **5-1** to obtain more insight into the structural changes upon electron-injection (Figure 5-9). There were no significant changes except for a decrease in bond length alternation around *meso*-positions. The harmonic oscillator model of aromaticity (HOMA)¹¹ value of **5-5** is 0.57, which is slightly higher than the neutral species **5-5** (0.43). These results suggest that the structural change of Ni(II) norcorrole **5-1** is small for one-electron reduction.

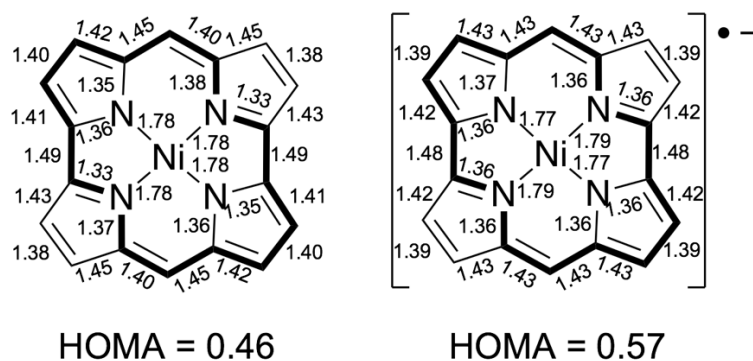


Figure 5-9. Bond lengths in X-ray crystal structures of **5-1** and **5-5**. Mesityl groups are omitted for clarity.

Encouraged by the small structural change during electron doping, the author conducted the DFT calculations to evaluate the reorganization energy at the CAM-B3LYP/6-31G(d)+SDD level (Table 5-1). The reorganization energy was evaluated based on the adiabatic potential energy surfaces method.¹³ The reorganization energy of **5-1**, C₆₀ fullerene, and Zn(II) porphyrin for one-electron reduction and oxidation processes were calculated by the CAM-B3LYP/6-31G(d)+SDD level (Table 5-1). Reorganization energy was estimated based on following equations Eq. 5-1 and Eq. 5-2.

$$\lambda^{(1)} = E^{(1)}(M) - E^{(0)}(M) \quad (\text{Eq. 1})$$

$$\lambda^{(2)} = E^{(1)}(M^{\bullet-\text{or}+}) - E^{(0)}(M^{\bullet-\text{or}+}) \quad (\text{Eq. 2})$$

Here, $E^{(0)}(M)$ and $E^{(0)}(M^{\bullet-}$ or $M^{\bullet+})$ are the energies of the neutral and radical ion states in their ground states, respectively. $E^{(1)}(M)$ is the energy of the neutral molecule in the optimized geometry of the radical ion and $E^{(1)}(M^{\bullet-}$ or $M^{\bullet+})$ is the energy of the radical ions at the optimized geometry of the neutral molecule. The total reorganization energy was determined by the sum of the relaxation energies of $\lambda^{(1)}$ and $\lambda^{(2)}$.

The reorganization energy of **5-1** through the one-electron reduction process was

calculated to be 149 meV, of which value is comparable to that of C₆₀ (183 meV) and smaller than that of aromatic Zn(II) porphyrin (259 meV). The author also calculated the reorganization energy for the one-electron oxidation process of **5-1** to be 246 meV, which is larger than that of the one-electron reduction process. Chao and co-worker proposed that the enhanced non-bonding character in frontier orbitals is related to the decrease in the reorganization energy.¹² In this regard, the LUMO of **5-1** exhibits nonbonding feature except for the two C–C bonds between pyrrole rings (Figure 5-8c).

Table 5-1. Relaxation energies ($\lambda^{(1)}$ and $\lambda^{(2)}$) and reorganization energy ($\lambda^{(1)+\lambda^{(2)}}$) (meV).

5-1	$\lambda^{(1)}$	$\lambda^{(2)}$	$\lambda^{(1)+\lambda^{(2)}}$
Reduction	74.8	74.7	149
Oxidation	111	135	246
C ₆₀ fullerene	$\lambda^{(1)}$	$\lambda^{(2)}$	$\lambda^{(1)+\lambda^{(2)}}$
Reduction	89.7	92.8	183
Oxidation	89.8	91.0	181
Zn(II) porphyrin	$\lambda^{(1)}$	$\lambda^{(2)}$	$\lambda^{(1)+\lambda^{(2)}}$
Reduction	151	108	259
Oxidation	60.4	60.9	121

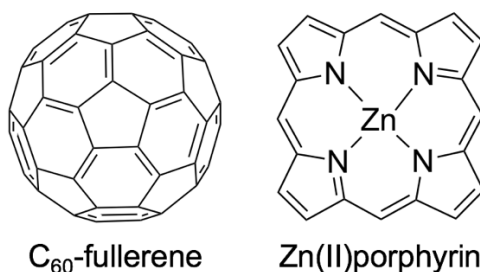


Figure 5-10. Structure of Zn(II) porphyrin and C₆₀ fullerene used for calculation of the reorganization energy.

5-7. Summary of Chapter 5

In summary, Ni(II) *meso*-dimesitylnorcorrole radical anion **5-5** was isolated through chemical reduction of the corresponding neutral species **5-1**. The radical anion **5-5** can be stored for long periods in the solid state, indicating its highly stable nature. The structure of **5-5** was elucidated by X-ray structure analysis, which indicates the small structural change between neutral species **5-1** and radical anion **5-5**. The DFT calculations elucidated the small reorganization energy of norcorrole **5-1** upon one-electron injection. The current study highlights attractive features of norcorrole, namely (1) high stability of radical anion, (2) small reorganization energy upon electron-injection, and (3) good electron-affinity as seen in its reduction potential of -0.92 V (vs Fc/Fc⁺). These properties should be helpful for the development of high-performance n-type semiconductors in the future.

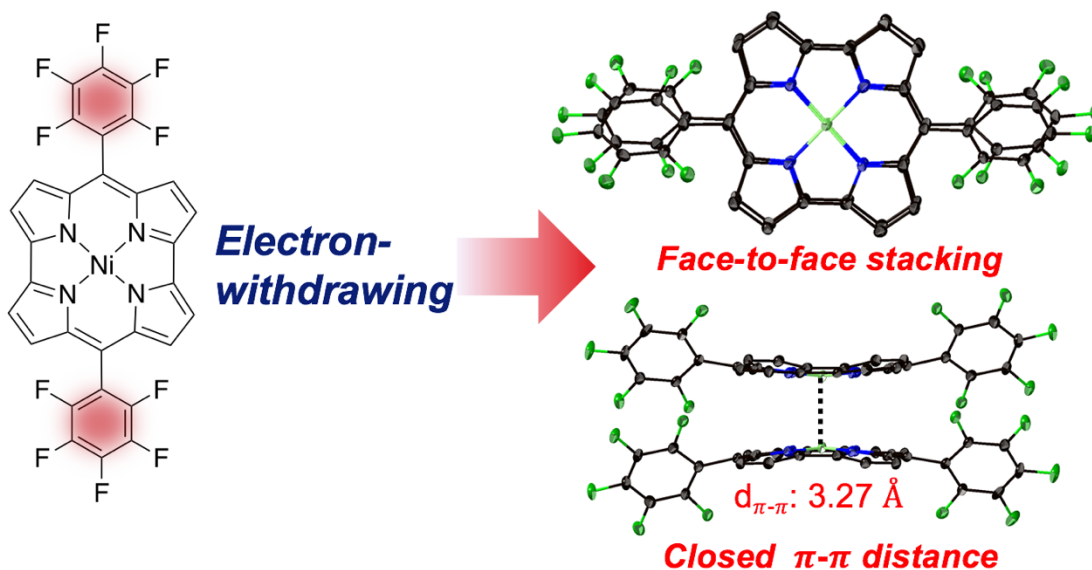
5-8. References

- 1 (a) Takimiya, K.; Kunugi, Y.; Otsubo, T. *Chem. Lett.* **2007**, *36*, 578. (b) Anthony, J. E. *Chem. Rev.* **2006**, *106*, 5028. (c) Anthony, J. E. *Angew. Chem., Int. Ed.* **2008**, *47*, 452. (d) Wen, Y.; Liu, Y. *Adv. Mater.* **2010**, *22*, 1331. (e) Murphy, A. R.; Fréchet, J. M. *Chem. Rev.* **2007**, *107*, 1066. (f) Wang, C.; Dong, H.; Hu, W.; Liu, Y.; Zhu, D. *Chem. Rev.* **2012**, *112*, 2208.
- 2 (a) Newman, C. R.; Frisbie, C. D.; da Silva Filho, D. A.; Brédas, J.-L.; Ewbank, P. C.; Mann, K. R. *Chem. Mater.* **2004**, *16*, 4436. (b) Quinn, J. T. E.; Zhu, J.; Li, X.; Wang, J.; Li, Y. *Mater. Chem. C* **2017**, *5*, 8654. (c) Lan, S.; Yan, Y.; Yang, H.; Zhang,

- G.; Ye, Y.; Li, F.; Chen, H.; Guo, T. *J. Mater. Chem. C* **2019**, *7*, 4543. (d) Jung, B. J.; Tremblay, N. J.; Yeh, M.-L.; Katz, H. E. *Chem. Mater.* **2011**, *23*, 568.
- 3 (a) Marcus, R. A. *Annu. Rev. Phys. Chem.* **1964**, *15*, 155. (b) Marcus, R. A. *Rev. Mod. Phys.* **1993**, *65*, 599.
- 4 Ito, T.; Hayashi, Y.; Shimizu, S.; Shin, J.; Kobayashi, N.; Shinokubo, H. *Angew. Chem. Int. Ed.* **2012**, *51*, 8542.
- 5 (a) Shin, J.-Y.; Yamada, T.; Yoshikawa, H.; Awaga, K.; Shinokubo, H. *Angew. Chem., Int. Ed.* **2014**, *53*, 3096. (b) Hwang, J.; Hagiwara, R.; Shinokubo, H.; Shin, J.-Y. *Mater. Adv.* **2021**, *2*, 2263.
- 6 Ukai, S.; Koo, Y. H.; Fukui, N.; Seki, S.; Shinokubo, H. *Dalton Trans.* **2020**, *49*, 14383.
- 7 Deng, Z.; Li, X.; Stepien, M.; Chmielewski, P. J. *Chem. Eur. J.* **2016**, *22*, 4231.
- 8 Connelly, N. G.; Geiger, W. E. *Chem. Rev.* **1996**, *96*, 877.
- 9 The mean plane was defined by the 22 core atoms consisting of *meso*-carbons and four pyrrole units.
- 10 Radical anion **5-5** is poorly soluble in less polar solvents such as toluene, CH₂Cl₂, and THF. Attempts to measure the ESR spectrum of **5-5** in these solvents were failed.
- 11 Krygowski, T. M.; Cyrański, M. K. *Chem. Rev.* **2001**, *101*, 1385.
- 12 Chang, Y.-C.; Chao, I. *J. Phys. Chem. Lett.* **2009**, *1*, 116.
- 13 Hutchison, G. R.; Ratner, M. A.; Marks, T. J. *J. Am. Chem. Soc.* **2005**, *127*, 2339.

Chapter 6

Synthesis of Ni(II) *meso*- di(pentafluorophenyl)norcorrole



Contents

6-1. Introduction	114
6-2. Synthesis of Ni(II) <i>meso</i> -di(pentafluorophenyl)norcorrole.....	115
6-3. Structural analysis	116
6-4. Electronic structure	117
6-5. Summary of Chapter 6	119
6-6. References	119

6-1. Introduction

The stacking of antiaromatic π -systems exhibits three-dimensional aromaticity due to the effective orbital interactions through space.¹ In fact, the three-dimensional aromaticity of stacked Ni(II) norcorroles has been demonstrated.² Notably, a cyclophane type Ni(II) norcorrole linked by two flexible alkyl chains **6-1** exhibits a stronger attractive interaction than that of aromatic Ni(II) porphyrin **6-2** (Figure 6-1).^{2c} However, such linker assistances are not suitable for dense integration and crystal structure control. Consequently, other approaches are necessary to form the higher-order structures based on the interactions of antiaromatic compounds.

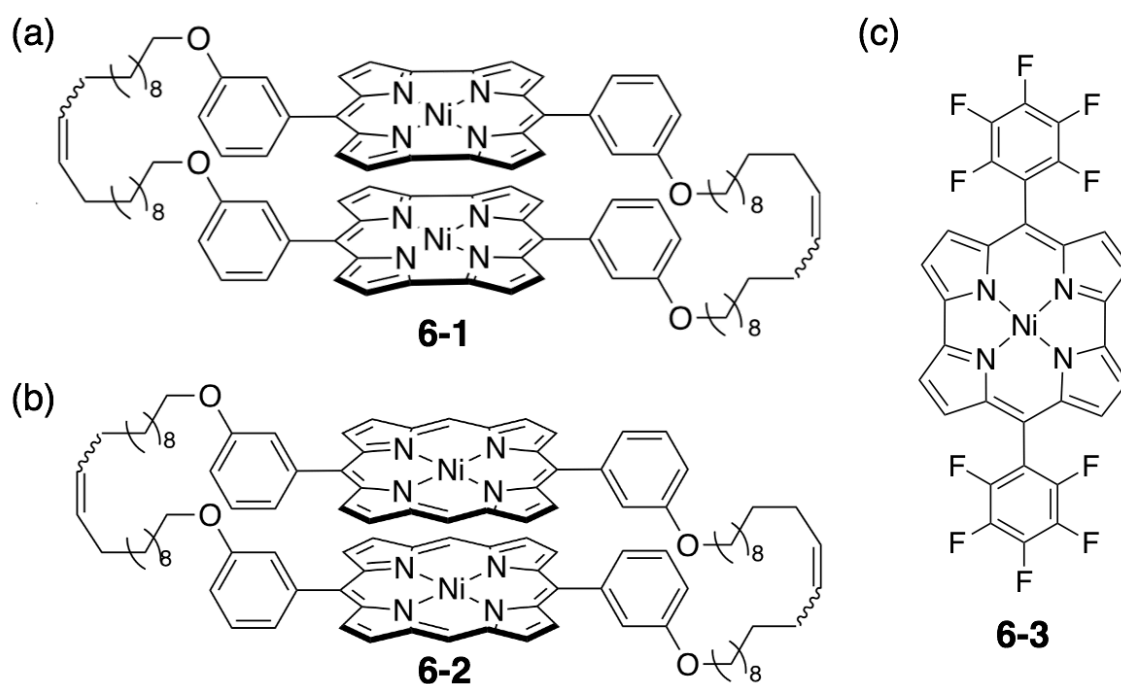
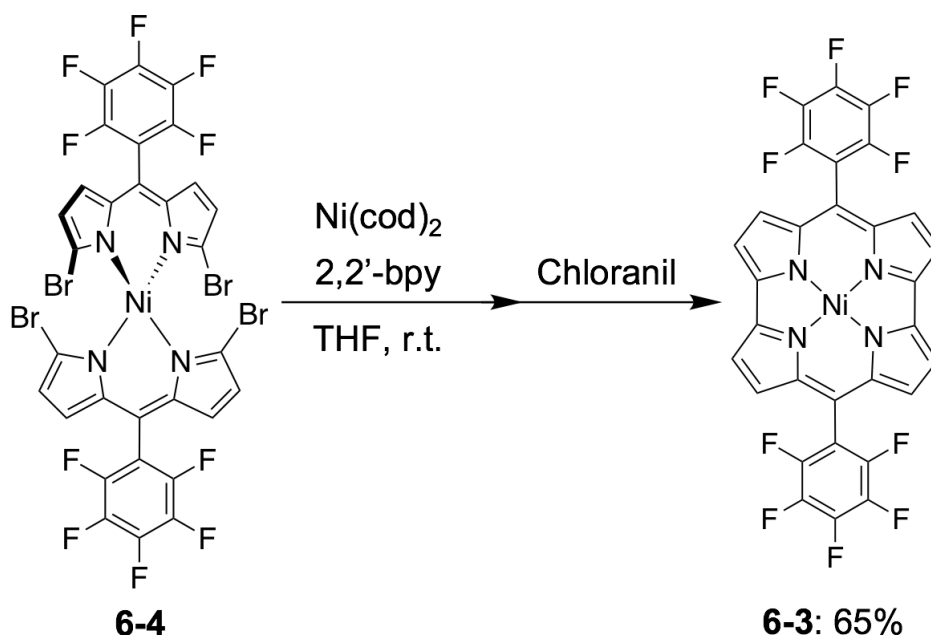


Figure 6-1. Structure of Ni(II) cyclophane type Ni(II) norcorrole **6-1** and Ni(II) porphyrin **6-2**, Ni(II) *meso*-di(pentafluorophenyl)norcorrole **6-3**.

Against this background, the author focused on the introduction of electron-withdrawing groups to norcorroles. In general, the introduction of electron-withdrawing groups (F, CN, and NO₂) for π -systems promote π - π stacking formation due to the reduction of the π -electron repulsions.⁴ In Chapter 6, the author describes the introduction of C₆F₅ groups⁵ into Ni(II) norcorrole at *meso*-positions **6-3** to form close distance π - π stacking without linkers.

6-2. Synthesis of Ni(II) *meso*-di(pentafluorophenyl)norcorrole

As mentioned in Chapter 1, norcorroles with electron-withdrawing groups at *meso*-positions could not be obtained because of their inherent instability.⁷ In Chapter 5, the author reported that the norcorrole radical anion shows high stability due to its deep-lying LUMO and effective delocalized spin over the norcorrole π -system. According to these results, the author speculates that in the synthesis of Ni(II) norcorrole, after the reductive coupling reaction of the dipyrine precursor, the radical anion of Ni(II) norcorrole should be formed by one-electron reduction of neutral Ni(II) norcorrole by excess Ni(0) species in the reaction solution. This situation should be particularly the case for norcorroles with electron-withdrawing groups at *meso*-positions. Then, the author expected to convert radical anion species to norcorroles with an oxidant before the work-up process. Chloranil was selected as the oxidant for this purpose because it did not react with norcorroles, as shown in Chapter 4. In fact, reductive coupling of **6-4** with Ni(cod)₂ followed by chloranil oxidation provided Ni(II) *meso*-di(pentafluorophenyl)norcorrole **6-3** in 65% yield (Scheme 6-1).⁸



Scheme 6-1. Synthesis of Ni(II) *meso*-di(pentafluorophenyl)norcorrole **6-3**.

6-3. Structural analysis

The structure of Ni(II) *meso*-di(pentafluorophenyl)norcorrole **6-3** was unambiguously elucidated by single-crystal X-ray structure analysis (Figure 6-2). The two norcorrole skeletons were stacking closely. The interplanar distance was 3.27 Å, which is shorter than the sum of van der Waals radii of sp^2 -hybridized carbon atoms. Notably, the norcorroles were completely stacked face-to-face π - π stacking. This orientation is similar to one of the polymorphs in the cyclophane type Ni(II) norcorrole linked by two flexible alkyl chains (See Chapter 1: Figure 1-12c). On the other hand, *meso*-diphenylnorcorrole exhibited twisted stacking. The introduction of electron-withdrawing groups could promote the formation of face-to-face π - π stacking.^{2a}

In the stacking structure of **6-3**, the harmonic oscillator model of aromaticity (HOMA)³ value is 0.78, which is distinctly larger than that of the Ni(II) *meso*-dimesitylnorcorrole (0.43)⁶, and comparable to that of the face-to-face stacking

conformation of cyclophane type Ni(II) norcorrole **6-1** (0.69)^{2c} and Ni(II) porphyrin **6-2** (0.77)^{2c}. These results implies that **6-3** exhibits three-dimensional aromaticity in the π - π stacking structure.

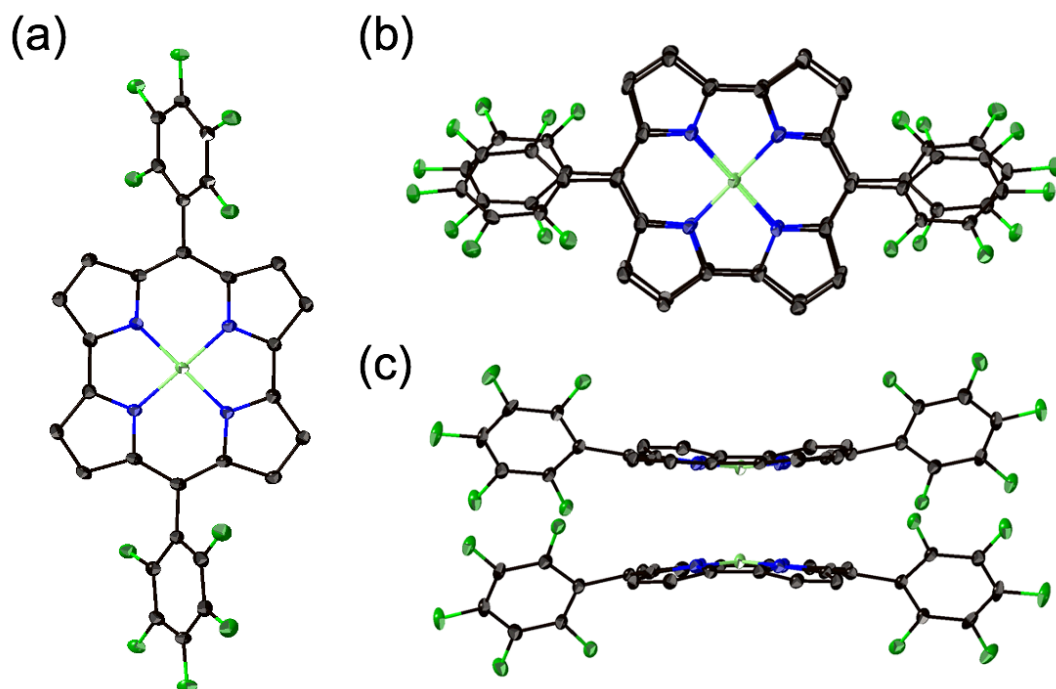


Figure 6-2. X-ray crystal structure of **6-3**. (a) Top and (b) side view of **6-3**. Thermal ellipsoids are drawn at the 50% probability level. All hydrogen atoms are omitted for clarity.

6-4. Electronic structure

The electronic structure was evaluated using DFT calculations at the B3LYP/6-31G(d)+SDD level of theory (Figures 6-3), which suggested that orbitals of norcorrole units interact each other through space in HOMO and HOMO-1. To evaluate the aromaticity of **6-3**, NICS(0) values are calculated at all rings. In the monomer structure **6-3**, positive values from 4.81 to -45.41 ppm for all rings were obtained (Figure 6-4). On the other hand, the dimer structure **6-3**, negative values from -7.81 to -32.38 ppm for all rings were obtained (Figure 6-4). These results indicate that the dimeric structure **6-3** exhibits three-dimensional aromaticity.²

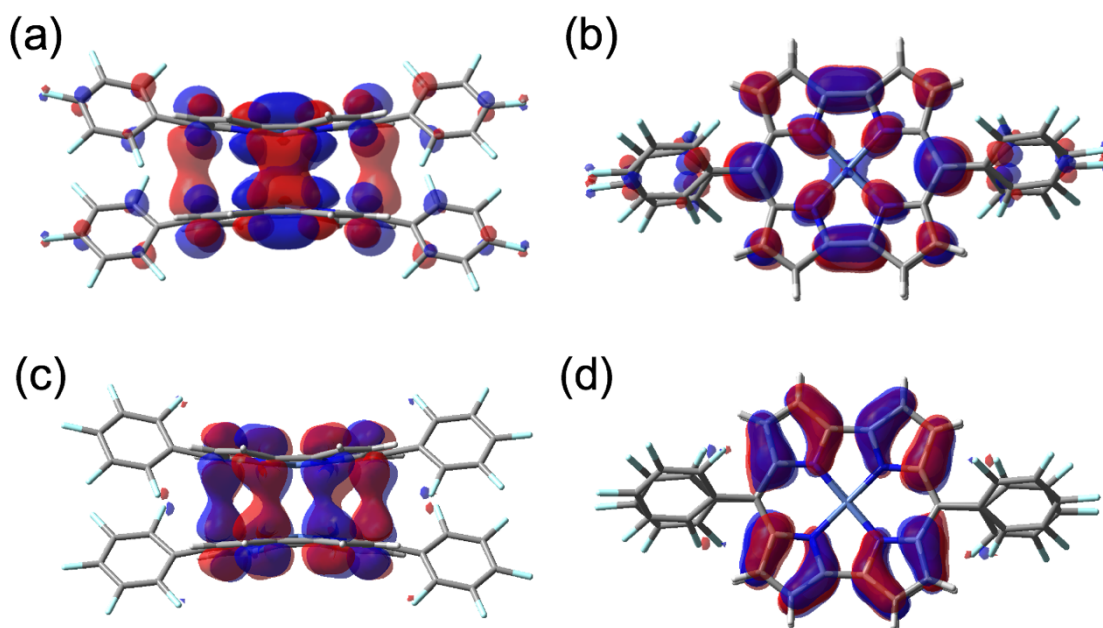


Figure 6-3. Frontier orbital distribution of HOMO (a: side, b: top view) and HOMO-1 (c: side, d: top view) of **6-3**. Calculations were conducted at the B3LYP/6-31G(d)+SDD level of theory.

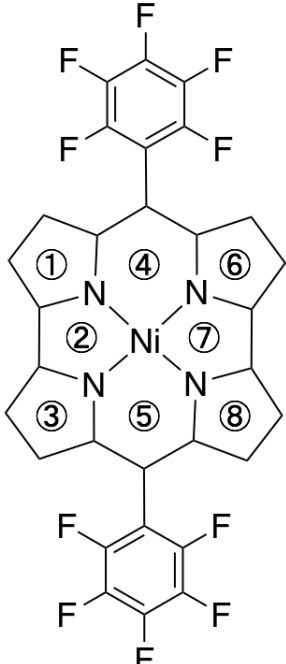
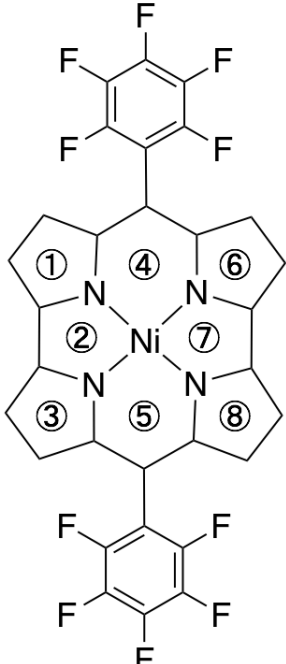
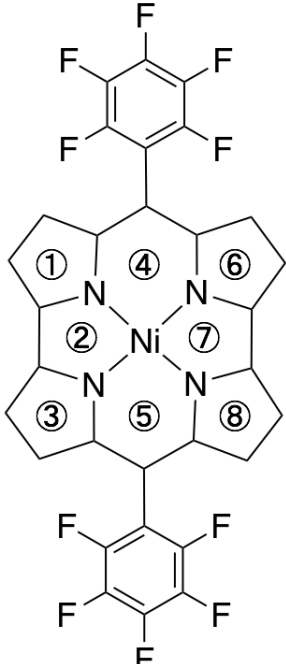
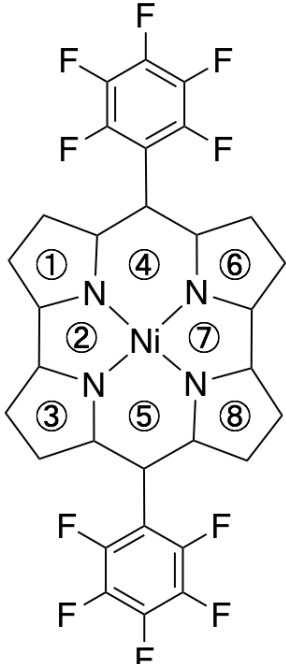
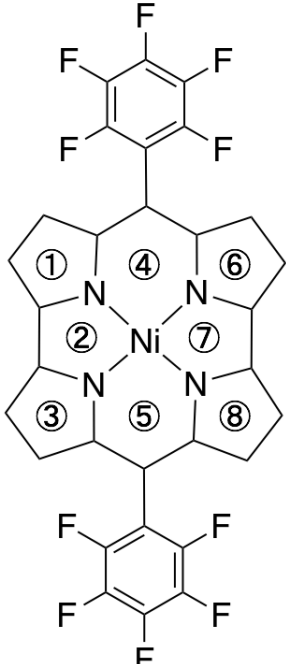
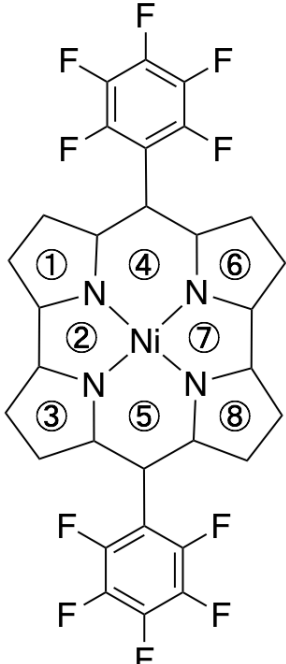
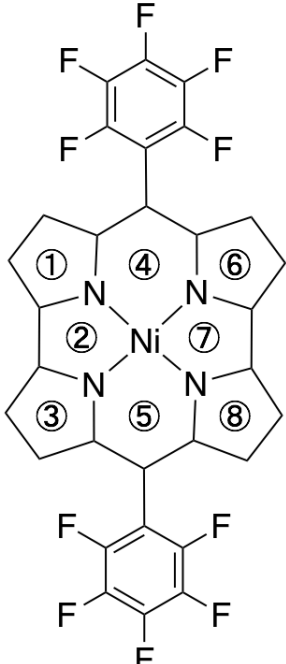
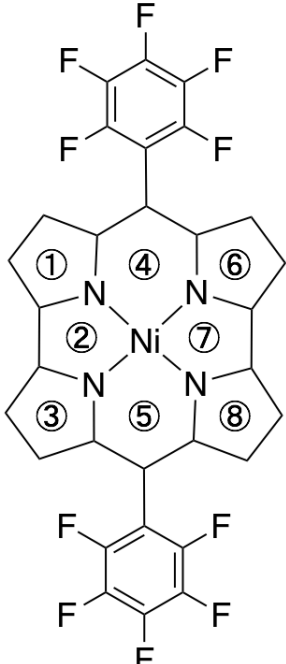
	NICS(0) [ppm] monomer	NICS(0) [ppm] dimer
	4.81	-7.81
	44.68	-32.38
	4.81	-7.80
	45.41	-27.07
	45.41	-27.15
	4.81	-9.78
	44.68	-31.40
	4.81	-9.29

Figure 6-4. NICS(0) values of monomer and dimer structure **6-3**. Calculations were carried out at the B3LYP/6-31G(d)+SDD level of theory.

6-5. Summary of Chapter 6

In summary, the synthesis of Ni(II) *meso*-di(pentafluorophenyl)norcorrole **6-3** was succeeded. The structure of **6-3** was elucidated by X-ray structure analysis, which revealed the face-to-face stacking dimer conformation. In addition, the π - π stacking distance was 3.27 Å. The DFT calculations elucidated the dimer structure of **6-3** exhibited aromaticity. This result shows that the introduction of electron-withdrawing groups into Ni(II) norcorroles enables the control of the stacking orientation without the linkers. This approach should be helpful for the development of high-order structures of norcorroles based on antiaromatic interactions.²

6-6. References

- (a) Corminboeuf, C.; von Ragué Schleyer, P.; Warner, P. *Org. Lett.* **2007**, *9*, 3263.
 - (b) Bean, D. E.; Fowler, P. W. *Org. Lett.* **2008**, *10*, 5573.
- (a) Nozawa, R.; Tanaka, H.; Cha, W.-Y.; Hong, Y.; Hisaki, I.; Shimizu, S.; Shin, J.-Y.; Kowalczyk, T.; Irle, S.; Kim, D.; Shinokubo, H. *Nat. Commun.* **2016**, *7*, 13620.
 - (b) Nozawa, R.; Kim, J.; Oh, J.; Lamping, A.; Wang, Y.; Shimizu, S.; Hisaki, I.; Kowalczyk, T.; Fliegl, H.; Kim, D.; Shinokubo, H. *Nat. Commun.* **2019**, *10*, 3576.
 - (c) Kawashima, H.; Ukai, S.; Nozawa, R.; Fukui, N.; Fitzsimmons, G.; Kowalczyk, T.; Fliegl, H.; Shinokubo, H. *J. Am. Chem. Soc.* **2021**, *143*, 10676.
- The mean plane was defined by the 22 core atoms consisting of meso-carbons and four pyrrole units.
- (a) Hunter, C. A.; Sanders, J. K. M. *J. Am. Chem. Soc.* **1990**, *112*, 5525. (b) Cozzi, F.; Cinquini, M.; Annuziata, R.; Siegel, J. S. *J. Am. Chem. Soc.* **1993**, *115*, 5330. (c) Janiak, C. *J. Chem. Soc., Dalton Trans.* **2000**, 3885.

Chapter 6

- 5 (a) Reichenbacher, K.; Süss, H. I.; Hulliger, J. *Chem. Soc. Rev.* **2005**, *34*, 22. (b) Berger, R.; Resnati, G.; Metrangolo, P.; Weber, E.; Hulliger, J. *Chem. Soc. Rev.* **2011**, *40*, 3496.
- 6 Shin, J.-Y.; Yamada, T.; Yoshikawa, H.; Awaga, K.; Shinokubo, H. *Angew. Chem. Int. Ed.* **2014**, *53*, 3096.
- 7 Yoshida, T.; Sakamaki, D.; Seki, S.; Shinokubo, H. *Chem. Commun.* **2017**, *53*, 1112.
- 8 Without oxidative treatment of the reaction mixture with chloranil, the formation of **6-3** was not confirmed by TLC analysis.

Chapter 7

Summary of this thesis

This thesis demonstrated that antiaromatic norcorroles are handled without using bulky *meso*-substituent for kinetic protection. This insight allowed the integration of norcorrole by various methods. In addition, the aggregates exhibited reversible self-assembly, charge transport functions, and electrical conductivity.

Chapter 2 described that Ni(II) norcorrole can be stably handled without the bulky protection at the *meso*-position. The single-crystal X-ray analysis revealed that the methyl groups substituted norcorrole at the *meso*-position form a one-dimensional stacking structure in the solid-state and exhibited n-type charge transport properties.

Chapter 3 disclosed the formation of a one-dimensional supramolecular polymer from an antiaromatic Ni(II) norcorrole constructed by hydrogen bonding. The polymer exhibited high charge transport properties than that of supramolecular polymer constituted of aromatic Zn(II) porphyrins.

Chapter 4 discussed the formation of CT complexes of Ni(II) norcorrole with various acceptors. X-ray crystal analysis of the CT complex with TCNE revealed the formation of a conduction pathway between the Ni(II) norcorrole units through a partial overlap of the π -planes.

Chapter 5 described the reduction of Ni(II) *meso*-dimesitylnorcorrole to its isolable radical anion with cobaltocene ($\text{Co}^{\text{II}}\text{Cp}_2$). X-ray crystal analysis of the radical anion revealed that the structural change by one-electron reduction is marginal. DFT

calculations elucidated that the reorganization energy of Ni(II) norcorrole upon one-electron injection is smaller than those of Zn(II) porphyrin and C₆₀ fullerenes.

Chapter 6 disclosed the introduction of pentafluorophenyl groups to Ni(II) norcorrole at *meso*-positions. X-ray analysis of the C₆F₅-substituted norcorrole revealed that the structure of closely stacked face-to-face dimer formed without linkers.

The research on materials based on aromatic compounds has been developed over half a century because of their high stability and flexible structure modification. On the other hand, the research on antiaromatic compounds has been limited due to their instability despite their excellent potentials for electronic devices. The author believes that the present study on the integration of norcorroles would inspire the prospects of antiaromatic molecules-based materials.

Chapter 7

Experimental Section

Contents

E-1. Instruction and materials	125
E-2. Charge transfer properties (Chapter 2).....	126
E-3. Synthetic procedures and compounds data	127
E-4. Crystallographic data	140
E-5. References	145

E-1. Instruction and materials

¹H NMR (500 MHz), ¹³C NMR (126 MHz), and ¹⁹F NMR (471 MHz) spectra were recorded on a Bruker AVANCE III HD spectrometer. Chemical shifts were reported as the delta scale in ppm relative to CHCl₃ ($\delta = 7.26$ ppm) for ¹H NMR and CDCl₃ ($\delta = 77.16$ ppm) for ¹³C NMR. UV/vis/NIR absorption spectra were recorded on a Shimadzu UV-2550 or JASCO V 670 spectrometer. High-resolution atmospheric pressure chemical ionization time-of-flight (APCI-TOF) and electrospray ionization time-of-flight (ESI-TOF) mass spectra were taken on a Bruker microTOF instrument using a positive ionization mode. High-resolution matrix assisted laser desorption and ionization time-of-flight (MALDI-TOF) mass spectra were taken on a Bruker autoflex max using a negative ionization mode. X-ray diffraction data were taken on a Rigaku CCD diffractometer (Rigaku VariMax Saturn) with Varimax Mo optics using graphite monochromated Mo-K α radiation ($\lambda = 0.71073$ Å). The structures were solved using a direct method (SHELXT) and refined by a full-matrix least-squares method on F^2 for all reflections using the programs of SHELXL-2014. All nonhydrogen atoms were refined with anisotropic displacement parameters. The hydrogen atoms were placed in idealized

positions and refined as riding models with the relative isotropic displacement parameters. Crystallographic data have been deposited with the Cambridge Crystallographic Data Centre as a supplementary publication. Transmission electron microscopy (TEM) was performed with a JEM-1400EM (JEOL) using an acceleration voltage of 80 kV. Fourier transform infrared (FT-IR) spectroscopic analysis was performed on a JASCO FT/IR-4200 spectrometer. All calculations were carried out using the *Gaussian 09* or *16* programs.^{1,2} Calculations were performed with Becke's three-parameter hybrid exchange functional and the Lee–Yang–Parr correlation functional (B3LYP)^{3,4} or hybrid exchange–correlation functional using the Coulomb-attenuating method (CAM-B3LYP)⁵ and a basis set consisting of SDD⁶ for Ni. Unless otherwise noted, materials obtained from commercial suppliers were used without further purification. 5-Methyldipyrromethane,⁷ 3,4,5-tridodecyloxybenzoic,⁸ 5-(4-hydroxyphenyl)dipyrromethane⁹ and Ni(II) *meso*-pentafluorophenyl- α,α' -dibromodipyrin¹⁰ were synthesized according to the literature. Unless otherwise noted, materials obtained from commercial suppliers were used without further purification.

E-2. Charge transfer properties (Chapter 2)

E-2-1. TRMC Measurements

Transient photoconductivity was measured by an FP-TRMC setup. A resonant cavity with $Q \sim 2500$ was used to obtain a high degree of sensitivity in the conductivity measurement. Probing microwave frequency and power were set at ~ 9.1 GHz and 3.0 mW, respectively, such that the electric field of the microwave was sufficiently small not to disturb the translational motion of charge carriers. The observed value of photoconductivity converted to the product of the quantum yield ϕ and the sum of charge-

carrier mobilities $\Sigma\mu$ by $\varphi\Sigma\mu = \Delta\sigma (eI_0F_{\text{light}})^{-1}$, where e , I_0 , F_{light} and $\Delta\sigma$ are the unit charge of a single electron, incident photon density of excitation laser (photons per m^2), a correction factor (m^{-1}) and transient photoconductivity, respectively. The sample was set at the point of electric field maximum in a resonant cavity. FP-TRMC experiments were performed at room temperature under O_2 or Ar saturated conditions by continuous flowing > 10 min. The measurements of all the samples were performed for polycrystalline samples. These samples were fixed on a quartz substrate by poly(vinyl alcohol) binders.

E-2-2. Calculation of Intermolecular Charge Transfer Integrals

The values of intermolecular charge transfer integrals were calculated with the corresponding dimer structures in the crystal packing of each Ni(II) norcorrole complex with the PW91/LANL2DZ level using CATNIP in conjunction with the Gaussian 16 package.^{2,11} The non-hybrid PW91¹² functional was used as the basis sets for transfer integral calculation, which has been known to give better estimates of transfer integral and reduce the calculation cost.¹³

E-3. Synthetic procedures and compounds data

Ni(II) *meso*-diphenylnorcorrole 2-3

Ni(II) *meso*-diphenyl- α,α' -dibromodipyrin (352 mg, 0.40 mmol), bis(1,5-cyclooctadiene)nickel (275.5 mg, 0.40 mmol), and 2,2'-bipyridyl (155.8 mg, 0.4 mmol) were dissolved in degassed and dehydrated THF (80 mL) in an argon-filled glovebox. The solution was stirred for 3 h at room temperature under argon. The reaction mixture was filtered through a short pad of Celite[®] (CHCl_3 as eluent). The solvent was removed

in vacuo. The residue was washed with acetone, which afforded **2-3** in 54% (106 mg, 0.215 mmol) as a green solid.

The compound data was consistent with the reported ones.¹⁴ ¹H NMR (CDCl₃, 25 °C): δ 6.89 (t, J = 7.5 Hz, 2H, Ph), 6.68 (t, J = 7.5 Hz, 4H, Ph), 6.00 (d, J = 7.5 Hz, 4H, Ph), 2.20 (d, J = 4.0 Hz, 4H, β -H), 1.84 (d, J = 4.0 Hz, 4H, β -H) ppm; ¹³C NMR (CDCl₃, 25 °C): δ 167.8, 158.6, 147.4, 131.8, 131.0, 131.0, 127.8, 120.3, 114.7 ppm.

Ni(II) meso-methyl- α,α' -dibromodipyrin 2-12

A two-necked flask containing 5-methyldipyrromethane **2-11** (2.20 g, 13.7 mmol) was evacuated and then refilled with N₂. To the flask, dry THF (100 mL) was added. The solution was cooled to -78 °C. *N*-Bromosuccinimide (NBS, 4.89 g, 27.4 mmol) was added to the solution in three portions with a 10 min interval. The mixture was stirred for 1 h. To the mixture, 2,3-dichloro-5,6-dicyano-1,4-benzoquinone (DDQ, 3.23 g, 15.1 mmol) was added. After stirring at -78 °C for 1 h, Ni(OAc)₂·4H₂O (1.21 g, 6.85 mmol) was added to the solution and warmed to room temperature. After stirring at room temperature for 1 h, the reaction mixture was filtered through a short pad of alumina column (CH₂Cl₂ as eluent). The solvent was removed under reduced pressure. The residue was purified by silica-gel column chromatography (CH₂Cl₂/hexane = 1/4 as eluent), which afforded **2-13** in 10% (532 mg, 7.73 mmol) as a red powder.

HR-MS (ESI-MS): m/z = 684.7402, calcd for (C₂₀H₁₄N₄Br₄Ni)⁺ = 684.7378 [M + H]⁺. The ¹H NMR spectrum was too broad to be assigned because of the paramagnetic nature of **2-13**.

Ni(II) meso-dimethylnorcorrole 2-4

Dipyrin complex **2-13** (50 mg, 0.073 mmol), bis(1,5-cyclooctadiene)nickel (20

mg, 0.18 mmol), and 2,2'-bipyridyl (28 mg, 0.18 mmol) were dissolved in dehydrated THF (13 mL) in an argon-filled glovebox. The solution was stirred for 4 h at room temperature under argon. The reaction mixture was filtered through a short pad of Celite® (CHCl₃ as eluent). The solvent was removed *in vacuo*. The residue was purified by silica-gel column chromatography (CH₂Cl₂/hexane = 1/4 as eluent), and the collected yellow-brown band was concentrated, which afforded **2-4** in 26% (7.0 mg, 19 μmol) as a black powder.

¹H NMR (CDCl₃, 25 °C): δ 3.11 (d, *J* = 4.0 Hz, 4H, β-H), 2.42 (d, *J* = 4.0 Hz, 4H, β-H), -0.96 (s, 6H, methyl) ppm; λ_{max} (ε(M⁻¹ cm⁻¹)) 422 (34,000), 504 (17,000) nm; HR-MS (ESI-MS): *m/z* = 368.0555, calcd for (C₂₀H₁₄N₄Ni)⁺ = 368.0566 [M]⁺. The ¹³C NMR spectrum was not obtained because of the low solubility of **2-4**.

***N*-(3-Bromopropyl)-3,4,5-tridodecyloxybenzamide 3-6**

3,4,5-Tri(dodecyloxy)benzoic acid (1.5 g, 1.9 mmol) was dissolved in CH₂Cl₂ (20 mL). To the solution, 1-(3-dimethylaminopropyl)-3-ethylcarbodiimide hydrochloride (EDCI•HCl, 505 mg, 2.64 mmol) and 4-dimethylaminopyridine (DMAP, 30 mg, 0.24 mmol) were added. Then 3-bromopropylamine hydrochloride (482 mg, 2.20 mmol) was added, and the mixture was stirred for 30 min at room temperature. After the reaction was completed, the reaction mixture was washed with water. The organic layer was dried over Na₂SO₄ and filtered and concentrated. The obtained crude product was purified by silica-gel column chromatography (hexane/EtOAc = 7/1, R_f = 0.50) to obtain **3-6** (769 mg, 51%) as a white solid.

¹H NMR (500 MHz, CDCl₃, 298 K): δ = 6.94 (s, 2H), 6.21 (t, *J* = 5.9 Hz, 1H), 3.95–4.05 (m, 6H), 3.60 (q, *J* = 6.5 Hz, 2H), 3.50 (t, *J* = 6.6 Hz, 2H), 2.21 (quin, *J* = 6.5 Hz, 2H), 1.77–1.85 (m, 4H), 1.70–1.76 (m, 2H), 1.42–1.51 (m, 6H), 1.20–1.40 (m, 48H), 0.88

(t, $J = 8.8$ Hz, 9H) ppm; ^{13}C NMR (126 MHz, CDCl_3 , 298 K): $\delta = 167.6, 153.1, 141.3, 129.3, 105.7, 73.5, 69.4, 38.8, 32.2, 31.2, 31.1, 30.3, 29.8, 29.7, 29.6, 29.4, 26.1, 22.7, 14.1$ ppm; HR-MS (APCI): $[\text{M}+\text{H}]^+$ Calcd for $\text{C}_{46}\text{H}_{85}^{79}\text{BrNO}_4$ 794.5656; Found 794.5566.

***N*-(3-Bromopropyl)-3,4,5-tridodecyloxybenzoate 3-7**

3,4,5-Tri(dodecyloxy)benzoic acid (200 mg, 0.296 mmol) was dissolved in CH_2Cl_2 (4 mL). To the solution, 1-(3-dimethylaminopropyl)-3-ethylcarbodiimide hydrochloride (EDCI \cdot HCl, 68 mg, 0.36 mmol) and 4-dimethylaminopyridine (DMAP, 3.6 mg, 0.015 mmol) were added. Then, 3-bromo-1-propanol (50 mg, 0.36 mmol) was added, and the mixture was stirred for 12 h at room temperature. After the reaction was completed, the reaction mixture was washed with water. The organic layer was dried over Na_2SO_4 and filtered and concentrated. The obtained crude product was purified by recrystallization from ($\text{CH}_2\text{Cl}_2/\text{MeOH}$) to obtain **3-7** (150 mg, 63%) as a white solid.

^1H NMR (500 MHz, CDCl_3 , 298 K): $\delta = 7.24$ (s, 2H), 4.44 (t, $J = 6.5$ Hz, 2H), 3.95–4.05 (m, 6H), 3.53 (t, $J = 6.5$ Hz, 2H), 2.32 (q, $J = 6.5$ Hz, 2H), 2.21 (quin, $J = 6.5$ Hz, 2H), 1.77–1.85 (m, 4H), 1.70–1.76 (m, 2H), 1.42–1.51 (m, 6H), 1.20–1.40 (m, 46H), 0.88 (t, $J = 8.8$ Hz, 9H) ppm; ^{13}C NMR (126 MHz, CDCl_3 , 298 K): $\delta = 166.3, 152.9, 142.6, 124.5, 108.1, 73.5, 69.2, 62.8, 31.9, 29.8, 29.6, 29.4, 29.3, 26.1, 22.7, 29.4, 14.1$ ppm; HR-MS (APCI): $[\text{M}]^+$ Calcd for $\text{C}_{46}\text{H}_{83}^{79}\text{BrO}_5$ 794.5418; Found 794.5417.

Amide-functionalized dipyrromethane 3-8a

To a solution of 5-(4-hydroxyphenyl)dipyrromethane **3-5** (100 mg, 0.420 mmol) in THF/DMF (1/4, 100 mL), Cs_2CO_3 (1.37 g, 4.20 mmol) and **3-6** (668 mg, 0.841 mmol) were added. The mixture was stirred for 2.5 h at 50 °C. After the reaction was completed, the reaction mixture was extracted with EtOAc and washed with water. The organic layer

was dried over Na₂SO₄ and filtered and concentrated. The obtained crude product was purified by silica-gel column chromatography (hexane/EtOAc = 2/1, R_f = 0.45) to obtain **3-8a** (344 mg, 86%) as a brown solid.

¹H NMR (500 MHz, CDCl₃, 298 K): δ = 7.95 (br, 2H), 7.12 (d, *J* = 8.6 Hz, 2H), 6.96 (s, 2H), 6.84 (d, *J* = 8.6 Hz, 2H), 6.68 (dd, *J* = 3.2, 2.8 Hz, 2H), 6.50 (t, *J* = 5.4 Hz, 1H), 6.14 (q, *J* = 2.8 Hz, 2H), 5.88–5.92 (m, 2H), 5.42 (s, 1H), 4.05–4.15 (m, 4H), 4.00 (t, *J* = 6.5 Hz, 6H), 3.64 (q, *J* = 6.2 Hz, 2H), 1.70–1.85 (m, 6H), 1.40–1.51 (m, 6H), 1.23–1.37 (m, 48H), 0.89 (t, *J* = 7.1 Hz, 9H) ppm; ¹³C NMR (126 MHz, CDCl₃, 298 K): δ = 167.4, 157.5, 153.1, 141.2, 134.8, 132.7, 129.6, 129.5, 117.2, 114.6, 108.5, 107.1, 105.7, 73.5, .69.4, 66.9, 43.2, 38.4, 31.9, 30.3, 29.8, 29.7, 29.6, 29.4, 26.1, 22.7, 14.1 ppm; HR-MS (APCI): [M]⁺ Calcd for C₆₁H₉₇N₃O₅ 951.7423; Found 951.7427.

Ester-functionalized dipyrromethane 3-8b

To a solution of 5-(4-hydroxyphenyl)dipyrromethane **3-5** (100 mg, 0.420 mmol) in THF/DMF (1/2, 21 mL), Cs₂CO₃ (819 mg, 2.52 mmol) and **3-7** (401 mg, 0.500 mmol) were added. The mixture was stirred for 2 h at 50 °C. After the reaction was completed, the reaction mixture was extracted with EtOAc and washed with water. The organic layer was dried over Na₂SO₄ and filtered and concentrated. The obtained crude product was purified by silica-gel column chromatography (hexane/EtOAc = 4/1, R_f = 0.53) to obtain **3-8b** (330 mg, 83%) as a brown solid.

¹H NMR (500 MHz, CDCl₃, 298 K): δ = 7.94 (br, 2H), 7.25 (s, 2H), 7.11 (d, *J* = 8.5 Hz, 2H), 6.85 (d, *J* = 8.5 Hz, 2H), 6.68 (dd, *J* = 3.2, 2.8 Hz, 2H), 6.16 (q, *J* = 2.8 Hz, 2H), 5.88–5.92 (m, 2H), 5.42 (s, 1H), 4.49 (t, *J* = 6.5 Hz, 2H), 4.10 (t, *J* = 6.5 Hz, 2H), 3.95–4.05 (m, 6H), 2.25 (quin, *J* = 6.2 Hz, 2H), 1.70–1.90 (m, 6H), 1.44–1.55 (m, 6H), 1.23–1.37 (m, 48H), 0.89 (t, *J* = 7.1 Hz, 9H) ppm; ¹³C NMR (126 MHz, CDCl₃, 298 K): δ =

166.4, 157.7, 152.9, 142.5, 134.5, 132.8, 129.4, 124.7, 117.1, 114.5, 108.4, 107.1, 73.6, .69.3, 64.5, 61.9, 43.2, 32.0, 30.4, 30.0, 29.7, 29.6, 29.4, 29.3, 28.9, 26.1, 22.7, 14.1 ppm; HR-MS (APCI): $[M+H]^+$ Calcd for $C_{61}H_{97}N_2O_6$ 953.7341; Found 953.7434.

5-(4-Dodecyloxyphenyl)dipyrromethane 3-8c

To a solution of 5-(4-hydroxyphenyl)dipyrromethane **3-5** (300 mg, 1.26 mmol) in THF/DMF (1/4, 5 mL), CS_2CO_3 (492 mg, 1.50 mmol) and 1-bromododecane (374 mg, 1.50 mmol) was added. The mixture was stirred for 2.5 h at 50 °C. After the reaction was completed, the reaction mixture was extracted with EtOAc and washed with water. The organic layer was dried over Na_2SO_4 and filtered and concentrated. The obtained crude product was purified by recrystallization from ($CH_2Cl_2/MeOH$) to obtain **3-8c** (309 mg, 60%) as a white solid.

1H NMR (500 MHz, $CDCl_3$, 298 K): δ = 9.73 (br, 2H), 7.21 (d, J = 8.4 Hz, 2H), 6.96 (d, J = 8.4 Hz, 2H), 6.77–6.79 (m, 2H), 6.08 (q, J = 2.7 Hz, 2H), 5.81–5.84 (m, 2H), 5.48 (s, 1H), 4.07 (t, J = 6.5 Hz, 2H), 1.82–1.90 (m, 2H), 1.54–1.65 (m, 2H), 1.35–1.51 (m, 16H), 1.00 (t, J = 6.8 Hz, 3H) ppm; ^{13}C NMR (126 MHz, acetone- d_6 , 298 K): δ = 158.2, 134.1, 133.1, 129.4, 117.2, 114.6, 108.4, 107.2, 68.2, 43.2, 32.0, 29.8, 29.7, 29.5, 29.4, 26.2, 22.8, 14.2 ppm; HR-MS (APCI): $[M]^+$ Calcd for $C_{27}H_{38}N_2O$ 406.2979; Found 406.2981.

Amide-functionalized Ni(II) α,α' -dibromodipyrin 3-10a

A two-necked flask containing dipyrromethane **3-8a** (377 mg, 0.350 mmol) was evacuated and then refilled with N_2 . To the flask, dry THF (106 mL) was added. The solution was cooled to -78 °C. *N*-Bromosuccinimide (NBS, 125 mg, 0.700 mmol) was added to the solution in three portions with a 10 min interval. The mixture was stirred for

1 h. To the mixture, 2,3-dichloro-5,6-dicyano-1,4-benzoquinone (DDQ, 87 mg, 0.39 mmol) was added. After stirring at $-78\text{ }^{\circ}\text{C}$ for 1 h, $\text{Ni}(\text{OAc})_2 \cdot 4\text{H}_2\text{O}$ (120 mg, 0.484 mmol) was added to the solution and warmed to room temperature. After stirring at room temperature for 1 h, the reaction mixture was filtered through a short pad of alumina column (CH_2Cl_2 as eluent). The solvent was removed under reduced pressure, and the residue was purified by recrystallization from ($\text{CH}_2\text{Cl}_2/\text{MeOH}$) to afford **3-10a** in 71% (284 mg, 0.125 mmol) as a red powder.

HR-MS (ESI): $[\text{M}+\text{Na}]^+$ Calcd for $\text{C}_{122}\text{H}_{184}^{79}\text{Br}_4\text{N}_6\text{NiO}_{10}\text{Na}$ 2290.0053; Found 2290.0001. The ^1H NMR spectrum was too broad to be assigned because of the paramagnetic nature of **3-10a**.

Ester-functionalized Ni(II) α,α' -dibromodipyrin 3-10b

A two-necked flask containing dipyrromethane **3-8b** (285 mg, 0.300 mmol) was evacuated and then refilled with N_2 . To the flask, dry THF (120 mL) was added. The solution was cooled to $-78\text{ }^{\circ}\text{C}$. *N*-Bromosuccinimide (NBS, 36 mg, 0.20 mmol) was added to the solution in three portions with a 10 min interval. The mixture was stirred for 1 h. To the mixture, 2,3-dichloro-5,6-dicyano-1,4-benzoquinone (DDQ, 74 mg, 0.33 mmol) was added. After stirring at $-78\text{ }^{\circ}\text{C}$ for 1 h, $\text{Ni}(\text{OAc})_2 \cdot 4\text{H}_2\text{O}$ (22 mg, 0.090 mmol) was added to the solution and warmed to room temperature. After stirred at room temperature for 1 h, the reaction mixture was filtered through a short pad of alumina column (CH_2Cl_2 as eluent). The solvent was removed under reduced pressure and the residue purified by silica-gel column chromatography (hexane/EtOAc = 7/1, R_f = 0.60) to obtain **3-10b** (200 mg, 64%) as a viscous red liquid.

HR-MS (ESI): $[\text{M}+\text{Na}]^+$ Calcd for $\text{C}_{122}\text{H}_{182}^{79}\text{Br}_4\text{N}_4\text{NiO}_{12}\text{Na}$ 2291.9733; Found 2291.9752. The ^1H NMR spectrum was too broad to be assigned because of the

paramagnetic nature of **3-10b**.

Ni(II) *meso*-(4-dodecyloxyphenyl)- α,α' -dibromodipyrin **3-10c**

A two-necked flask containing dipyrromethane **3-8c** (263 mg, 0.648 mmol) was evacuated and then refilled with N₂. To the flask, dry THF (20 mL) was added. The solution was cooled to -78 °C. *N*-Bromosuccinimide (NBS, 125 mg, 0.700 mmol) was added to the solution in three portions with a 10 min interval. The mixture was stirred for 1 h. To the mixture, 2,3-dichloro-5,6-dicyano-1,4-benzoquinone (DDQ, 162 mg, 0.713 mmol) was added. After stirring at -78 °C for 1 h, Ni(OAc)₂·4H₂O (55 mg, 0.44 mmol) was added to the solution and warmed to room temperature. After stirring at room temperature for 1 h, the reaction mixture was filtered through a short pad of alumina column (CH₂Cl₂ as eluent). The solvent was removed under reduced pressure, and the residue was purified by recrystallization from (CH₂Cl₂/MeOH) to afford **3-10c** in 98% (250 mg, 0.125 mmol) as a red powder.

HR-MS (APCI): [M+H]⁺ Calcd for C₅₄H₆₇⁷⁹Br₄N₄NiO₂ 1177.1345; Found 1177.1189. The ¹H NMR spectrum was too broad to be assigned because of the paramagnetic nature of **3-10c**.

Amide-functionalized Ni(II) norcorrole **3-2**

Dipyrin complex **3-10a** (283 mg, 0.125 mmol), bis(1,5-cyclooctadiene)nickel (85.5 mg, 0.311 mmol), and 2,2'-bipyridyl (48.6 mg, 0.311 mmol) were dissolved in dehydrated THF (50 mL) in an argon-filled flask. The solution was stirred for 4 h at room temperature under argon. The reaction mixture was filtered through a short pad of Celite[®] (CHCl₃ as eluent). The solvent was removed *in vacuo*. The residue was purified with column chromatography using amino-functionalized silica-gel (hexane/CHCl₃ = 2/3 as eluent),

and the collected yellow-brown band was concentrated to afford **3-2** in 22% (53 mg, 27 μmol) as a green powder.

^1H NMR (CDCl_3 , 298 K): δ = 6.82 (s, 4H), 6.15–6.25 (m, 6H), 6.03 (d, J = 8.5 Hz, 4H), 3.96 (t, J = 6.6 Hz, 4H), 3.91 (t, J = 6.4 Hz, 8H), 3.80 (t, J = 5.6 Hz, 4H) 3.46 (q, J = 6.2 Hz, 4H), 2.43 (d, J = 4.2 Hz, 4H), 2.06 (d, J = 4.2 Hz, 4H), 1.91 (t, J = 6.2 Hz, 4H), 1.75–1.85 (m, 12H), 1.20–1.40 (m, 108H), 0.80–0.95 (m, 18H) ppm; ^{13}C NMR (126 MHz, CDCl_3 , 298 K): δ = 167.3, 166.99, 161.31, 157.98, 153.06, 146.31, 141.23, 130.58, 129.38, 124.12, 114.25, 113.00, 105.62, 73.50, 69.40, 66.47, 37.89, 32.03, 29.87, 29.77, 29.73, 29.61, 29.49, 29.40, 26.14, 22.76, 14.16 ppm; λ_{max} (ϵ ($\text{M}^{-1} \text{cm}^{-1}$)) = 425 (41,000), 492 (50,000) nm; MALDI-TOF-MS: $[\text{M}]^+$ Calcd for $\text{C}_{122}\text{H}_{184}\text{N}_6\text{NiO}_{10}$ 1951.3422; Found 1951.2585.

Ester-functionalized Ni(II) norcorrole **3-3**

Dipyrin complex **3-10b** (200 mg, 0.0880 mmol), bis(1,5-cyclooctadiene)nickel (61 mg, 0.022 mmol), and 2,2'-bipyridyl (34 mg, 0.022 mmol) were dissolved in dehydrated THF (35 mL) in an argon-filled flask. The solution was stirred for 2 h at room temperature under argon. The reaction mixture was filtered through a short pad of Celite[®] (CH_2Cl_2 as eluent). The solvent was removed *in vacuo*. The residue was purified with silica-gel column chromatography (hexane/EtOAc = 7/1, R_f = 0.33) and the collected yellow-brown band was concentrated to afforded **3-3** in 58% (100 mg, 0.0512 mmol) as a green solid.

^1H NMR (CDCl_3 , 298 K): δ = 7.12 (s, 4H), 6.19 (d, J = 8.9 Hz, 4H), 6.03 (d, J = 8.9 Hz, 4H), 4.30 (t, J = 6.3 Hz, 4H), 3.91 (t, J = 6.4 Hz, 8H), 3.98 (t, J = 6.5 Hz, 4H) 3.81 (t, J = 6.3 Hz, 4H), 2.52 (d, J = 4.2 Hz, 4H), 2.12 (d, J = 4.2 Hz, 4H), 1.70–1.85 (m, 16H), 1.20–1.40 (m, 108H), 0.80–0.95 (m, 18H) ppm; ^{13}C NMR (126 MHz, CDCl_3 , 298

K): $\delta = 166.7, 166.25, 161.52, 157.95, 152.78, 146.12, 142.54, 130.58, 124.51, 123.98, 122.85, 114.20, 112.98, 73.51, 69.21, 32.00, 30.32, 29.82, 29.76, 29.75, 29.72, 29.48, 29.46, 29.41, 29.32, 28.50, 26.13, 22.75, 14.16$ ppm; $\lambda_{\max} (\epsilon (\text{M}^{-1} \text{cm}^{-1})) = 425 (41,000), 492 (50,000)$ nm; MALDI-TOF-MS: $[\text{M}]^+$ Calcd for $\text{C}_{122}\text{H}_{182}\text{N}_4\text{NiO}_{12}$ 1955.3102; Found 1953.2107

Ni(II) *meso*-di(4-dodecyloxyphenyl)norcorrole 3-4

Dipyrrin complex **3-10c** (250 mg, 0.212 mmol), bis(1,5-cyclooctadiene)nickel (146 mg, 0.53 mmol), and 2,2'-bipyridyl (82 mg, 0.53 mmol) were dissolved in dehydrated THF (85 mL) in an argon-filled flask. The solution was stirred for 4 h at room temperature under argon. The reaction mixture was filtered through a short pad of Celite[®] (CHCl_3 as eluent). The solvent was removed *in vacuo*. The residue was purified by silica-gel column chromatography (hexane/ $\text{CH}_2\text{Cl}_2 = 4/1$ as eluent), and the collected yellow-brown band was concentrated. The crude product was purified by recrystallization from CHCl_3 to afford **3-4** in 11% (21 mg, 24 μmol) as green needle crystals.

^1H NMR (CDCl_3 , 298 K): $\delta = 6.18$ (d, $J = 9.0$ Hz, 4H), 6.04 (d, $J = 9.0$ Hz, 4H), 3.64 (t, $J = 6.4$ Hz, 4H), 2.51 (d, $J = 4.0$ Hz, 4H), 2.11 (d, $J = 4.0$ Hz, 4H), 1.15–1.30 (m, 40H), 0.86 (t, $J = 6.9$ Hz, 6H) ppm; ^{13}C NMR (126 MHz, $\text{CDCl}_3/\text{CS}_2 = 1/3$, 298 K): $\delta = 166.96, 162.15, 158.42, 146.17, 130.61, 123.65, 122.62, 114.23, 112.98, 67.83, 32.33, 30.16, 30.05, 29.99, 29.94, 29.71, 29.27, 26.30, 23.27, 14.59$ ppm; $\lambda_{\max} (\epsilon (\text{M}^{-1} \text{cm}^{-1})) = 423 (43,000), 515 (49,000)$ nm; MALDI-TOF-MS: $[\text{M}]^+$ Calcd for $\text{C}_{54}\text{H}_{66}\text{N}_4\text{NiO}_2$ 860.4534; Found 860.4779. Single crystals were obtained by vapor diffusion of hexane into a chloroform solution of **3-4**. Crystallographic data: $\text{C}_{54}\text{H}_{66}\text{N}_4\text{NiO}_2$, $M_w = 861.81$, triclinic, space group $P\bar{1}$, $a = 7.4541(2)$, $b = 8.9928(2)$, $c = 17.4427(4)$ Å, $\alpha = 89.460(2)$, $\beta = 89.460(2)$, $\gamma = 76.481(2)^\circ$, $V = 1109.85(5)$ Å³, $Z = 1$, $D_{\text{calc}} = 1.289$ g cm⁻³, $T = 93$ K,

$R_1 = 0.0472$ ($I > 2.0 \sigma(I)$), $wR_2 = 0.1296$ (all data), GOF = 1.035, CCDC-2107508.

Amide-functionalized porphyrin **3-12**

A two-necked flask containing dipyrromethane **3-8a** (107 mg, 0.110 mmol) was evacuated and then refilled with N₂. To the flask, trimethyl orthoformate (0.42 mL, 3.9 μmol) and dry CH₂Cl₂ (30 mL) were added. The flask was wrapped in aluminum foil, and the mixture was stirred. A solution of trifluoroacetic acid (0.19 mL, 2.5 mmol) in CH₂Cl₂ (12 mL) was added dropwise over 15 min. The resulting solution was stirred in the dark for 4 h. After the reaction was completed, the reaction mixture was quenched with triethylamine (0.45 mL). Finally, air was bubbled into the solution for 10 min, and the reaction mixture was stirred for 1 h under ambient conditions. The solvent was removed, and the obtained crude product was purified with silica-gel column chromatography (hexane/EtOAc = 1/1) to obtain **3-12** in 12% (25 mg, 13 μmol) as a purple solid.

¹H NMR (CDCl₃, 298 K): δ = 10.29 (s, 2H), 9.38 (d, J = 6.0 Hz, 4H), 9.08 (d, J = 6.0 Hz, 4H), 8.18 (d, J = 11 Hz, 4H), 7.34 (d, J = 11 Hz, 4H), 7.12 (s, 4H), 6.78 (t, J = 6.5 Hz, 2H), 4.43 (t, J = 6.5 Hz, 4H), 4.09 (t, J = 8.2 Hz, 8H), 4.02 (t, J = 8.2 Hz, 4H), 3.86 (q, J = 7.7 Hz, 4H), 2.34 (quin, J = 7.3 Hz, 4H), 1.80–1.90 (m, 8H), 1.75–1.80 (m, 4H), 1.40–1.50 (m, 12H), 1.20–1.40 (m, 96H), 0.80–0.90 (m, 18H), –3.08 (s, 2H) ppm; ¹³C NMR (126 MHz, CDCl₃, 298 K): δ = 167.58, 158.51, 153.24, 147.44, 145.13, 141.28, 135.96, 134.24, 131.60, 130.93, 129.74, 118.59, 113.08, 105.81, 105.25, 73.57, 69.50, 67.33, 38.65, 31.90, 30.37, 29.76, 29.70, 29.61, 29.45, 29.42, 29.33, 29.20, 26.14, 22.68, 14.13 ppm; MALDI-TOF-MS: [M]⁺ Calcd for C₁₂₄H₁₈₈N₆O₁₀ 1922.4460; Found 1922.4546.

Amide-functionalized Zn(II) porphyrin 3-11

Porphyrin **3-12** (25 mg, 13 μmol) and $\text{Zn}(\text{OAc})_2$ (26 mg, 0.14 mmol) were loaded in a round-bottomed flask and dissolved in THF (10 mL). The mixture was heated to reflux and stirred 12 h under argon. The mixture was then allowed to cool to room temperature and the solvent was removed under reduced pressure. The crude product was further purified with silica-gel column chromatography (hexane/EtOAc = 1/1) to obtain **11** in 90% (25 mg, 13 μmol) as a purple solid. ^1H and ^{13}C NMR data were consistent with those reported in the literature.¹⁵

^1H NMR (CDCl_3 , 298 K): δ = 10.27 (s, 2H), 9.41 (d, J = 4.5 Hz, 4H), 9.13 (d, J = 4.5 Hz, 4H), 8.18 (d, J = 8.5 Hz, 4H), 7.32 (d, J = 8.5 Hz, 4H), 6.81 (s, 4H), 6.56 (t, J = 5.0 Hz, 2H), 4.39 (t, J = 5.5 Hz, 4H) 3.95–4.05 (m, 12H), 3.52 (q, J = 5.7 Hz, 4H), 2.21 (quin, J = 6.0 Hz, 4H), 1.76–1.85 (m, 12H), 1.40–1.50 (m, 12H), 1.20–1.40 (m, 96H), 0.80–0.90 (m, 18H) ppm; ^{13}C NMR (126 MHz, CDCl_3 , 298 K): δ = 167.48, 158.28, 153.13, 150.40, 149.45, 141.21, 135.74, 135.60, 132.41, 131.70, 129.48, 119.49, 112.71, 106.19, 105.66, 73.54, 69.46, 67.38, 38.56, 31.92, 31.92, 31.87, 30.34, 29.74, 29.74, 29.72, 29.68, 29.62, 29.58, 29.43, 29.40, 29.38, 29.30, 29.10, 26.12, 22.68, 22.65, 14.10 ppm; MALDI-TOF-MS: $[\text{M}]^+$ Calcd for $\text{C}_{124}\text{H}_{186}\text{N}_6\text{O}_{10}\text{Zn}$ 1983.3516; Found 1983.3535.

Ni(II) norcorrole radical anion 5-5

Ni(II) *meso*-dimesitylnorcorrole (92 mg, 0.16 mmol) and cobaltocene ($\text{Co}^{\text{II}}\text{Cp}_2$) (33 mg, 0.17 mmol) were dissolved in dehydrated CH_2Cl_2 (50 mL) in an argon-filled flask. The solution was stirred for 10 min at room temperature under argon. The precipitate was collected by filtration and washed with CH_2Cl_2 , affording **5-5** (116 mg, 0.15 mmol, 95%) as a green solid. The ^1H NMR spectrum of the product was not detected because of the paramagnetic nature of **5-1**. A peak for the counter cation ($[\text{Co}^{\text{III}}\text{Cp}_2]^+$) was also detected

at $\delta = 5.85$ ppm.¹⁶ The single crystal of **5-5** was obtained by slow evaporation of DMSO under reduced pressure.

Ni(II) meso-di(pentafluorophenyl)norcorrole 6-3

Dipyrrin complex **6-4** (120 mg, 0.121 mmol), bis(1,5-cyclooctadiene)nickel (134 mg, 0.48 mmol), and 2,2'-bipyridyl (75 mg, 0.48 mmol) were dissolved in dehydrated THF (50 mL) in an argon-filled glovebox. The solution was stirred for 4 h at room temperature under argon followed by addition chloranil (148 mg, 0.601 mmol) to the reaction mixture. The reaction mixture was filtered through a short pad of Celite® (CH₂Cl₂ as an eluent). The solvent was removed *in vacuo*. The residue was purified by silica-gel column chromatography (CH₂Cl₂/hexane = 1/4 as an eluent) and the collected yellow-brown band was concentrated, which afforded **6-3** in 65% (53 mg, 79 μ mol) as a black powder.

¹H NMR (CDCl₃, 298 K): δ 3.11 (br, 4H, β -H), 3.83 ppm; ¹⁹F NMR (CDCl₃, 298 K): δ = 129.49 (m, 4F), 148.14 (t, J = 22 Hz, 2F), 154.91 (m, 4F) ppm; HR-MS (ESI-MS): m/z = 671.9917, calcd for (C₃₀H₈F₁₀N₄Ni)⁺ = 671.9937 [M]⁺. The ¹³C NMR spectrum was not obtained because of the low stability of **6-3**.

E-4. Crystallographic data

Chapter 2

	2-9	2-4
empirical formula	C ₅₄ H ₄₀ Br ₈ N ₈ Ni ₂	C ₁₀ H ₇ N ₂ Ni _{0.5}
moiety formula	C ₂₇ H ₂₀ Br ₄ N ₄ Ni	C ₁₀ H ₇ N ₂ Ni _{0.5}
crystal system	monoclinic	monoclinic
space group	<i>C2/c</i> (#15)	<i>I12/a1</i> (#15)
<i>a</i> (Å)	35.7513(7)	19.3223(7)
<i>b</i> (Å)	8.3470(1)	4.6693(1)
<i>c</i> (Å)	36.6094(5)	17.6807(6)
α (°)	90	90
β (°)	95.428(1)	112.336(4)
γ (°)	90	90
<i>V</i> (Å ³)	10875.8(3)	1475.50(9)
<i>Z</i>	8	8
<i>D</i> (g/cm ³)	1.903	1.661
<i>R</i> ₁ (<i>I</i> > 2σ(<i>I</i>))	0.0328	0.0450
<i>wR</i> ₂ (all data)	0.0919	0.1253
GOF	1.046	1.076

Chapter 3

	3-4
empirical formula	C ₅₄ H ₆₆ N ₄ NiO ₂
moiety formula	C ₅₄ H ₆₆ N ₄ NiO ₂
crystal system	triclinic
space group	<i>P</i> -1
<i>a</i> (Å)	7.4541(2)
<i>b</i> (Å)	8.9928(2)
<i>c</i> (Å)	17.4427(4)
α (°)	89.460(2)
β (°)	89.460(2)
γ (°)	76.481(2)
<i>V</i> (Å ³)	1109.85(5)
<i>Z</i>	1
<i>D</i> (g/cm ³)	1.289
<i>R</i> ₁ (<i>I</i> > 2σ(<i>I</i>))	0.0472
<i>wR</i> ₂ (all data)	0.1296
GOF	1.035

Chapter 4

	4-1 · chloranil	4-1 · bromanil	4-1 · fluoranil	4-1 · TCNE
empirical formula	$C_{36}H_{18}Cl_4N_4NiO_2$	$C_{36}H_{18}Br_4N_4NiO_2$	$C_{36}H_{18}F_4N_4NiO_2$	$C_{36}H_{18}N_8Ni$
moiety formula	$C_{30}H_{18}N_4Ni \cdot C_6Cl_4O_2$	$C_{30}H_{18}N_4Ni \cdot C_6Br_4O_2$	$C_{30}H_{18}N_4Ni \cdot C_6F_4O_2$	$C_{30}H_{18}N_4Ni \cdot C_6N_4$
crystal system	trigonal	trigonal	monoclinic	monoclinic
space group	$R3$ (#146)	$R3$ (#146)	$P2_1/c$ (#14)	$C2/c$ (#15)
a (Å)	32.8424(8)	32.9871(5)	11.0999(8)	9.6608(6)
b (Å)	32.8425(8)	32.9871(5)	6.5541(4)	25.9352(16)
c (Å)	7.0973(3)	7.2606(2)	18.9951(11)	11.2626(8)
α (°)	90	90	90	90
β (°)	90	90	101.014(2)	106.689(2)
γ (°)	120	120	90	90
V (Å ³)	6629.7(4)	6842.1(3)	1356.44(15)	2703.0(3)
Z	9	9	2	4
D (g/cm ³)	1.666	2.003	1.648	1.527
R_I ($I > 2\sigma(I)$)	0.0231	0.0307	0.0396	0.0390
wR_2 (all data)	0.0556	0.0851	0.0853	0.0774
GOF	1.041	1.070	1.042	1.059

Chapter 5

	5-5
empirical formula	C ₄₆ H ₄₀ N ₄ NiCo
moiety formula	C ₃₆ H ₃₀ N ₄ Ni · C ₁₀ H ₁₀ Co
crystal system	monoclinic
space group	<i>C2/c</i> (#15)
<i>a</i> (Å)	13.6473(7)
<i>b</i> (Å)	19.0724(7)
<i>c</i> (Å)	14.5929(7)
<i>a</i> (°)	90
<i>b</i> (°)	107.031(5)
<i>g</i> (°)	90
<i>V</i> (Å ³)	3631.8(3)
<i>Z</i>	4
<i>D</i> (g/cm ³)	1.402
<i>R</i> ₁ (<i>I</i> > 2 <i>s</i> (<i>I</i>))	0.0527
<i>wR</i> ₂ (all data)	0.1180
GOF	1.126

Chapter 6

	6-3
empirical formula	C ₆₀ H ₁₆ F ₂₀ N ₈ Ni ₂
moiety formula	C ₆₀ H ₁₆ F ₂₀ N ₈ Ni ₂
crystal system	triclinic
space group	<i>P</i> -1 (#2)
<i>a</i> (Å)	14.6135(5)
<i>b</i> (Å)	10.8506(4)
<i>c</i> (Å)	14.8429(7)
<i>a</i> (°)	90
<i>b</i> (°)	102.385(4)
<i>g</i> (°)	90
<i>V</i> (Å ³)	2298.80(16)
<i>Z</i>	2
<i>D</i> (g/cm ³)	1.945
<i>R</i> ₁ (<i>I</i> > 2 <i>s</i> (<i>I</i>))	0.0485
<i>wR</i> ₂ (all data)	0.1151
GOF	1.018

E-5. References

1. M. J. Frisch, G. W. Trucks, H. B. Schlegel, G. E. Scuseria, M. A. Robb, J. R. Cheeseman, G. Scalmani, V. Barone, B. Mennucci, G. A. Petersson, H. Nakatsuji, M. Caricato, X. Li, H. P. Hratchian, A. F. Izmaylov, J. Bloino, G. Zheng, J. L. Sonnenberg, M. Hada, M. Ehara, K. Toyota, R. Fukuda, J. Hasegawa, M. Ishida, T. Nakajima, Y. Honda, O. Kitao, H. Nakai, T. Vreven, J. A. Montgomery, Jr., J. E. Peralta, F. Ogliaro, M. Bearpark, J. J. Heyd, E. Brothers, K. N. Kudin, V. N. Staroverov, R. Kobayashi, J. Normand, K. Raghavachari, A. Rendell, J. C. Burant, S. S. Iyengar, J. Tomasi, M. Cossi, N. Rega, J. M. Millam, M. Klene, J. E. Knox, J. B. Cross, V. Bakken, C. Adamo, J. Jaramillo, R. Gomperts, R. E. Stratmann, O. Yazyev, A. J. Austin, R. Cammi, C. Pomelli, J. W. Ochterski, R. L. Martin, K. Morokuma, V. G. Zakrzewski, G. A. Voth, P. Salvador, J. J. Dannenberg, S. Dapprich, A. D. Daniels, Ö. Farkas, J. B. Foresman, J. V. Ortiz, J. Cioslowski, D. J. Fox, Gaussian, Inc., Wallingford CT, **2009**.
2. *Gaussian 16*, Revision A.03, M. J. Frisch, G. W. Trucks, H. B. Schlegel, G. E. Scuseria, M. A. Robb, J. R. Cheeseman, G. Scalmani, V. Barone, G. A. Petersson, H. Nakatsuji, X. Li, M. Caricato, A. V. Marenich, J. Bloino, B. G. Janesko, R. Gomperts, B. Mennucci, H. P. Hratchian, J. V. Ortiz, A. F. Izmaylov, J. L. Sonnenberg, D. Williams-Young, F. Ding, F. Lipparini, F. Egidi, J. Goings, B. Peng, A. Petderson, D. Ranasinghe, V. G. Zakrzewski, J. Gao, N. Rega, G. Zheng, W. Liang, M. Hada, M. Ehara, K. Toyota, R. Fukuda, J. Hasegawa, M. Ishida, T. Nakajima, Y. Honda, O. Kitao, H. Nakai, T. Vreven, K. Throssell, J. A. Montgomery, Jr., J. E. Peralta, F. Ogliaro, M. J. Bearpark, J. J. Heyd, E. N. Brothers, K. N. Kudin, V. N. Staroverov, T. A. Keith, R. Kobayashi, J. Normand, K. Raghavachari, A. P. Rendell, J. C. Burant,

- S. S. Iyengar, J. Tomasi, M. Cossi, J. M. Millam, M. Klene, C. Adamo, R. Cammi, J. W. Ochterski, R. L. Martin, K. Morokuma, O. Farkas, J. B. Foresman, and D. J. Fox, Gaussian, Inc., Wallingford CT, **2016**
3. Becke, A. D. *Phys. Rev. A* **1988**, *38*, 3098.
 4. Lee, C.; Yang, W.; Parr, R. G. *Phys. Rev. B* **1988**, *37*, 785.
 5. Yanai, T.; Tew, D. P.; Handy, N. C. *Chem. Phys. Lett.* **2004**, *393*, 51.
 6. Dolg, M.; Wedig, U.; Stoll, H.; Preuss, H. *J. Chem. Phys.* **1987**, *86*, 866.
 7. Singhal, A.; Singh, S.; Chauhan, S. M. S. *Arkivoc* **2016**, *6*, 144.
 8. Tang, Y.; Zhou, L.; Li, J.; Luo, Q.; Huang, X.; Wu, P.; Wang, Y.; Xu, J.; Shen, J.; Liu, J. *Angew. Chem. Int. Ed.* **2010**, *49*, 3920.
 9. Song, X.; Li, N.; Wang, C.; Xiao, Y. *J. Mater. Chem. B* **2017**, *5*, 360.
 10. Yoshida, T.; Sakamaki, D.; Seki, S.; Shinokubo, H. *Chem. Commun.* **2017**, *53*, 1112.
 11. Brown, J. S. (2018). CATNIP (Version 1.9). [Software]. Available from https://github.com/JoshuaSBrown/QC_Tools.
 12. J. P. Perdew, in *Electronic Structure of Solids*, ed. P. Ziesche and H. Eschrig, Akademie Verlag, Berlin, **1991**, p. 11.
 13. J. Huang, M. Kertesz, *J. Chem. Phys.* **2005**, *122*, 234707.
 14. Nozawa, R.; Tanaka, H.; Cha, W.-Y.; Hong, Y.; Hisaki, I.; Shimizu, S.; Shin, J.-Y.; Kowalczyk, T.; Irle, S.; Kim, D.; Shinokubo, H. *Nat. Commun.* **2016**, *7*.
 15. Ogi, S.; Fukui, T.; Jue, M. L.; Takeuchi, M.; Sugiyasu, K. *Angew. Chem.* **2014**, *126*, 14591.
 16. Ren, L.; Hardy, C. G.; Tang, C. *J. Am. Chem. Soc.* **2010**, *132*, 8874.

List of Publications

1. “Synthesis and Electron-Transport Properties of a Stable Antiaromatic Ni(II) Norcorrole with the Smallest *meso*-Substituent”
Ukai, S.; Koo, Y. H.; Fukui, N.; Seki, S.; Shinokubo, H. *Dalton Trans.* **2020**, 49,14383.
2. “A Supramolecular Polymer Constituted of Antiaromatic Ni(II) Norcorroles”
Ukai, S.; Takamatsu, A.; Nobuoka, M.; Tsutsui, Y.; Fukui, N.; Ogi, S.; Seki, S.; Yamaguchi, S.; Shinokubo, H. *Angew. Chem. Int. Ed.* **2022**, in press (DOI: 10.1002/ange.202114230).
3. “Isolation and Structure Analysis of a Ni(II) Norcorrole Radical Anion”
Ukai, S.; Ikeue, T.; Fukui, N.; Shinokubo, H. *Chem. Lett.* **2022**, in press (DOI: 10.1246/cl.210715).

The following papers are not included in this doctoral thesis.

1. “Determinant Factors of Three-Dimensional Aromaticity in Antiaromatic Cyclophanes”
Kawashima, H.; Ukai, S.; Nozawa, R.; Fukui, N.; Fitzsimmons, G.; Kowalczyk, T.; Fliegl, H.; Shinokubo, H. *J. Am. Chem. Soc.* **2021**, 143, 10676.
2. “Dual-Ion NiNc Battery: A Sustainable Revolution for Sodium Organic Batteries”
Hwang, J.; Matsumoto, K.; Hagiwara, R.; Ukai, S.; Shinokubo, H.; Shin, J-Y. *Batter. Supercaps.* **2021**, 4, 1605.
3. “Trioxotriangulene with Carbazole: A Donor–Acceptor Molecule Showing Strong Near-Infrared Absorption Exceeding 1000 Nm”

Murata, T.; Kariyazono, K.; Ukai, S.; Ueda, A.; Kanzaki, Y.; Shiomi, D.; Sato, K.; Takui, T.; Morita, Y. *Org. Chem. Front.* **2019**, *6*, 3107.

4. “Intramolecular Magnetic Interaction of Spin-Delocalized Neutral Radicals through M-Phenylene Spacers”

Murata, T.; Asakura, N.; Ukai, S.; Ueda, A.; Kanzaki, Y.; Sato, K.; Takui, T.; Morita, Y. *ChemPlusChem* **2019**, *84*, 680.

5. “Colored Ionic Liquid Based on Stable Polycyclic Anion Salt Showing Halochromism with HCl Vapor”

Enozawa, H.; Ukai, S.; Ito, H.; Murata, T.; Morita, Y. *Org. Lett.* **2019**, *21*, 2161.

Acknowledgment

First of all, the author would like to express his deepest gratitude to Prof. Dr. Hiroshi Shinokubo at Graduate School of Engineering, Nagoya University, for his invaluable guidance and encouragement throughout this thesis. The author is deeply grateful to Dr. Norihito Fukui, Prof. Dr. Yoshihiro Miyake, and Prof. Dr. Ji-Young Shin for their kind and helpful discussions and suggestions for this study. The author was always inspired by the insightful advice from Prof. Shinokubo and the professors in the Shinokubo Group.

The author wishes to express deep appreciation to Prof. Dr. Makoto Yamashita at Graduate School of Engineering, Nagoya University, and Prof. Dr. Kentaro Tanaka at Graduate School of Science, Nagoya University. Their helpful suggestions and discussion were indispensable for the completion of his dissertation. It was a great honor that these leading researchers reviewed this thesis.

The author also owes a deep debt of gratitude to Prof. Dr. Shu Seki and Dr. Yusuke Tsutsui at Graduate School of Engineering, Kyoto University, for TRMC measurements of Ni(II) *meso*-dimethylnorcorrole, supramolecular polymers, and CT-complexes.

The author wishes to express deep appreciation to Prof. Dr. Shigehiro Yamaguchi and Prof. Dr. Soichiro Ogi at Graduate School of Science, Nagoya University, for their helpful suggestions and discussions on the supramolecular polymer research from the proposal and for providing various measurement instruments and the environment. The author feels very privileged to have an opportunity to collaborate with these leading researchers.

The author is obliged to Prof. Dr. Takahisa Ikeue at Graduate School of Natural Science and Technology, Shimane University, to help the ESR measurements of a Ni(II) norcorrole radical anion.

The author also gratefully acknowledges Prof. Dr. Yasushi Morita and Prof. Dr. Tsuyoshi Murata at the Department of Applied Chemistry, Faculty of Engineering, Aichi

Institute of Technology, for their invaluable guidance and encouragement when the author was in the Morita group from 2016 to 2019.

The author would like to acknowledge to following members of the Shinokubo Group for their friendly competition and consideration.

Dr. Ryo Nozawa	Mr. Hiroyasu Murase	Ms. Mai Odajima
Dr. Shuhei Akahori	Ms. Haruka Takekoshi	Mr. Yoshihiro Takeo
Dr. Takumi Nakazato	Ms. Nishijo Mayu	Mr. Shota Kino
Dr. Nishimura Tsubasa	Ms. Siham Asyiqin Shafie	Mr. Takumi Hayashi
Mr. Atsumi Yagi	Mr. Kazuya Miyagawa	Mr. Yuki Tanaka
Ms. Asahi Takiguchi	Mr. Hiroyuki Kawashima	Mr. Shigetatsu Tsugimoto
Ms. Siyu Liu	Ms. Shiho Mori	Ms. Kyoka Kusano
Mr. Takahiro Sakurai	Mr. Ryohei Noge	Mr. Yusei Takahashi
Mr. Keita Tajima	Mr. Masahiro Odawara	Mr. Ryoya Tomida
Mr. Tomoya Yokota	Mr. Kensuke Hanida	Mr. Ren Takayanagi
Mr. Yuki Tanaka	Mr. Masaki Kato	Ms. Ayako Kimata

The author is deeply grateful for financial supports from Japan Society for Promotion of Science (JSPS) and Graduate Program of Transformative Chem-Bio Research (GTR), which were indispensable to conduct this study.

Last but not least, the author desire to express deep gratitude beyond description to his father, Mr. Tatsuya Ukai, his mother, Ms. Eriko Ukai, his sister, Ms. Arina Ukai, his grandfather, Mr. Tokio Yamaguchi, his grandmother, Ms. Fumie Yamaguchi, his grandfather, Mr. Shigesaburo Ukai, and his grandmother, Ms. Yoko Ukai. This thesis would not have appeared in the present form without their hearty encouragement and devoted support.

Shusaku Ukai
鵜飼 修作
March 2022